UNIVERSITY OF CALIFORNIA,
IRVINE

Sweating the small stuff: simulating dwarf galaxies, ultra-faint dwarf galaxies, and their own tiny satellites

DISSERTATION

submitted in partial satisfaction of the requirements
for the degree of

DOCTOR OF PHILOSOPHY

in Physics

by

Coral Rose Wheeler

Dissertation Committee:
Professor James S. Bullock, Chair
Professor Michael C. Cooper
Professor Majoj Kaplinghat

2016

DEDICATION

To my father, Robert E. Wheeler (1948 - 2009), who won't get to see me complete my doctorate, but who loved astronomy and strongly encouraged me to return to graduate school just before he passed away. And to my dear friend Kit Reilly (1979-2003), a dreamer and an adventurer whose aspirations of becoming an astronomer were tragically cut short, but who was a huge inspiration to me to finish my degree.

TABLE OF CONTENTS

Page

LIST OF FIGURES **v**

LIST OF TABLES **ix**

ACKNOWLEDGMENTS **x**

CURRICULUM VITAE **xi**

ABSTRACT OF THE DISSERTATION **xiii**

1 Introduction **1**

2 The Surprising Inefficiency of Dwarf Satellite Quenching **4**
2.1 Introduction 4
2.2 Observations 5
2.3 Simulations 6
2.4 Results 8
2.4.1 Quenched Fraction vs. Subhalo Fraction 8
2.4.2 Testing Simple Models for Quenching 11
2.5 Summary 16
2.6 Discussion 17

3 The Existence and Star Formation Histories of Satellites of Dwarfs **23**
3.1 Introduction 23
3.2 Simulations 27
3.2.1 Sample Details 31
3.3 Results 33
3.3.1 Star Formation Histories 36
3.4 Detecting Satellites of Dwarfs 38
3.4.1 How Common are Satellites of Dwarfs? 38
3.4.2 Can they be detected? 42
3.5 Comparison to Previous work 44
3.6 Discussion and Conclusions 46

4 The No Spin Zone: Rotation vs Dispersion Support in Simulated and Observed Dwarf Galaxies **50**
4.1 Introduction . . . 50
4.2 Observations . . . 55
4.3 Simulations . . . 56
4.4 Measuring Rotation . . . 58
4.4.1 Bayesian Analysis . . . 58
4.4.2 Comments on Individual Galaxies . . . 62
4.4.3 Simulation analysis . . . 66
4.5 Results . . . 67
4.5.1 Inferring 3D Rotation . . . 70
4.6 Discussion . . . 71
4.7 Summary and Conclusion . . . 74

5 Conclusions **77**

Bibliography **79**

LIST OF FIGURES

Page

2.1 The fraction of quenched dwarf galaxies as a function of the projected distance from the nearest luminous neighbor (symbols, reproduced from G12). For comparison, the black band shows the fraction of those dwarf galaxies that are expected to reside within subhalos of a larger host, plotted as a function of the same separation measure, as determined by mock observations in the MS-II cosmological simulation. The thickness of this band corresponds to a range of $V_{\rm max}$ choices for identifying dwarf halos, as discussed in §3. The subhalo fraction is always well above the quenched fraction, meaning that it is impossible for all subhalos to be quenched; rather, satellite quenching at these mass scales must be fairly inefficient. 9

2.2 Range of virial masses (95%, light grey; 68%, dark grey) for the actual hosts of subhalos identified in Figure 1. Hosts of dwarfs found close to luminous neighbors have a range of viral masses spanning the group to cluster scale $\sim 10^{12.5-14}$ $M_\odot$, while hosts of dwarfs found far from large neighbors are concentrated around a much lower mass, $10^{11.5}$ $M_\odot$. The sharp decrease in the quenched fraction below $\sim 0.75 - 1$ Mpc seen in Figure 1 is likely associated with the virial radius scale of groups or small clusters. 9

2.3 The relationship between quenching and host halo mass. Colored bands show the predicted quenched fraction in a model where subhalos become quenched only when their host mass is above a given threshold: $V_{\rm max} > 150\,{\rm km\,s^{-1}}$ (cyan), $> 450\,{\rm km\,s^{-1}}$ (magenta), and $> 650\,{\rm km\,s^{-1}}$ (green). The symbols are the same data points shown in Figure 1. Reproducing the data requires a minimum host $V_{\rm max}$ of $650\,{\rm km\,s^{-1}}$, which is much too large given existing constraints on satellite quenching in lower mass hosts. The thickness of the bands illustrate how our results change as we vary the $V_{\rm infall}$ range used in identifying dwarf galaxy halos, as discussed in §3. 12

2.4 The relationship between quenching and infall time. Colored bands show the predicted quenched fraction in a model where subhalos become quenched only after a time $\tau_{\rm infall}$ of orbiting within a host: $\tau_{\rm infall} > 4$ Gyr (cyan), > 7 Gyr (magenta), and > 9.5 Gyr (green). This model works only with rather long quenching timescales, $\tau_{\rm infall} > 9.5$ Gyr. The thickness of the bands correspond to different ranges of $V_{\rm max}$ used to identify dwarf halos, as discussed in §3. 15

2.5 The relationship between quenching and mass loss. Colored bands show the predicted quenched fraction in a model where satellites become quenched when their subhalos have been stripped of mass beyond a certain level: $V_{\rm max}/V_{\rm infall} < 0.85$ (cyan), < 0.75 (magenta), and < 0.65 (green). The data are marginally well described by a quenching scenario with $V_{\rm max}/V_{\rm infall} = 0.65$ as the critical scale for star formation cessation. The thickness of the bands correspond to different ranges of $V_{\rm max}$ used to identify dwarf halos, as discussed in §3. 15

2.6 The environmentally quenched fraction – the fraction of satellites that are quenched in excess of that expected in the field, i.e. the fraction of satellites that are quenched because they are satellites. We see that while environmental quenching seems to have an approximately constant efficiency of $\sim$ 30% at stellar masses from 10^8 to 10^{11} $M_\odot$, there appears to be a dramatic upturn in quenching at lower stellar masses (if the Local Group is typical). 20

3.1 Projected ($x - y$ plane) visualizations for all of the runs presented in this work. From left to right, the top three panels visualize Dwarf 1, UFD 1 and UFD 2, while Dwarf $2_{\rm Early}$, Dwarf $2_{\rm Middle}$ and Dwarf $2_{\rm Late}$ are shown in the lower panels. The dark matter distribution is shown in greyscale, while the stellar density is pictured in color for all subhalos with $M_\star > 3 \times 10^3$ $M_\odot$ (in at least one run in the case of Dwarf 2; see text for details). $M_\star$ is calculated as the stellar mass within the inner 3 (1.5) kpc of the central (satellite) galaxy. The white line in the lower left of each panel represents 5 kpc. 28

3.2 Left: Subhalo mass function for all six runs. $M_{\rm halo}^{z=0}$ is the present day mass for all subhalos. For reference, $M_{\rm halo}^{z=0}$ is typically about a factor of 2 smaller than $M_{\rm peak}$. The left edge of the panel corresponds to $\sim$ 400 bound dark matter particles. Note: if these halos simply contained the universal fraction ($f_{\rm b} = 0.169$) of baryons, this would correspond to $\gtrsim$ 350 baryonic particles in these halos before they were forcefully removed by feedback. Middle: Stellar mass function for all satellites that form at least one star particle. The average mass of a single star particle is shown as a dark green band. Masses we regard as poorly-resolved ($M_\star < 3 \times 10^3$ $M_\odot$) are highlighted by the light green region. Right: $M_\star - M_{\rm halo}$ for all Centrals (filled circles), 1st and 2nd satellites (upward and downward triangles respectively). With surprisingly little scatter, our isolated dwarfs and their six well-resolved satellites (filled triangles) sit just offset from the extrapolated abundance matching relation from Garrison-Kimmel et al. [80] (solid black line). Both this and the abundance-matching relationship from Behroozi et al. [8] (dotted black line) are shown with 0.2 dex in scatter. Open symbols correspond to poorly resolved galaxies: $M_\star < 3 \times 10^3$ $M_\odot$ and/or $N_p^{\rm dm} < 2 \times 10^5$. 33

3.3 Cumulative fractional star formation histories (SFH) of the Centrals (solid) and well-resolved satellites (dashed / dotted) in the two isolated Dwarf simulations ($M_{\rm vir} \sim 10^{10}$ M$_\odot$). Short vertical lines along the top axes indicate infall times of the satellites. Top: Dwarf 1 Central (solid) along with its two satellites. The massive "dSph" satellite is shown by the dotted line and it displays a late-time burst in conjunction with its recent infall. The "ultra-faint" satellite (dashed) is quenched early, during reionization (shaded band), well before it is accreted. Bottom: Dwarf 2 centrals (solid) and the most massive satellites (dashed) in each run. All three "ultra-faint" satellites in the Dwarf 2 runs form all of their stars before $z = 2$. 39

3.4 Ancient "ultra-faints". Shown are the cumulative fractional star formation histories (SFH) for our isolated (solid) and resolved satellite (dashed) "ultra-faint" dwarfs ($M_\star^{z=0} = 3 - 30 \times 10^3$ M$_\odot$). The SFH of the unresolved outlier that passes the stellar mass cut (see Section 3.2.1 for details) is also shown (dotted line). All seven of these systems have ancient stellar populations, similar to those observed for the ultra-faint galaxies of the Milky Way. 40

3.5 From the dark-matter only ELVIS suite of Local Group simulations, the fraction of isolated dwarfs in the $V_{\rm max}$ range $35 - 45$ km s^{-1} with N or more subhalos with $M_{\rm peak} > 5 \times 10^8$ M$_\odot$ (thick line) and 4.5×10^9 M$_\odot$ (thin line) that are found within 50 kpc of their host galaxy. In all of our hydrodynamic runs, all subhalos with $M_{\rm peak} > 5 \times 10^8$ M$_\odot$ have formed a galaxy with $M_\star > 3 \times 10^3$ M$_\odot$, while the most massive satellite, "dSph", forms in a subhalo with $M_{\rm peak} \simeq 4.5 \times 10^9$ M$_\odot$. According to these dark-matter only simulations, $\sim 35\%$ of isolated dwarfs should have a "massive satellite" within their virial radii, but only $\leq 5\%$ should host a satellite as massive as "dSph". 41

3.6 2D half-stellar-mass radii, $R_{1/2}$, vs $M_\star$ for all resolved galaxies in our simulations (filled circles and triangles; colors are the same as in Figure 3.2), the one unresolved satellite with $M_\star > 3000$ M$_\odot$ (open triangle), as well as for observed Milky Way dwarfs [173, open circles], the newly discovered DES ultra-faint dwarf candidates [241, black points with error-bars], [63, red points with error-bars], and Hydra II [162, blue square]. The solid line represents a surface brightness limit of 30 mag arcsec^{-2} while the dashed line shows 32.5 mag arcsec^{-2}. Both lines and the Hydra II data point assume a stellar mass-to-light ratio of 1. Satellites as massive as "dSph", which occur around $\sim 5\%$ of isolated dwarfs (see Figure 3.5), should be currently visible, but most of the satellites lie just out of reach, and will visible only with future surveys such as LSST or potentially even DES. 43

4.1 Stellar rotation support $v_{\rm rot}/\sigma$ vs. e (ellipticity) for observed satellites of the Milky Way and M31 (open gray triangles), isolated Local Group Dwarfs (cyan stars), and simulated isolated (dIrr) galaxies (gray squares). Open stars show the two galaxies for which a flat rotation model is preferred. The solid line shows the approximate value of $v_{\rm rot}/\sigma$ for self-gravitating objects that are flattened by rotation [24]. The (5/30) observed satellite galaxies (open triangles) that lie above the curve are Andromeda VII, Andromeda II, Coma Berenecis NGC 147, and Canis Venatici II. Only three isolated observed galaxies lie above the curve. Those are Leo A, Pegasus, and Aquarius. 65
4.2 Stellar rotation support ($v_{\rm rot}/\sigma$) vs. stellar mass for observed satellites of the Milky Way and M31 (open gray triangles), isolated Local Group Dwarfs (cyan stars), and our simulations (gray squares). No clear trend with stellar mass is seen in the data, although there could be a slight upward turn at the highest masses observed. 65
4.3 Rotation support $v_{\rm rot}/\sigma$ vs $\rm d_{L_\star}$, distance from the dwarf to the closest $L_\star$ galaxy (either the Milky Way or M31), for observed classical Milky Way dSphs (up-facing dark magenta triangles), ultra-faint dSphs (down-facing light magenta triangles), M31 dSphs (gold circles), isolated Local Group Dwarfs (cyan stars) and dEs (brown pentagons). There is no clear trend between $v_{\rm rot}/\sigma$ and $\rm d_{L_\star}$, as predicted by tidal stirring models. 68
4.4 Distribution of measured $v_{\rm rot}/\sigma$ on the sky if all galaxies are assumed to have an intrinsic $v_{\rm rot}/\sigma$ value of 0.7 (dash-dotted line), 2.0 (dashed line) or 3.0 (dotted line), but are viewed with a random inclination. The thick solid black (thin solid cyan) line shows the distribution of estimated median $v_{\rm rot}/\sigma$ values for the satellites (isolated dwarfs) in our sample. The error in the satellite distribution is illustrated with 1000 thin gray lines, each consisting of points drawn randomly from Gaussian distributions with parameters taken from the estimated values for each of the 29 dSphs in our sample. For clarity, the error is not shown for the distribution of isolated galaxies, but has a wider spread than the lines for the satellite population. The isolated distribution is distinct from the satellite distribution, and more closely tracks $v_{\rm rot}^{\rm intrinsic}/\sigma \sim 1-2$. However, it is clear that the $v_{\rm rot}^{\rm intrinsic}/\sigma$ values for the isolated galaxies are much less than 3, the commonly used value in tidal stirring simulations. 72

LIST OF TABLES

Page

3.1 Halo and stellar masses of all central galaxies and their 1st and 2nd satellites from all six simulations. For all simulations except Dwarf $2_{\rm Early}$ and Dwarf $2_{\rm Late}$, the 1st and 2nd satellites refer to the first and second most massive satellites in stellar mass. The 2nd Satellites for Dwarf $2_{\rm Early}$ and Dwarf $2_{\rm Late}$ are selected because their counterpart within Dwarf $2_{\rm Middle}$ has $M_\star > 3 \times 10^3$ $M_\odot$. Both satellites in Dwarf 1 and the 1st satellites in all Dwarf 2 runs are "massive satellites" (see text). The stellar masses of all other satellites are shown in parentheses. 31

4.1 Properties and estimated parameters of all galaxies in the observed sample. (1) Name of galaxy. (2) Galaxy type. (3) Galaxy stellar mass from literature. (4) Distance from galaxy to its nearest massive neighbor from literature – either the Milky Way or M31. (5) Ellipticity of galaxy obtained from literature, with error. (6) Median of parameter $v_{\rm rot}/\sigma$ from Bayesian analysis, with ± 1 σ error. (7) Median rotational velocity from Bayesian analysis, with ± 1 σ error. (8) Median velocity dispersion from Bayesian analysis, with ± 1 σ error. (9) Number of stars used in analysis. (10) $\ln B_{\rm rad}$, where B is the Bayes factor for the rotation model. Values less than 3 imply weak/inconclusive evidence for the radially varying model and negative values favor the flat rotation model, see Section 4.4.1 for details). (11) $\ln B_{\rm rot}$, where B is the Bayes factor for rotation vs non-rotation. Values less than 3 imply weak/inconclusive evidence for rotation and negative values favor non-rotation to varying degrees, see Section 4.4.1 for details). (12) Citations: a) McConnachie 174, b) Simon & Geha 225 c) Koposov et al. 142, d) Walker, Olszewski & Mateo 264, e) Pace 193, f) Walker et al. 259, g) Koch et al. 135, h) Frinchaboy et al. 78, i) Mateo 167, j) Salomon et al. 216, k) Tollerud et al. 243, l) Collins et al. 47, m) Martin et al. 163, n) Martin et al. 159, o) Ho et al. 94, p) Geha et al. 83, q) Fraternali et al. 77, r) Kirby et al. 127, s) Leaman et al. 149, t) Leaman et al. 150. *We exclude Sagittarius from all figures. See Section 4.4.2 for details. † There are only two galaxies for which a flat rotation model is preferred (Aquarius and NGC 6822). For these two galaxies, columns 6,7,8 and 11 are all calculated assuming a flat rotation model. 57

ACKNOWLEDGMENTS

I would like to thank my thesis advisor, James Bullock, for being incredibly supportive every single step of the way throughout my unusual career path. I could never possibly recount every example of support that James provided during difficult times in research, dealing with bureaucracy at UCI, and in my personal life when appropriate, but each and every time was instrumental in completing my graduate career.

I would like to further thank my committee members, Michael Cooper and Manoj Kaplinghat, as well as all of the professors in the department, who not only taught me astronomy and astrophysics, but who made the department a welcoming environment during my time here.

There were a few individuals who went above and beyond to help me acquire the technical skill necessary to run and analyze simulations. I am indebted to Erik Tollerud, Mike Boylan-Kolchin, Jose Oñorbe, and Shea Garrison-Kimmel.

I would also like to thank my many co-authors (not mentioned above), Andrew Pace, Alex Fitts, Phil Hopkins, Dusan Kereš, Oliver Elbert, Sean Fillingham, John Phillips, and Tobias Kaufmann, who made the research presented here possible. I would also like to thank every graduate student who passed through my research group, and everyone that participated in department activities. All of the technical and scientific discussions I had with all of you helped shape me into the scientist I am today.

Finally, I want to thank my friends and family. You helped me become the person I am now, and I could not have completed my Ph.D. without your love and encouragement. In particular, I want to thank my sisters, Ivy and Kalen Wheeler, for being the best emotional support system that I could have ever wanted, and my dear friends Sarah and Yossi Arditi, for getting me through the last few months. I would not have even gone into science if not for the tremendous support of my parents, Dan Wasdahl and Colette Rice, and I have been inspired to continue to succeed by the achievements of my cousin John Rice and my brother, Alex Wasdahl.

This work could not have been completed without funding from NSF grants AST-1009973, AST-1009999, *Hubble Space Telescope* grants HST-AR-13921.002-A and HST-AR-13888.003-A, and the Josephine de Karman Trust. I would like to further acknowledge computational resources granted by NASA Advanced Supercomputing (NAS) Division, NASA Center for Climate Simulation, Teragrid and by the Extreme Science and Engineering Discovery Environment (XSEDE), supported by National Science Foundation grant number OCI-1053575 and ACI-1053575, the latter through allocation AST140080 (PI: Boylan-Kolchin), as well as the Caltech compute cluster "Zwicky" (NSF MRI award #PHY-0960291) and allocation TG-AST130039 granted by the Extreme Science and Engineering Discovery Environment (XSEDE) supported by the NSF.

CURRICULUM VITAE

Coral Rose Wheeler

EDUCATION

Doctor of Philosophy in Physics **2016**
University of California, Irvine *Irvine, CA*

Completed requirements for Master of Science in Physics **2008**
University of California, Irvine *Irvine, CA*

Bachelor of Science in Mathematics **2003**
The University of Akron *Akron, OH*

RESEARCH EXPERIENCE

Josephine de Karman Dissertation Year Fellow **2015–2016**
University of California, Irvine *Irvine, California*

Graduate Research Assistant **2012–2015**
University of California, Irvine *Irvine, California*

Graduate Student Research Assistant and GAANN Fellow **2005–2008**
University of California, Irvine *Irvine, California*

FIRST AUTHOR PUBLICATIONS

The no-spin zone: rotation vs dispersion support in observed and simulated dwarf galaxies **2016**
submitted to MNRAS

Sweating the small stuff: simulating dwarf galaxies, ultra-faint dwarf galaxies, and their own tiny satellites **2015**
MNRAS

The surprising inefficiency of dwarf satellite quenching **2014**
MNRAS

CONTRIBUTED PUBLICATIONS

Under Pressure: Quenching Star Formation in Low-Mass Satellite Galaxies via Stripping **2016**
Submitted to MNRAS

Taking care of business in a flash: Constraining the timescale for low-mass satellite quenching with ELVIS **2015**
MNRAS

The mass dependence of satellite quenching in Milky Way-like halos **2015**
MNRAS

A dichotomy in satellite quenching around L* galaxies **2014**
MNRAS

On the morphologies, gas fractions, and star formation rates of small galaxies **2007**
MNRAS

ABSTRACT OF THE DISSERTATION

Sweating the small stuff: simulating dwarf galaxies, ultra-faint dwarf galaxies, and their own tiny satellites

By

Coral Rose Wheeler

Doctor of Philosophy in Physics

University of California, Irvine, 2016

Professor James S. Bullock, Chair

We study dwarf satellite galaxy quenching using observations from the Geha et al. (2012) NSA/SDSS catalog together with ΛCDM cosmological simulations to facilitate selection and interpretation. We show that fewer than 30% of dwarfs ($M_\star \simeq 10^{8.5-9.5}\,\mathrm{M}_\odot$) identified as satellites within massive host halos ($M_{\rm host} \simeq 10^{12.5-14}\,\mathrm{M}_\odot$) are quenched. We conclude that whatever the action triggering environmental quenching of dwarf satellites, the process must be highly inefficient. We investigate a series of simple, one-parameter quenching models in order to understand what is required to explain the low quenched fraction and conclude that either the quenching timescale is very long ($> 9.5\,$Gyr, a "slow starvation" scenario) or that the environmental trigger is not well matched to accretion within the virial volume.

We further present FIRE/`Gizmo` hydrodynamic zoom-in simulations of isolated dark matter halos, two each at the mass of classical dwarf galaxies ($M_{\rm vir} \simeq 10^{10}\,\mathrm{M}_\odot$) and ultra-faint galaxies ($M_{\rm vir} \simeq 10^{9}\,\mathrm{M}_\odot$). The resulting central galaxies lie on an extrapolated abundance matching relation from $M_\star \simeq 10^6$ to $10^4\,\mathrm{M}_\odot$ without a break. Our dwarfs with $M_\star \simeq 10^6\ \mathrm{M}_\odot$ each have $1-2$ well-resolved satellites with $M_\star = 3 - 200 \times 10^3\,\mathrm{M}_\odot$. Even our isolated ultra-faint galaxies have star-forming subhalos. We combine our results with the ELVIS simulations to show that targeting $\sim$ 50 kpc regions around nearby isolated dwarfs could increase the chances of discovering ultra-faint galaxies

by $\sim 35\%$ compared to random pointings.

The well-resolved ultra-faint galaxies in our simulations ($M_\star \simeq 3 - 30 \times 10^3$ $M_\odot$) form within $M_{\rm peak} \simeq 0.5 - 3 \times 10^9\,M_\odot$ halos. Each has a uniformly ancient stellar population (> 10 Gyr) owing to reionization-related quenching. More massive systems, in contrast, all have late-time star formation. Our results suggest that $M_{\rm halo} \simeq 5 \times 10^9\,M_\odot$ is a probable dividing line between halos hosting reionization "fossils" and those hosting dwarfs that can continue to form stars in isolation after reionization.

Finally, we perform a systematic Bayesian analysis of rotation vs. dispersion support ($v_{\rm rot}/\sigma$) in 40 dwarf galaxies throughout the Local Volume (LV) over a stellar mass range $10^{3.5}\,M_\odot < M_\star < 10^8\,M_\odot$. We find that the stars in $\sim 80\%$ of the LV dwarf galaxies studied – both satellites and isolated systems – are dispersion-supported. These results challenge the traditional view that the stars in gas-rich dwarf irregulars (dIrrs) are distributed in cold, rotationally-supported stellar disks, while gas-poor dwarf spheroidals (dSphs) are kinematically distinct in having dispersion-supported stars. We apply the same Bayesian analysis to four of the FIRE/`Gizmo` hydrodynamic zoom-in simulations of isolated dwarf galaxies ($10^9\,M_\odot < M_{\rm vir} < 10^{10}\,M_\odot$) and show that the simulated *isolated* dIrr galaxies have stellar ellipticities and stellar $v_{\rm rot}/\sigma$ ratios that are consistent with the observed population of dIrrs *and* dSphs without the need to subject these dwarfs to any external perturbations or tidal forces. We posit that most dwarf galaxies form as puffy, dispersion-dominated systems, rather than cold, angular momentum-supported disks. If this is the case, then transforming a dIrr into a dSph may require little more than removing its gas.

Chapter 1

Introduction

The high dark matter content and the shallow potential wells of low mass, or "dwarf", galaxies (10^3 $M_\odot < M_\star < 10^{9.5}$ $M_\odot$) make them excellent testbeds for differing theories of galaxy formation, including how star formation and stellar feedback affect their stellar mass, morphology and satellite population and how their star formation is eventually "quenched", or shut down. Dwarf galaxies towards the upper end of this stellar mass range (10^7 $M_\odot < M_\star < 10^9$ $M_\odot$) appear to only be quenched in the presence of a massive neighbor ($M_\star \sim 10^{10.5}$ $M_\odot$), suggesting that all dwarfs in the field (i.e. far from a massive neighbor) in this mass range are star-forming Geha et al. [82, hereafter G12]. Even within 250 kpc (projected on the sky) of a massive neighbor, only about 35% of dwarfs are non-star-forming, which implies that, whatever the quenching mechanism, it is extremely inefficient for galaxies in this mass range. The picture becomes even less clear at the lower end of the dwarf mass range (10^3 $M_\odot < M_\star < 10^8$ $M_\odot$). Due to the low luminosities of the tiniest observed dwarfs, observations are largely limited to the Local Volume, or even to the Milky Way's virial radius at the lowest masses observed ($M_\star \sim 10^3$ $M_\odot$). Because nearly all ($\gtrsim 80\%$) of the satellites of the Milky Way and M31 with $M_\star < 10^8$ $M_\odot$ are quenched [167, 174], the recent infall times suggested by cosmological simulations require a faster-acting quenching mechanism [75].

Additional complications arise due to the number of dark matter halos expected to not have formed any galaxies at all. Although cosmological dark matter-only simulations predict the existence of 100s - 1000s of subhalos within the virial radius of the Milky Way's dark matter halo, there are only ~ 30 observed satellites orbiting our Galaxy. As first suggested by Bullock, Kravtsov & Weinberg [39], most extremely low mass dark matter halos were likely prevented from forming any stars due to the onset of the cosmic ionizing radiation, and its heating of the intergalactic medium to temperatures above the virial temperature of these low mass subhalos. However, the specific mass range at which this cut-off may occur is still largely unknown. If some of these galaxies were able to accrete gas and form some stars before having their star formation quenched by this radiation, they would exhibit uniformly ancient stellar populations or possibly even bimodal star formation histories [209]. If such "fossils" of reionization do exist, they may inhabit lower mass dark matter halos than all currently observed dwarfs, and have low surface brightnesses that place them just outside the detection limits of current galaxy surveys [40].

Complicating the determination of external quenching mechanisms is the presence of internal "feedback" – energy, mass and momentum imparted to the galactic gas from the stars in each galaxy [97]. It is possible that some or even all external quenching mechanisms are aided by the gas blow-out associated with feedback in dwarf galaxies. For those quenching mechanisms, such as ram-pressure stripping (the violent removal of cold gas from a galaxy due to the pressure force exerted on it by a hotter gaseous medium [90]), the feedback itself may itself be increased due to gas compression-induced star formation upon infall onto the host galaxy [74].

Gas blow-out and ram-pressure stripping were also initially thought to be responsible for the two seemingly distinct populations of galaxies found in the Local Volume [65, 55]. Dwarf Irregular galaxies (dIrrs) have (rotating) gas, ongoing star formation, and some exhibit disk-like features [167, 174]. Dwarf spheroidal galaxies (dSphs), believed to be descended from dIrrs, have spheroidal shapes, no gas, and no ongoing star formation [87, 174]. However, a feedback-induced blow-out transformation mechanism fails to account for the fact that dSphs and dIrrs are found near

and far, respectively, from massive hosts, and ram-pressure stripping cannot account for what was initially thought to be a significant amount of kinematic difference between the stellar populations in each type of galaxy [87]. To solve these problems, later studies suggested a process – known as tidal stirring – by which a galaxy's stellar component is randomized by the tidal forces associated with repeated pericentric passages near a massive host [171]. However, recent cosmological simulations suggest that the Milky Way dwarfs likely fell in much too recently to have undergone the required number of passages [210, 80].

These questions – what shuts down star formation in dwarfs? What is the lowest dark matter halo to host a galaxy? What is required to transform a dwarf spheroidal into a dwarf irregular? – can be informed by a combination of observations, dark-mater only simulations, and fully hydrodynamic zoom-in simulations. This paper, which sets out to do so, is organized as follows. Chapter 2 tests several simple quenching mechanisms for higher mass dwarfs by comparing dark matter-only simulations to a large observational sample taken from the Sloan Digital Sky Survey. Chapter 3 investigates the extremely low-mass end of the galaxy luminosity function and reionization-related quenching in ultra-faint dwarf galaxies. Chapter 4 explores the effect of feedback on the stellar populations of dwarfs, and compares the kinematics of the stellar populations in observed Local Volume dIrrs and dSphs. We conclude in Chapter 5.

Chapter 2

The Surprising Inefficiency of Dwarf Satellite Quenching

2.1 Introduction

In addition to isolating the impact of environment on low-mass galaxies, the analysis by G12 provides well-defined, quantitative observational constraints on potential quenching mechanisms. For example, G12 probe the physical extent of environmental quenching, finding that dwarf galaxies are only quenched within a projected distance of $\sim$ 1–1.5 Mpc of a luminous galaxy. They interpret this result by suggesting that dwarfs are being quenched at 2–4 virial radii of Milky Way size hosts. Below, we use cosmological simulations to suggest an alternative scenario in which the $\sim$ 1 – 1.5 Mpc scale more likely corresponds to the virial radius of galaxy groups or small clusters. Moreover, G12 also find that even within 250 kpc of a luminous neighbor, the fraction of quenched systems peaks at $\sim$ 25–30%. The implication of these findings is that satellite quenching is remarkably inefficient at low stellar masses, and we can constrain quenching models through the requirement that they match this low efficiency.

In what follows we compare mock observations of a large N-body simulation to the observed quenched fractions vs. projected distance to a luminous neighbor from G12. We consider several one-parameter models for quenching, including a simple quenched-at-infall scenario as well as models where quenching depends on the host $V_{\rm max}$, satellite infall time, or the ratio of the satellite's current $V_{\rm max}$ to the $V_{\rm max}$ it had at infall. In Sections 2.2 and 2.3 we describe the G12 observational sample and our simulations, respectively. Section 2.4 presents our principal results. Finally, we summarize our findings in Section 2.5 and discuss them in light of past work in Section 2.6.

2.2 Observations

Our observational comparisons rely on the work of G12, who construct a dwarf galaxy sample selected from the NASA-Sloan Atlas (NSA) of the SDSS Data Release 8 spectroscopic catalog with an improved background subtraction technique [26, 3]. G12 investigate the fraction of quenched dwarf galaxies as a function of projected distance to a more luminous neighboring galaxy with a velocity offset of $1000\,{\rm km\,s^{-1}}$ or less. The dwarfs in this sample have stellar masses that range from $7.5 < \log(M_\star/\,{\rm M}_\odot) < 10$. The luminous neighboring galaxies are selected from the 2MASS Extended Source Catalog [229] and have stellar masses of $M_\star > 2.5 \times 10^{10}\,{\rm M}_\odot$. We investigate a subset of this sample for simplicity, focusing on the stellar mass bins $8.25 \leq \log(M_\star/\,{\rm M}_\odot) < 8.75$ and $9.25 \leq \log(M_\star/\,{\rm M}_\odot) < 9.625$.

G12 define quenched galaxies as having both no Hα emission and $\rm D_n4000 > 0.6{+}0.1\,log_{10}(M_\star/\,M_\odot)$, a criteria based on the light-weighted age of the stellar population. We adopt the same definition of quenched for the observations in this work. See G12 for more details on the observational sample.

2.3 Simulations

We use the Millennium II Simulation [MS-II, 35] to construct a mock galaxy catalogue with the goal of mimicking, via abundance matching, the sample used in G12. MS-II is a dark-matter-only simulation of $2160^3 \approx 10$ billion particles in a box of size $L_{\rm box} = 100\ h^{-1}\,{\rm Mpc}$, with a particle mass of $m_{\rm p} = 6.885 \times 10^6 h^{-1}\,{\rm Mpc}$ and a Plummer-equivalent force softening of $\epsilon = 1\ h^{-1}\,{\rm kpc}$ in comoving units. The cosmological parameters are $\Omega_{\rm tot} = 1.0$, $\Omega_{\rm m} = 0.25$, $\Omega_{\rm b} = 0.045$, $\Omega_\Lambda = 0.75$, $h = 0.73$, $\sigma_8 = 0.9$, and $n_{\rm s} = 1$, where σ_8 is the rms amplitude of linear mass fluctuations in $8\ h^{-1}\,{\rm Mpc}$ spheres at $z = 0$ and $n_{\rm s}$ is the spectral index of the primordial power spectrum. The simulation stores all gravitationally self-bound dark matter subhalos down to 20 particles, which corresponds to a resolved mass of $1.38 \times 10^8\ {\rm M}_\odot$. Thus, MS-II is more than adequate to make realistic comparisons to our data, as it has the resolution required to resolve the subhalos that would likely host the galaxies in the G12 sample.

In the figures that follow, the simulation data is made by selecting halos that lie in two distinct $V_{\rm max}$ (taken at infall for subhalos) bins. The lower (upper) $V_{\rm max}$ bin contains halos with $80\ {\rm km\,s^{-1}} < V_{\rm max} < 90\ {\rm km\,s^{-1}}$ ($100\ {\rm km\,s^{-1}} < V_{\rm max} < 110\ {\rm km\,s^{-1}}$) and roughly corresponds, via abundance matching [33], to the G12 stellar mass bin centered at $M_\star = 10^{8.5}\ {\rm M}_\odot$ ($M_\star = 10^{9.5}\ {\rm M}_\odot$). Rather than make an explicit comparison between a single $V_{\rm max}$ bin and a single bin in stellar mass in the plots, we attempt to encompass the uncertainty of abundance matching at low $V_{\rm max}$ by comparing points from the G12 data to shaded bands that show results as we vary $V_{\rm max}$ between these two selection bins. In practice, our results are not strongly sensitive to the precise range of $V_{\rm max}$ corresponding to the satellite stellar masses from the NSA. This is evidenced by the fact that these bands are relatively thin in the following figures.

In selecting subhalos, we use the $V_{\rm max}$ at infall, hereafter $V_{\rm infall}$, where infall is defined in MS-II as the time at which a halo most recently became a subhalo (see Section 2.4.2). This ensures that any tidal stripping that a subhalo has experienced will not introduce biases in the abundance matching

for that halo. Behroozi et al. [9] have recently shown that $V_{\rm infall}$ is distinct from $\rm V_{peak}$ (the largest value of $V_{\rm max}$ in the subhalo's history), that $\rm V_{peak}$ is typically set by a 1:5 merger, and that the time at which it occurs does not correspond to the time at which the halo mass peaks. However, $V_{\rm infall}$ does correspond to the peak halo mass. Thus, we consider the $V_{\rm max}/V_{\rm infall}$ ratio to be a better proxy for mass loss of a subhalo than would be $V_{\rm max}/\rm V_{peak}$. We select only those halos that have a $V_{\rm max}/V_{\rm infall} > 3/8$, ensuring that our sample is complete down to our lower $V_{\rm infall}$ limit of $80\,\rm km\,s^{-1}$, as MS-II is complete down to a current $V_{\rm max}$ of $40\,\rm km\,s^{-1}$.

For simplicity and without loss of generality, we mock observe the simulation by placing the "observer" at the origin. Then, following G12, we determine the projected distance, $\rm d_{Neighbor}$, from each halo in our dwarf mass range to the closest (in projected distance) halo that would be likely to host a more luminous galaxy. We use the term "luminous neighbor", once again following G12, but will use quotation marks when we are actually referring to the dark matter halo of the luminous neighbor. We choose a minimum $V_{\rm infall}$ of $150\,\rm km\,s^{-1}$ for the population of "luminous neighbors" which corresponds – according to the abundance matching relation of Boylan-Kolchin, Bullock & Kaplinghat [33] – to the stellar mass limit ($> 10^{10.4}\,\rm M_\odot$) used to select luminous neighbors in G12. In our mock observations, there are instances where the "luminous neighbor" of the dwarf is not the dwarf's actual host, but a subhalo of larger halo. Therefore, we use the $V_{\rm infall}$ of the "luminous neighbors" instead of their $V_{\rm max}$ unless we are referring to a subsample of the "luminous neighbors" for which all of the objects are actual host halos in the simulation.

In order to match the observations of G12 so that we can make appropriate comparisons, we follow exactly their method of removing contaminants in the sample. We remove halos that are close in projection but distant in velocity space by making sure that the velocity offset between the dwarf and the "luminous neighbor" is less than $1000\,\rm km\,s^{-1}$. This cutoff will indeed remove some interlopers, but as Phillips et al. [198] show, even with a more restrictive velocity offset maximum of $500\,\rm km\,s^{-1}$ and the imposition of a set of isolation criteria designed to remove groups and cluster halos, false pairs are still quite common. For LMC size satellites within 350 kpc of isolated Milky

Way analogs, Phillips et al. [198]show that the "host-satellite" pairs are still false pairs 25% of the time. This suggests that with our $1000\,\mathrm{km\,s^{-1}}$ cutoff and no isolation criteria, we will quite often identify a "luminous neighbor" that is not the actual host of the dwarf, even when the pairs are close in projection. Nonetheless, we use the $1000\,\mathrm{km\,s^{-1}}$ velocity offset in order to exactly match what was done for the observations from G12 so that our comparisons to their data are meaningful.

Although Guo et al. [91] and Moster, Naab & White [181] have constructed mock catalogues of galaxies with star formation rates and colors derived from semi-analytic models applied to MS-II, we have independently confirmed results [268, 125, 267, 266] showing that the semi-analytic models over-predict the red fraction of satellites significantly. By relying instead on our simple models applied to subhalos, we aim to gain insight into the basic prescriptions that will be required to match the data more effectively in the future.

2.4 Results

2.4.1 Quenched Fraction vs. Subhalo Fraction

The symbols (circles and triangles) in Figure 2.1 reproduce results from G12: the fraction of dwarfs that are quenched is plotted as a function of projected distance from their nearest luminous ($M_\star > 2.5 \times 10^{10}\,\mathrm{M_\odot}$) neighbor. As emphasized in G12, the quenched fraction is effectively zero at large $\mathrm{d_{Neighbor}}$ separation, rising to $\sim$ 25–30% at the smallest separations. For comparison, the black band shows the fraction of dwarf halos in the simulation – identified by mock observations that mirror exactly those used by G12 to produce the data points (see Section 2.3) – that are known subhalos (i.e. that are subhalos within a larger FOF group).

Figure 2.1 reveals at least two interesting points for elaboration. First, the subhalo fraction remains nonzero even at very large $\mathrm{d_{Neighbor}}$ separation, hovering just under 10% in a region of the figure that

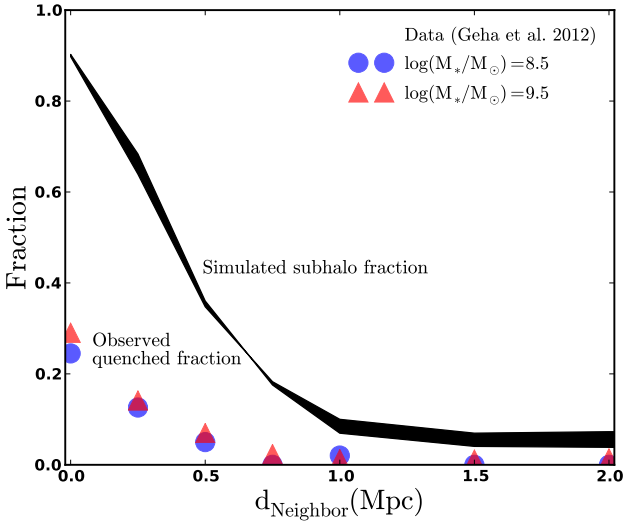

Figure 2.1: The fraction of quenched dwarf galaxies as a function of the projected distance from the nearest luminous neighbor (symbols, reproduced from G12). For comparison, the black band shows the fraction of those dwarf galaxies that are expected to reside within subhalos of a larger host, plotted as a function of the same separation measure, as determined by mock observations in the MS-II cosmological simulation. The thickness of this band corresponds to a range of $V_{\rm max}$ choices for identifying dwarf halos, as discussed in §3. The subhalo fraction is always well above the quenched fraction, meaning that it is impossible for all subhalos to be quenched; rather, satellite quenching at these mass scales must be fairly inefficient.

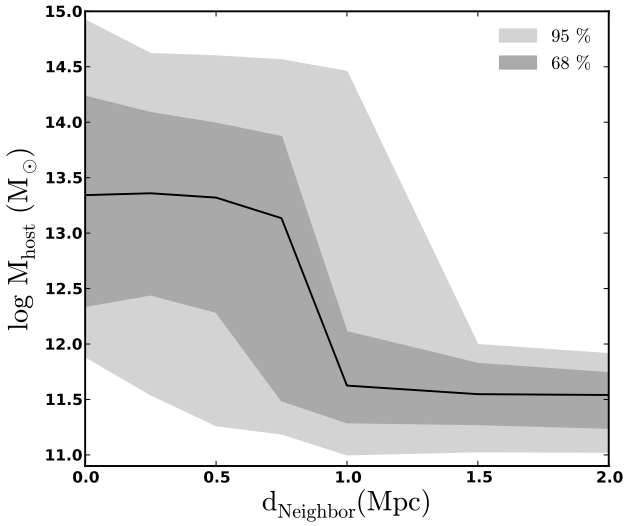

Figure 2.2: Range of virial masses (95%, light grey; 68%, dark grey) for the actual hosts of subhalos identified in Figure 1. Hosts of dwarfs found close to luminous neighbors have a range of viral masses spanning the group to cluster scale $\sim 10^{12.5-14}$ $M_\odot$, while hosts of dwarfs found far from large neighbors are concentrated around a much lower mass, $10^{11.5}$ $M_\odot$. The sharp decrease in the quenched fraction below $\sim 0.75 - 1$ Mpc seen in Figure 1 is likely associated with the virial radius scale of groups or small clusters.

is designed to target isolated galaxies. The reason for this is that galaxies at large separation from *luminous* hosts can nevertheless be subhalos of dimmer hosts that fall below the luminosity cut (for our purposes, halos with $V_{\rm max} < 150\,{\rm km\,s^{-1}}$; as demonstrated explicitly in Figure 2 and discussed below). The fact that observed dwarfs at these large $d_{\rm Neighbor}$ separations are *all* star-forming, even though $\sim 10\%$ of them are identified as subhalos of *something*, immediately demands that not all subhalos are quenched. A second point of note in Figure 1 is that the subhalo fraction rises to $\sim 90\%$ at small $d_{\rm Neighbor}$, while the quenched fraction remains relatively low by comparison (~ 25–30%). We see again that the mere act of being a subhalo cannot result in immediate quenching.

Figure 2.2 provides a more detailed examination of the mock observations used in Figure 2.1, concentrating on the subset of halos in each $d_{\rm Neighbor}$ bin that are identified as subhalos. The shaded bands show the range of host virial masses inhabited by subhalos for a given $d_{\rm Neighbor}$ separation.[1] The median halo mass is plotted as a solid black line, while the 68% and 95% regions are shown in dark and light grey, respectively. As expected, dwarf halos that are identified as subhalos with $d_{\rm Neighbor} \gtrsim 1$ Mpc have much smaller host masses than the dwarfs with $d_{\rm Neighbor} < 0.5$ Mpc. Dwarfs within ~ 0.5 Mpc are found preferentially in cluster size host halos. Although we cannot rule out the hypothesis of G12 that the drop-off seen at ~ 1 Mpc corresponds to 2–4 times the virial radius of a typical $M_\star \sim 3 \times 10^{10}\,{\rm M}_\odot$ galaxy, we find this scenario unlikely as it would imply that satellites are being quenched at equal or greater efficiency where the ambient gas density is very low relative to satellites within the virial radius of clusters or large groups. Thus, we find that a natural alternative explanation for the quenched fraction drop-off at ~ 1 Mpc is that it is set by the typical virial radius of a large group or a small cluster.

The preceding discussion has shown that satellite quenching is far too inefficient to be caused simply by a galaxy becoming a satellite (i.e. falling into another dark matter halo). The fraction of observed quenched dwarfs in the inner bin of Figure 2.1 (within 250 kpc of a more luminous neighbor) is just over 25%, while over 90% of simulated dwarfs selected in the same manner and

[1] We emphasize that the halo mass shown is that of the true host halo identified in the simulations, which is not necessarily that associated with the "luminous neighbor" identified in the mock G12 observations.

at the same projected distance are subhalos (typically, of $\sim 10^{13.5}\,M_\odot$ hosts). This implies that at most $\sim 30\%$ of subhalos are quenched. This disparity between subhalo fraction and observed quenched fraction is consistent with known problems faced by many models of galaxy formation in explaining observed satellite red fractions. In particular, models in which gas is instantaneously stripped from an infalling satellite upon entering into the host's virial radius over-predict satellite red fractions [e.g. 125]. In the next section, we explore a few simple models in order to understand what is required to explain the relatively low fraction of quenched dwarf satellites seen in the G12 data.

2.4.2 Testing Simple Models for Quenching

Figure 2.2 shows that the host halos of the star-forming dwarfs at large $d_{\rm Neighbor}$ are systematically less massive than those of the dwarfs found within 1 Mpc of a luminous neighbor. Since dwarfs at these large distances are uniformly star-forming, this suggests a simple model that limits quenching to hosts above a minimum halo mass. A model of this kind might be motivated by the transition mass at which a quasi-static gaseous corona forms [122, 25, 180]. However, several authors have argued that trends between the quenched fraction and host mass could be strongly affected by "pre-processing", whereby the satellites falling into massive hosts have previously fallen into less massive host halos that are then accreted onto the more massive systems, and thus have been preferentially quenched by the first host that they fell into [255, 52, 273].

To investigate the possibility that satellites are only quenched when falling into a host above a certain halo mass, we develop a "minimum mass" quenching model for which the resulting dependence of quenched fraction on projected distance is shown in Figure 2.3. In this model, we define a dwarf to be quenched once it joins the fof group of a host more massive than a threshold $V_{\rm max}$, which we use as a proxy for host halo mass. If we set this minimum host $V_{\rm max}$ to be the minimum $V_{\rm infall}$ required for a halo to be considered a "luminous neighbor", $V_{\rm infall} > 150\,{\rm km\,s^{-1}}$ (shown as a

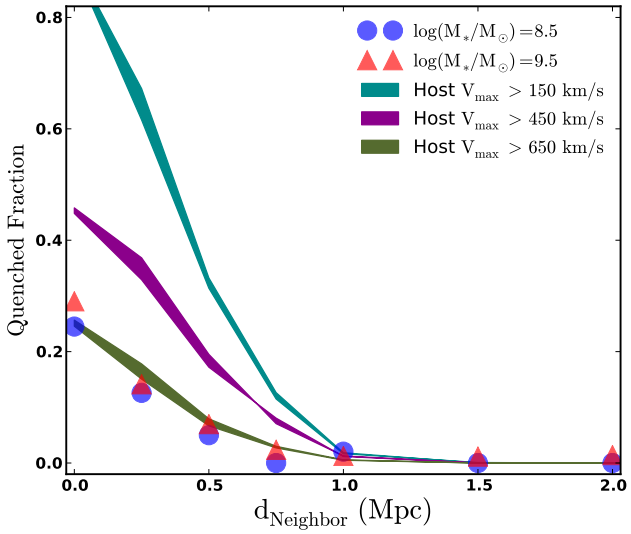

Figure 2.3: The relationship between quenching and host halo mass. Colored bands show the predicted quenched fraction in a model where subhalos become quenched only when their host mass is above a given threshold: $V_{\rm max} > 150\,{\rm km\,s^{-1}}$ (cyan), $> 450\,{\rm km\,s^{-1}}$ (magenta), and $> 650\,{\rm km\,s^{-1}}$ (green). The symbols are the same data points shown in Figure 1. Reproducing the data requires a minimum host $V_{\rm max}$ of $650\,{\rm km\,s^{-1}}$, which is much too large given existing constraints on satellite quenching in lower mass hosts. The thickness of the bands illustrate how our results change as we vary the $V_{\rm infall}$ range used in identifying dwarf galaxy halos, as discussed in §3.

cyan band), we can easily reconstruct the observed quenched fraction of 0 at $d_{\rm Neighbor} > 1-1.5$ Mpc. This is a result of the fact that subhalos this far from their "luminous neighbors" have hosts that are not luminous enough to fall into the "luminous neighbors" category. If the actual hosts were luminous enough, we would have identified them as the "luminous neighbor", and the $d_{\rm Neighbor}$ would reflect this shorter distance to the actual host. This model does, however, have significant trouble reproducing the observed quenched fraction at small $d_{\rm Neighbor}$, with the predicted quenched fraction exceeding 90% for dwarfs with $d_{\rm Neighbor} < 250$ kpc, even when we require the host to have $V_{\rm max} > 150\,{\rm km\,s^{-1}}$.

Only when we restrict quenching to satellites within host halos of $V_{\rm max} > 650\,{\rm km\,s^{-1}}$ is our model able to match the observed quenched fraction. However, this is an unrealistically high value for a $V_{\rm max}$ threshold. Several studies have shown that satellites are quenched in excess of the field when seen around hosts with much smaller halo masses [180, 176, 244]. For example, using a carefully designed sample to target Milky Way size hosts, Phillips et al. [198] find that LMC

size satellites are quenched with an excess of roughly 16% compared to galaxies in the field. Furthermore, our own Milky Way, with a (dark matter) $V_{\rm max}$ less than $220\,{\rm km\,s^{-1}}$ (excluding the disk contribution), has many quenched satellites, as does M31 [167, 173]. We conclude that a simple model whereby a subhalo becomes quenched only after falling within a massive ($V_{\rm max} > 650{\rm km\,s^{-1}}$) host is unrealistic.

It is, perhaps, more plausible that infall time is the primary factor in determining whether a satellite becomes quenched. Models of this kind are popular and physically motivated [52, 273]. Because infall time is linked to distance from the center of the potential well in the host halo, infall time models naturally reproduce observed gradients in color with cluster-centric distance (see Hearin et al. 93, who demonstrate this qualitative result with a more sophisticated model, and Smith et al. 231).

We explore infall time ($\tau_{\rm infall}$) as a quenching parameter by associating subhalos with quenched galaxies based on the time they most recently became a subhalo of another halo in the simulation. In the MS-II database, the last time at which a halo becomes a subhalo is determined by the parameter *infallSnap*: the most recent *snapnum* at which the subhalo went from being at the center of its own friends–of–friends group to being inside another halo's friends–of–friends group. In our $\tau_{\rm infall}$ model, then, a galaxy becomes "quenched" after falling into another galaxy's friends–of–friends (FOF) group and orbiting for a minimum amount of time. Because we use this definition of infall time, in cases where the initial crossing was followed by a subsequent pass outside the FOF group, we specifically associate infall time with the *last time* the subhalo joined the FOF group. However, because the definition is based on FOF group instead of virial radius, some subhalos that pass outside the virial radius of their host but stay within the FOF group will still be counted as subhalos. This should account for some of the "backsplash" galaxies, which Wetzel et al. [272] have concluded should behave very similarly to satellite galaxies in terms of quenching. In cases where the subhalo was originally accreted as a subhalo of something else (e.g. infall into a cluster as part of a group) our definition means that we track the first time the object became a subhalo to

measure infall time.

The results of this model are illustrated in Figure 2.4, where once again we are comparing to the observed quenched fractions from G12 (blue circles and red triangles). Here, the cyan band is the fraction of all dwarfs that are subhalos and that became subhalos over 4 Gyr ago. Within 250 kpc, almost 80% of all dwarfs have been orbiting within their host halos for over 4 Gyr. Nearly 60% have been orbiting for over 7 Gyr, shown as the yellow band. In order to reproduce the observed quenched fraction at small separations ($d_{\rm Neighbor} < 250$ kpc), we must restrict quenching to only those satellites that fell into their host halo more than 9.5 Gyr ago. The quenched fraction that corresponds to this relatively extreme criterion is shown as the green band in Figure 2.4. This quenching timescale is very long, and suggestive of a very inefficient quenching process, more like strangulation than ram-pressure stripping at the virial radius. We discuss this result in relation to other work in Section 2.6.

Alternatively, subhalo quenching may have less to do with crossing the virial radius boundary than it does with a more central encounter, where tidal forces are greater and the hot gas density of the host halo is higher and more effective at ram-pressure stripping. While infall time is partially correlated with halo-centric distance, we explore a model that ties quenching to a parameter that more directly traces the tidal forces experience by a subhalo: the ratio of $V_{\rm max}$ at $z = 0$ to $V_{\rm infall}$. Figure 2.5 shows the results of this model, with the fraction of dwarfs with current $V_{\rm max}$ smaller than 85%, 75% and 65% of their $V_{\rm infall}$ values plotted as cyan, magenta and green bands, respectively. Using this model to define when a satellite galaxy is quenched, we roughly match the observed values using a $V_{\rm max}/V_{\rm infall} = 0.65$ threshold. This corresponds to the satellite having lost roughly 70% of its infall mass, which is perhaps reasonable. At a fixed $V_{\rm max}/V_{\rm infall}$, however, this model has trouble reproducing the observed quenched fractions in detail from $0.5 - 1$ Mpc compared to the fixed infall time model shown in Figure 2.4.

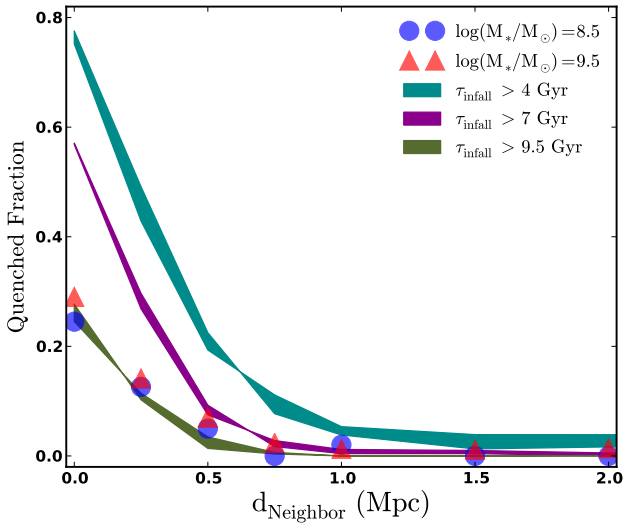

Figure 2.4: The relationship between quenching and infall time. Colored bands show the predicted quenched fraction in a model where subhalos become quenched only after a time $\tau_{\rm infall}$ of orbiting within a host: $\tau_{\rm infall} > 4$ Gyr (cyan), > 7 Gyr (magenta), and > 9.5 Gyr (green). This model works only with rather long quenching timescales, $\tau_{\rm infall} > 9.5$ Gyr. The thickness of the bands correspond to different ranges of $V_{\rm max}$ used to identify dwarf halos, as discussed in §3.

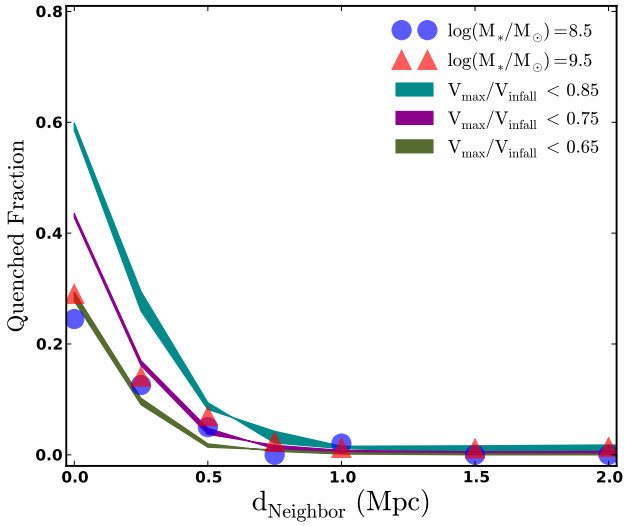

Figure 2.5: The relationship between quenching and mass loss. Colored bands show the predicted quenched fraction in a model where satellites become quenched when their subhalos have been stripped of mass beyond a certain level: $V_{\rm max}/V_{\rm infall} < 0.85$ (cyan), < 0.75 (magenta), and < 0.65 (green). The data are marginally well described by a quenching scenario with $V_{\rm max}/V_{\rm infall} = 0.65$ as the critical scale for star formation cessation. The thickness of the bands correspond to different ranges of $V_{\rm max}$ used to identify dwarf halos, as discussed in §3.

2.5 Summary

We have used mock observations of the MS-II simulation [35] in order to interpret dwarf galaxy ($M_\star \simeq 10^9$ $M_\odot$) quenching as a function of projected distance to a more luminous neighbor as observed by Geha et al. [82, G12]. Dwarfs of this mass are particularly useful as a test bed for environmental quenching because, as shown by G12, they are never (or almost never) quenched in isolation.

We show that while dwarfs within 250 kpc and 1000 km s^{-1} of a luminous neighbor are subhalos of a larger host approximately 90% of the time, only about 25–30% of such dwarfs are quenched (suggesting that $\sim 30\%$ of subhalos are quenched at these masses). The implication is that whatever is giving rise to subhalo quenching, the process must be fairly inefficient, at least when evaluated relative to the subhalo population as a whole.

We investigate a model in which dwarfs become quenched only after a time $\tau_{\rm infall}$ of being accreted into a larger host. The required quenching timescale is quite long, 9.5 Gyr (cf. Figure 2.4), compared to some estimates in the literature (see §2.6). Alternatively, if dwarf quenching is instead related to the tidal forces experienced by the subhalo, then a simple model in which dwarfs with $V_{\rm max}/V_{\rm infall} < 0.65$ become quenched does a reasonable job in reproducing the observed quenched fraction in the innermost bin of G12 (see Figure 2.5), though in detail the infall time model provides a better match overall (Figure 2.4). If, instead, we try to explain the relatively low quenched fraction for subhalos by demanding that only hosts larger than a critical $V_{\rm max}$ are able to quench their satellites, we find that a threshold $V_{\rm max}$ of 650 km s^{-1} is required. This value is unreasonably high, as it is well above that of isolated galaxy size hosts that are known to quench at least some of their satellites [180, 176, 244, 198].

Of course, quenching is likely a complicated process that depends on more than a single parameter. Our aim in this work is to focus on simple models in order to gain qualitative insight, though we also explore slightly more complicated cases in which two conditions must be met before

quenching occurs. Combining a minimum host $V_{\rm max}$ with a maximum ratio of $V_{\rm max}/V_{\rm infall}$ does not significantly change the required values for either parameter. A minimum host $V_{\rm max}$ of 350 km s^{-1} only moves the best fit threshold ratio to $V_{\rm max}/V_{\rm infall} = 0.70$, which is not significantly larger than the required one-parameter model value of 0.65. We also investigate a model that requires both a minimum host $V_{\rm max}$ as well as a minimum $\tau_{\rm infall}$ for a satellite to become quenched. However, even requiring the relatively high host $V_{\rm max}$ lower limit of 350 km s^{-1} does not reduce the required infall time significantly. We estimate that these joint criterion for quenching will lead to a reduced threshold quenching timescale of $\sim$ 7.5 Gyr. Finally, combining $V_{\rm max}/V_{\rm infall}$ and $\tau_{\rm infall}$ does not significantly change the required values for either parameter. This is due to the large amount of overlap between subhalos that have lost a certain fraction of their $V_{\rm infall}$ and those that have been orbiting within the virial radius of their hosts for a minimum amount of time.

2.6 Discussion

Applying a semi-analytic scheme that models the evolution of central and satellite galaxies separately, while determining the quenching timescales for each by matching the observed quenched fractions in the SDSS, Wetzel et al. [273] conclude that infall time is the main determinant with regard to satellite quenching. Wetzel et al. [273, hereafter W13] focus on satellite galaxies that are more massive than the dwarfs considered in this work. Their sample has a minimum satellite mass of $M_\star \sim 5 \times 10^9$ M$_\odot$, compared to $M_\star \sim 3 \times 10^9$ M$_\odot$ as the midpoint of the most massive stellar mass bin we consider for our dwarfs. W13 find that satellite galaxies experience "delayed-then-rapid" quenching, becoming quenched rapidly (within an e-folding time of 0.8 Gyr) only after having orbited their hosts for $\sim$ 2–4 Gyr. This translates into an overall quenching timescale of $\sim$ 3–5 Gyr, a value much less than the 9.5 Gyr determined in this work.

The 3–5 Gyr quenching timescale adopted by W13 is roughly comparable to one of our models, in which we assume a required infall time of 4 Gyr before quenching; this is illustrated by the cyan

band in Figure 2.4. However, this model yields a quenched fraction within 250 kpc of a "luminous neighbor" that is nearly quadruple that observed by G12. Furthermore, W13 count $\tau_{\rm infall}$ as the time since the satellite *first* fell into any host dark matter halo, while we use the time since the satellite most recently became a subhalo of *any* host. This difference in the definition of infall time dictates that our infall times will always be shorter than those inferred by W13 and thereby only serves to make the contrast between their results and our work more stark.

However, it is important to emphasize the different mass ranges investigated by W13 and our work. It is possible that invoking a simple (satellite) mass dependence in the quenching timescale could serve to largely eliminate the discrepancy between the two results. According to Figure 8 of W13, the quenching timescale becomes longer for less massive satellites. Their inferred quenching timescale nearly triples for satellites in their lower mass range, reaching ~ 6 Gyr for satellites with $M_\star \sim 5 \times 10^9$ $\mathrm{M}_\odot$ compared to ~ 2 Gyr for satellites with $M_\star \sim 10^{11}$ $\mathrm{M}_\odot$.

Quenching timescales found by De Lucia et al. [52, hereafter D12] also suggest a dependence of the quenching timescale on satellite mass. Using methods very similar to our own, they investigate mock observations of quenched fractions by testing simple models for quenching and comparing to observation. D12 find a quenching timescale of $5 - 7$ Gyr for satellite galaxies in a sample with stellar mass $10^9 < M_\star/\mathrm{M}_\odot < 10^{11}$. This mass range overlaps with ours slightly, which makes it unsurprising that they determine a timescale that is more similar to ours and to that determined by W13 for their lowest satellite stellar mass bin. However, D12 use yet another definition for infall time: the time since a satellite first fell into its *current* host (we use the time it last became a subhalo of anything). By definition, the timescale employed by D12 will always be less than or equal to the timescale employed by W13, but could be shorter or longer than ours depending on the merger history of the satellite in question. For example, if a galaxy becomes a satellite of a host, and then that host iself is accreted onto a larger system, the timescale would be longer according to our definition than that of D12.

In the context of a model where infall time is the determining factor in satellite quenching, there ap-

pears to be a qualitatively consistent trend in the literature that lower mass satellites require longer timescales for quenching. This result begs the question: how is it that the smallest galaxies, which are presumably the most fragile, require the longest periods of time to become quenched? We speculate that this can only work in a "slow starvation" scenario, whereby gas-rich yet inefficiently-star-forming dwarfs continue to form stars for a long time after their supply of fresh or recycled gas is shut off. This possibility is consistent with the well-known fact that dwarfs have much higher gas fractions (and longer star formation timescales) than more massive galaxies [101, 258, 81, 269]. If we consider the possibility that the quenching timescale is related to the gas depletion timescale, this would imply that this timescale should also increase with decreasing stellar mass.

Observationally, however, the mass dependence of the gas depletion timescale remains fairly cloudy, especially for low-mass systems. Based on measurements of atomic hydrogen in local star-forming galaxies, gas depletion timescales are generally found to increase with decreasing stellar mass [228, 221]. More recent studies, however, show that star formation is a direct product of the molecular gas in a galaxy, not of all gas. In particular, on sub-kpc scales, current star formation is found to correlate strongly with molecular gas and poorly with atomic gas [283, 121, 153, 22]. Moreover, recent measurements of CO emission in nearby galaxies find that the molecular gas depletion timescales are constant, or possibly even decreasing in lower stellar mass systems [153, 85, 23, 211, 28]. For systems with stellar mass less than 10^9 $M_\odot$, however, the constraints are generally weak due to the difficulty of detecting CO emission in low-mass systems — a limitation that will hopefully soon be overcome for larger samples using more sensitive facilities such as ALMA.

Regardless of the underlying cause, our results indicate that dwarf satellites in the $M_\star \sim 10^{8.5-9.5}$ $M_\odot$ mass range are quenched only $\sim$ 25–30% of the time. However, for more massive satellites there is quenching in the field, and so the quenched fraction is not the same as the fraction of satellites that are quenched because they are satellites. Thus, a proper comparison of environmental quenching over different stellar mass regimes is best made by comparing only the "environmentally quenched

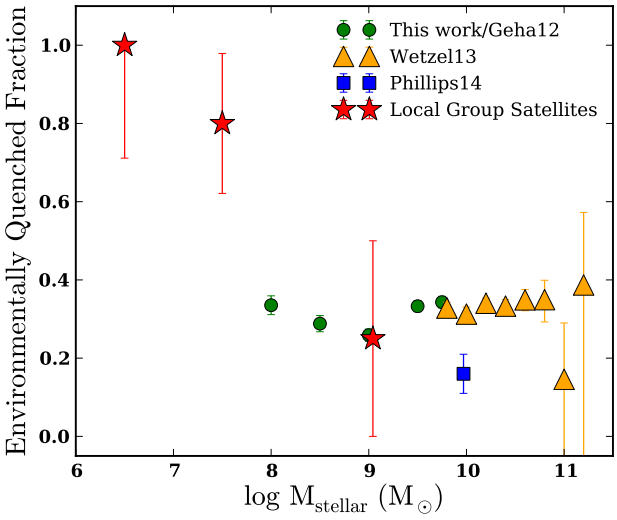

Figure 2.6: The environmentally quenched fraction – the fraction of satellites that are quenched in excess of that expected in the field, i.e. the fraction of satellites that are quenched because they are satellites. We see that while environmental quenching seems to have an approximately constant efficiency of $\sim$ 30% at stellar masses from 10^8 to 10^{11} $M_\odot$, there appears to be a dramatic upturn in quenching at lower stellar masses (if the Local Group is typical).

fraction". This is the fraction of satellites that are quenched but would have otherwise not be quenched in the field, and so is equivalent to the overall quenched fraction for low mass galaxies. Our "environmentally quenched fraction" is largely equivalent to the "transition fraction", $f_{tr|s,bc}$, first introduced by van den Bosch et al. [256], as well as to the "conversion fraction", $f_{convert}$, of Phillips et al. [198] and the "excess red fraction", f^{Q}_{excess}, of Wetzel et al. [273], the latter two of which are plotted in Figure 2.6 alongside our quenched fraction. As Figure 2.6 shows, over the stellar mass range 10^8–10^{11} $M_\odot$, the environmentally quenched fraction is almost completely independent of stellar mass. The yellow triangles show results from Wetzel et al. [273], for which satellite galaxies reside typically in clusters. The green points are taken from our G12 sample, and include only systems with $d_{Neighbor} < 250$ kpc, which again typically reside in small clusters (Figure 2.3; and we have taken into account the fact that only $\sim$ 90% of the galaxies in this bin are true subhalos, Figure 2.1). The Phillips et al. [198] point (blue square) is somewhat different in that these galaxies were chosen to reside within Milky-Way size hosts rather than clusters. This may explain the slightly lower environmentally quenched fraction. The results displayed here are consistent with other results suggesting that quenching efficiency is independent of stellar mass

[256, 197, 242].

Although the statistics for satellites in the stellar mass range $M_\star \sim 10^{8.5-9.5}\,\mathrm{M}_\odot$ within the Local Group are very low, it is interesting that the quenched fraction for these dwarfs is not too far from $\sim$ 25–30%. Within this mass range, the LMC, the SMC and M33 are star-forming while NGC 205 and M32 are quenched. Once we adjust the quenched fraction to the environmentally quenched fraction by accounting for the fraction of quenched galaxies at this mass in the field, the fraction of high mass satellites of the Milky Way and M31 that have been quenched as satellites is broadly consistent with the results of this work. This can be seen in Figure 2.6, where the high mass Local Group satellites have been represented by a point placed at the mean of their stellar mass values.

This consistency of the environmentally quenched fraction over so many orders of magnitude is particularly puzzling in light of the known (very high) quenched fraction of dwarf satellites in the Local Group in the mass range just below $M_\star \simeq 10^8\,\mathrm{M}_\odot$ [167, 173]. The low mass Local Group points in Figure 2.6 show a marked increase in the environmentally quenched fraction just below $10^8\ \mathrm{M}_\odot$. Furthermore, observations of the nearby group M81 show that almost all of the low mass satellites of that group are also quenched [109, 113]. Recall that at these low stellar masses, the overall quenched fraction is equivalent to the environmentally quenched fraction, since nearly all isolated systems are star-forming. Of course, most of the quenched dwarf satellites in the Local Volume are of significantly lower stellar mass than those in G12 sample, but if stellar mass is the determining factor, it requires a reversal of sorts: rather than continuing the trend of longer quenching timescales for lower mass galaxies as discussed above, the high quenched fraction of low mass dwarfs in the Local Group suggests a sudden uptick in quenching efficiency below $M_\star \sim 10^8\,\mathrm{M}_\odot$ (see Phillips et al. 2014b *in prep.* for more on this). It is possible that we are seeing a second physical process for quenching emerging in the low-mass dwarf regime: ram-pressure stripping, which should act more efficiently on systems with shallow potential wells, might well be at work. Future observations that probe this lower stellar mass regime with greater statistical samples will be required to determine whether the physics of satellite quenching transitions at

the dwarf spheroidal mass scale from processes that act inefficiently to those that squelch star formation almost uniformly.

Chapter 3

The Existence and Star Formation Histories of Satellites of Dwarfs

3.1 Introduction

If ΛCDM is correct, then all dark matter halos hosting galaxies – from those hosting dwarfs to those hosting giant clusters – should be filled with substructure [178, 132, 287]. Dark-matter only simulations over a vast range of particle masses and physical scales show that substructure persists down to the resolution limit of ΛCDM simulations [57, 158, 234, 35, 133]. The basic expectation is that the mass function of subhalos rises steadily to masses well below the molecular cooling limit of $M_{\rm halo} \sim 10^6\,{\rm M}_\odot$ [239], with thousands of sites for potentially star-forming satellites.

Observations of our own Milky Way, on the other hand, have revealed the presence of only ~ 30 confirmed satellite galaxies [281, 173, 13], the faintest of which, until very recently [162, 129], were all discovered by the Sloan Digital Sky Survey (SDSS) [279, 280, 88, 212, 106, 265, 89, 289, 290, 16, 15, 12, 14, 13]. However, the SDSS covers only a fraction of the sky and is incomplete to the most distant and faintest satellites of the Milky Way. Any solution to the mismatch between

the predicted abundance of subhalos and the observed counts of satellite galaxies around our own Milky Way will likely involve the discovery of ultra-faint satellites in unprobed regions of the sky, at large distances, and with surface brightnesses low enough that they lie just outside current detection limits [19, 209, 139, 245, 40]. Over the last several years, searches by PanSTARRS and VST ATLAS have failed to lend critical support to this idea – finding far fewer dwarf galaxy satellites than expected [148, 159]. However, the recent discovery of up to nine new ultra-faint satellites in the southern sky by the Dark Energy Survey [DES, 241, 140], other recent detections [147, 162, 124] and confirmations [129] of faint dwarf satellite candidates, and ongoing efforts to discover dwarfs at large distances [246] provide an exciting glimpse into the near future and point to a much larger population of as-yet-undiscovered dwarf galaxies in the Local Volume.

Interestingly, most of the newest Milky Way satellite candidates were all discovered near the Large Magellanic Cloud (LMC). While this could be nothing more than a location-based selection effect (the LMC happens to lie next to the region probed by the year one data release of DES), Deason et al. [54] show that several of the candidates could very well be satellites of the LMC, and their discovery highlights the potential for discovering ultra-faint satellites of other more massive dwarf satellites, or of isolated dwarf galaxies in the Local Group. The scale-free nature of the subhalo mass function in ΛCDM suggests that groups of subhalos should be common [178, 154, 271]. Because low-mass halos form earlier, are denser, and fall into smaller hosts before larger ones [186], it is likely that satellites of satellites or of lower mass isolated halos may have survived longer than their counterparts that fell directly into the Milky Way [57]. This suggests that one way to search for ultra-faint galaxies might be as satellites of known dwarf galaxies. Associations and pairs of satellite galaxies in the Local Group have been observed for some time [252, 12, 61, 137, 51, 102, 68], and several Milky Way satellites are suspected to host their own satellites [194, 53].

Once a group of satellites falls into the Milky Way, however, tidal forces will eventually disassemble the group and wipe out evidence of coherent structure [213, 54]. Isolated massive dwarfs in

the Local Group may serve as complementary targets in the hunt for ever-fainter dwarfs (which presumably probe the lowest mass dark matter subhalos). Bovill & Ricotti [31] suggest that even already-merged satellites of isolated dwarfs could be detected as "ghost halos" of ancient stellar populations surrounding their hosts. Despite the obvious challenge of detecting ultra-faints at large distances, isolated dwarfs also make efficient use of telescope pointings, removing some of the chance inherent in any random ultra-faint search without losing any of the search volume. In the near future, large-area, deep-sky surveys such as LSST, DES, PanSTARRS, and SkyMapper will push current detection limits to lower surface brightness and may be able to see ultra-faint satellites of isolated dwarf galaxies if they exist [107, 108, 120].

Dynamical measurements of most Milky Way dwarf spheroidals (dSphs) show that, despite having luminosities that vary over nearly five orders of magnitude, they have almost the same central densities, comparable to dark matter halos with $M_{\rm peak} \sim 3 \times 10^9$ $M_\odot$ [238, 84, 282]. This result is surprising, as the mass function of potentially star forming subhalos rises steeply towards low masses in ΛCDM models. Segue 2 may be the first of these long-searched-for small subhalos to be identified [126], as it appears to have a total dark matter mass $\lesssim 10^8\,M_\odot$. However, based on its metallicity, Kirby et al. [126] hypothesize that Segue 2 is a bare remnant of a much larger galaxy that has been severely tidally stripped. The common central density for observed dSphs might signify a low-mass cutoff in galaxy formation. Halos with slightly lower central densities may have been unable to shield themselves from the reionizing background, perhaps due to having a lower baryon fractions than their denser counterparts [175]. Alternatively, Bullock et al. [40, hereafter B10] suggest that the apparent common mass scale could be a selection effect, and that a large population of unobserved "stealth galaxies" may reside in halos with masses just below those that host observed dwarfs. These low-mass halos have shallow potential wells, and therefore the galaxies that form within them have larger effective radii and lower surface brightnesses, allowing them to more easily avoid detection [115, 40, 30, 31].

The number of these stealth galaxies expected to exist is sensitive to the presence of a low-mass

cutoff in galaxy formation, as the lowest mass halos are expected to host the "puffiest" galaxies in this picture. The heating of accreted gas or the prevention of gas accretion by the ambient ionizing UV background – created when the first galaxies formed – can arrest or prevent star formation in the smallest dark matter halos, suggesting a threshold in halo mass below which all halos remain dark [64, 233, 20, 144, 209, 177, 237, 225, 158]. It is possible, however, that some very low mass halos were able to form some Population II stars *before* reionization [39]. If star formation ceased after this time, it would cause them to have uniformly ancient stellar populations [209, 18] with extremely low metallicity [29, 208]. Remarkably, this appears to be the case with the known ultra faint dwarfs of the Milky Way [37].

Several authors have shown that photoheating prevents gas from condensing in halos with masses that lie just below or at the common halo mass scale for Milky Way satellites [192, 187, 220, 222]. However, the specific timing of the onset and end of reionization, the spectrum of the background radiation, the ability of gas to temporarily shield itself from these high energy photons, and particularly the mass resolution, can have a large effect on the number and minimum halo mass of galaxies in any simulation [64, 58, 95, 188]. Moreover, prescriptions for how stars and supernovae return energy back to the interstellar medium (ISM) will affect the formation history of small galaxies in the presence of an ionizing background.

In what follows, we present a series of simulations of galaxy formation within small dark matter halos run with the `Gizmo` code [97] in "PSPH-mode" [96]. `Gizmo` implements the Feedback in Realistic Environments (FIRE) [98] feedback scheme for converting gas into stars and capturing the energy fed back from those stars into the surrounding medium. Using these simulations, we find that the subhalos of the halos that surround $M_\star \sim 10^6$ $M_\odot$ dwarf galaxies should form stars fairly abundantly, and produce potentially observable ultra-faint satellite galaxies of known classical dwarfs in the Local Group. Further, the ultra-faint dwarfs in our simulations with $M_\star = 3 - 30 \times 10^3$ $M_\odot$ that form in isolation or as satellites within subhalos of $M_{\rm peak} \simeq 0.5 - 3 \times 10^9\,M_\odot$ all have completely ancient stellar populations, as is seen for the known population of the Milky Way. They

also have low-surface brightnesses, as expected for "stealth galaxies" forming in halos of these low masses, but may be within the detection capabilities of future surveys.

This paper is organized as follows: in Section 3.2, we give the details of our simulations, including halo finding and merger-tree analysis. Section 3.3 outlines our main results, including the $M_\star - M_{halo}$ relation for our galaxies and their star formation histories. In Section 3.4, we use the Exploring the Local Volume in Simulations (ELVIS) suite of dark-matter-only Local Group simulations [80] to determine how common these objects should be and the likelihood of their detection. We compare to several recent works in Section 3.5, and summarize our results and conclude in Section 3.6.

3.2 Simulations

We present six cosmological zoom-in simulations of four isolated dwarf galaxy halos using two implementations of subgrid physics. The four host halos are Dwarf 1 and Dwarf 2, which have $z = 0$ virial masses of $M_{\rm vir} \simeq 10^{10}$ $M_\odot$; and UFD 1 and UFD 2, which have $M_{\rm vir} \simeq 10^9$ $M_\odot$ (see Table 1 for precise numbers; in this paper we define the virial overdensity using the spherical top hat collapse approximation of Bryan & Norman 38). The Dwarf 2 halo was simulated three times – two runs varied the specific subgrid feedback implementation, while the third used a different choice of gravitational softening (see below), resulting in changes in the star formation histories of the main galaxies (see Oñorbe et al. 188 for details). We refer to these three cases as Dwarf $2_{\rm Early}$ (run with the fiducial parameters – the same parameters as Dwarf 1, UFD 1, and UFD 2), Dwarf $2_{\rm Middle}$, and Dwarf $2_{\rm Late}$. The subscripts refer to when the halos formed most of their stars (see Figure 3.3). Every run has a dark matter force softening of 25 to 35 pc and a dark matter particle mass of $m_p^{\rm dm} = 1.26 \times 10^3\,M_\odot$ except UFD 2, which uses $m_p^{\rm dm} = 2.46 \times 10^3\,M_\odot$. The UFD 1 and three Dwarf 2 simulations are identical to the "Ultrafaint" and Dwarf runs presented by Oñorbe et al.

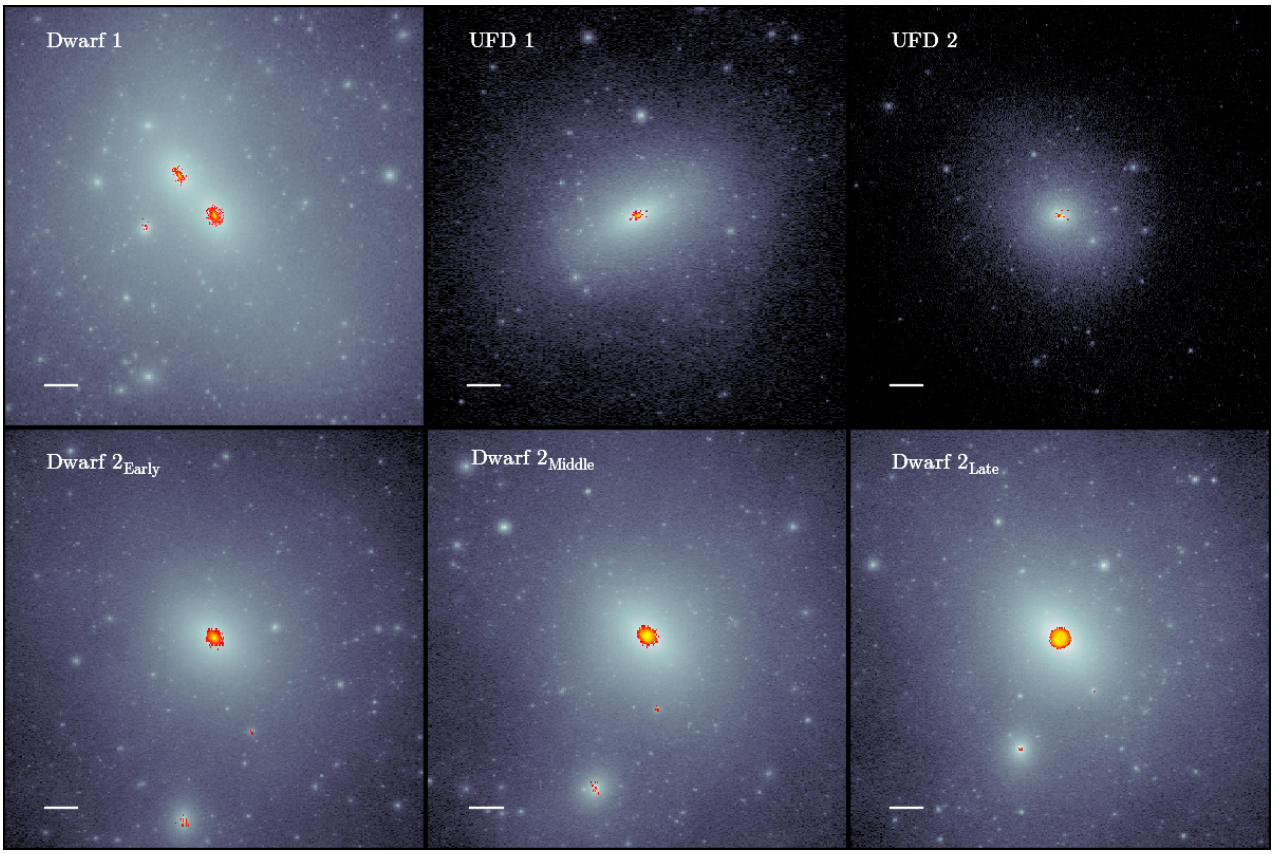

Figure 3.1: Projected ($x-y$ plane) visualizations for all of the runs presented in this work. From left to right, the top three panels visualize Dwarf 1, UFD 1 and UFD 2, while Dwarf $2_{\rm Early}$, Dwarf $2_{\rm Middle}$ and Dwarf $2_{\rm Late}$ are shown in the lower panels. The dark matter distribution is shown in greyscale, while the stellar density is pictured in color for all subhalos with $M_\star > 3 \times 10^3$ $M_\odot$ (in at least one run in the case of Dwarf 2; see text for details). $M_\star$ is calculated as the stellar mass within the inner 3 (1.5) kpc of the central (satellite) galaxy. The white line in the lower left of each panel represents 5 kpc.

[188].[1]

The initial conditions were generated using `MUSIC` [92], and selected from a cosmological box run at low resolution to $z = 0$. Dwarf 1, Dwarf 2, and UFD 1 were all selected from 5 h^{-1} Mpc boxes to have typical values of spin parameter λ, concentration, and formation time for their mass range, and also to have small Lagrangian volumes [189]. UFD 2 was selected from a 25 h^{-1} Mpc box and required to have no other halos of 50% or more of its mass within 4 $R_{\rm vir}$ at $z = 0$ and a small Lagrangian volume. All dwarfs in this work are isolated. Once the halos are identified, the

[1]Note that UFD 1 and Dwarf $2_{\rm Early}$ were also previously presented in Hopkins et al. [98] as m9 and m10 respectively.

particles are traced back in time and an enclosing Lagrangian volume is chosen and re-simulated at higher resolution with dark matter and gas, buffered by dark matter-only regions of increasing particle mass. This process is done according to the zoom-in techniques outlined by Katz & White [114], Oñorbe et al. [189] and with the goal of minimizing low resolution particles within the halos of interest. All simulations begin at a redshift of $z = 125$ and have 0% contamination from low resolution particles within a distance of 1.6 $R_{\rm vir}$ at all redshifts.

All simulations were run using the fully conservative cosmological hydrodynamic code `Gizmo` [97] in "PSPH-mode". This code adopts the Lagrangian "pressure-entropy" formulation of the smooth particle hydrodynamic (SPH) equations, ameliorating previous difficulties SPH codes had in modeling multiphase fluids [2]. For feedback and star formation we use the Feedback in Realistic Environments (FIRE) scheme [98]. FIRE tracks momentum imparted locally from stellar radiation pressure, radiation pressure on larger scales via the light that escapes star-forming regions, HII photoionization heating, supernovae (Type I and II) heating, momentum and mass loss and stellar winds from O-type and AGB stars. Each star particle has an age determined by its formation time, an initial mass function (IMF) taken from Kroupa [145], and a metallicity inherited from its parent gas particle. The star particle then loses mass and creates metals according to the `STARBURST99` stellar population synthesis model [151] and the input IMF. Our simulations use an ambient ionizing UV background from Faucher-Giguère et al. [69], which starts at $z = 10.65$ and completes reionization by $z \simeq 6$.

The FIRE implementation has as few free parameters as possible, with star formation in the multiphase ISM naturally self-regulating. Giant molecular clouds (GMCs) form, and then are subsequently heated and disrupted by the stars that form within the self-gravitating, molecular gas. In order to ensure that the gas within the GMCs reaches a density high enough to form stars ($n > 100$ cm^{-3}), the code requires extremely high mass and spatial resolution. Every run uses a gas particle mass of $m_p^{\rm gas} = 255$ M$_\odot$ except for UFD 2, which uses $m_p^{\rm gas} = 499$ M$_\odot$. The gas force resolution varies from $\epsilon_{\rm gas}^{\rm min} = 1.0 - 2.8$ pc in all runs except one version of Dwarf 2 (see below).

The Dwarf 2_{Early} run uses the fiducial subgrid parameters. In Dwarf 2_{Middle} and Dwarf 2_{Late}, mass, momentum, and energy are deposited to particles within the SPH kernel according to a mass-weighting scheme, rather than volume-weighting as in the fiducial runs. In addition to this change, Dwarf 2_{Middle} was run to test equal softening lengths for the dark matter and the gas (25 pc). All three runs of Dwarf 2 end up with stellar masses in the central galaxies (defined as the stellar mass enclosed within the central 3 kpc) that differ by only $\sim 25\%$, suggesting that the major differences between the runs are more a result of stochasticity than the changes to the feedback implementation and softening length (see Section 3.2.1).

We use the Amiga Halo Finder [AHF, 134] to identify gravitationally bound dark matter, stellar and gas particles in each snapshot of the simulation. Because pure particle-matching algorithms generally underperform relative to more sophisticated methods in terms of detection and removal of spurious interlopers between snapshots [235], we track particle overdensities between simulation snapshots using the `consistent-trees` software [11]. This is particularly important given our focus on subhalos. Because the current stable version of `consistent-trees` – which makes use of the ROCKSTAR [10] halo finder – does not track baryonic particles, we build a pipeline between AHF and ROCKSTAR that allows for a seamless transition between the AHF halo catalogs and the merger trees. This pipeline uses the halo phase space information combined with the dark matter particle IDs to match each halo in the catalogue to a `consistent-trees` merger tree. ROCKSTAR and `consistent-trees` were used to determine the peak virial mass and infall times for subhalos. All other halo, galaxy and stellar quantities were obtained from the AHF halo catalogs or the raw particle files.

All runs were initialized and simulated assuming the WMAP-7 cosmology $\sigma_8 = 0.801$, $\Omega_\Lambda = 0.734$, $\Omega_m = 0.266$, $\Omega_b = 0.0449$, $n_s = 0.963$ and $h = 0.71$ [138]. Further detail on the FIRE/`Gizmo` code can be found in Hopkins et al. [98], Hopkins [97].

	Dwarf 1	Dwarf $2_{\rm Early}$	Dwarf $2_{\rm Middle}$	Dwarf $2_{\rm Late}$	UFD 1	UFD 2
Central						
$M_{\rm vir}$ (10^9 M$_\odot$)	11.1	7.8	7.7	7.6	2.5	1.1
$M_\star$ (10^3 M$_\odot$)	620	2200	2700	2800	22	8.5
1st Satellite						
$M_{\rm peak}$ (10^9 M$_\odot$)	4.7	0.70	0.68	0.64	0.03	0.02
$M_\star$ (10^3 M$_\odot$)	220	4.2	5.4	2.9	(0.9)	(0.7)
2nd Satellite						
$M_{\rm peak}$ (10^9 M$_\odot$)	0.51	0.04	0.04	0.04	0.02	0.007
$M_\star$ (10^3 M$_\odot$)	5.0	(0.7)	(3.5)	(0.6)	(0.6)	(0.4)

Table 3.1: Halo and stellar masses of all central galaxies and their 1st and 2nd satellites from all six simulations. For all simulations except Dwarf $2_{\rm Early}$ and Dwarf $2_{\rm Late}$, the 1st and 2nd satellites refer to the first and second most massive satellites in stellar mass. The 2nd Satellites for Dwarf $2_{\rm Early}$ and Dwarf $2_{\rm Late}$ are selected because their counterpart within Dwarf $2_{\rm Middle}$ has $M_\star > 3 \times 10^3$ M$_\odot$. Both satellites in Dwarf 1 and the 1st satellites in all Dwarf 2 runs are "massive satellites" (see text). The stellar masses of all other satellites are shown in parentheses.

3.2.1 Sample Details

Figure 3.1 shows the dark matter distributions of all six runs in greyscale with the stellar mass density overlaid in color. The physical scales of the panels are identical: the white line in the lower left corner of each visualization indicates 5 kpc.

For our detailed analysis, we focus on objects with $M_\star > 3 \times 10^3$ M$_\odot$ in order to avoid effects from spurious star formation at our resolution limit. The gas density required to form stars in our simulations is quite high and can only occur in dense, molecular, self-gravitating regions. This onerous minimal criteria suggests that the formation of this minimum stellar mass represents a physical star formation episode.[2] Furthermore, we find that below a subhalo mass of $M_{\rm peak} \sim 5\times10^8$ M$_\odot$ our results become far less stable against the stochasticity in star formation (see below). We therefore consider only as robust those objects that form within halos that have a minimum dark matter particle number $N_p^{\rm dm} \geq 2 \times 10^5$ and refer to satellites that meet both this requirement and the stellar mass cut as "massive satellites".

[2]All galaxies that meet our minimum $M_\star$ requirement have at least 16 star particles and had $\gtrsim 3 \times 10^4$ dark matter particles at peak mass. All but one had $\gtrsim 2 \times 10^5$ dark matter particles at peak mass, corresponding to typical initial baryonic particle numbers of $\sim 3 - 4.5 \times 10^5$ before feedback dispelled most of these.

Dwarf 1 has two satellite galaxies that meet both of these requirements. Only one subhalo – the most massive in each of the runs of Dwarf 2 – forms a "massive satellite". In Dwarf $2_{\rm Middle}$ there is a second satellite that meets the stellar mass but not the dark matter particle number cut. Because all three runs of Dwarf 2 use identical initial conditions, each subhalo in Dwarf $2_{\rm Middle}$ has a corresponding subhalo in the other runs that shares a majority of the dark matter particles. The subhalos corresponding to this second satellite host galaxies below the stellar mass cut in Dwarf $2_{\rm Early}$ and Dwarf $2_{\rm Late}$. In Figure 3.1, stars are shown in this particular subhalo for all three runs of Dwarf 2. Importantly, although the three subhalos that host the second satellites of Dwarf 2 are effectively identical, they produce galaxies that differ by a factor of ~ 6 in stellar mass due to only minor changes in parameters between the runs. This motivates the fairly large dark matter particle number we require to consider a system well resolved.

$M_{\rm halo}$ and $M_\star$ for the central galaxy (Central), most-massive satellite (1st satellite), and second-most-massive satellite (2nd satellite)[3] in all six runs can be found in Table 1. In the Tables, Figures and throughout the text, $M_{\rm halo}$ is $M_{\rm vir}$ for centrals and $M_{\rm peak}$ for satellites. Values in parentheses indicate satellite systems that we regard as too poorly resolved to trust for detailed analysis. They are included here for completeness. The 2nd satellites of all Dwarf 2 runs fall into this category, as well as all satellites of the isolated ultra-faints UFD 1 and UFD 2.

In Figure 3.1, the dark matter distribution is shown for all dark matter particles located within 65% of the virial radius of the halo listed in each panel. Star particles are only shown if they reside within any halo that currently has $> 3 \times 10^3$ $M_\odot$ in stars in the inner 3 (1.5) kpc of a central (satellite) galaxy or are in a corresponding halo in the other two runs of Dwarf 2. Many of the other subhalos also contain star particles (see Figure 2), but they are not shown so that we may focus on systems that are reasonably well resolved. The radial extent of the galaxies was chosen by inspecting their stellar mass profiles (each central galaxy also has a *very* diffuse stellar halo that

[3]In all cases except Dwarf $2_{\rm Early}$ and Dwarf $2_{\rm Late}$, the 2nd satellite is the second most massive satellite in stellar mass. In these two runs only, the 2nd satellites are selected as the satellites that correspond to the high stellar mass outlier in run Dwarf $2_{\rm Middle}$. Only the 1st satellites in Dwarf 2 runs qualify as "massive satellites".

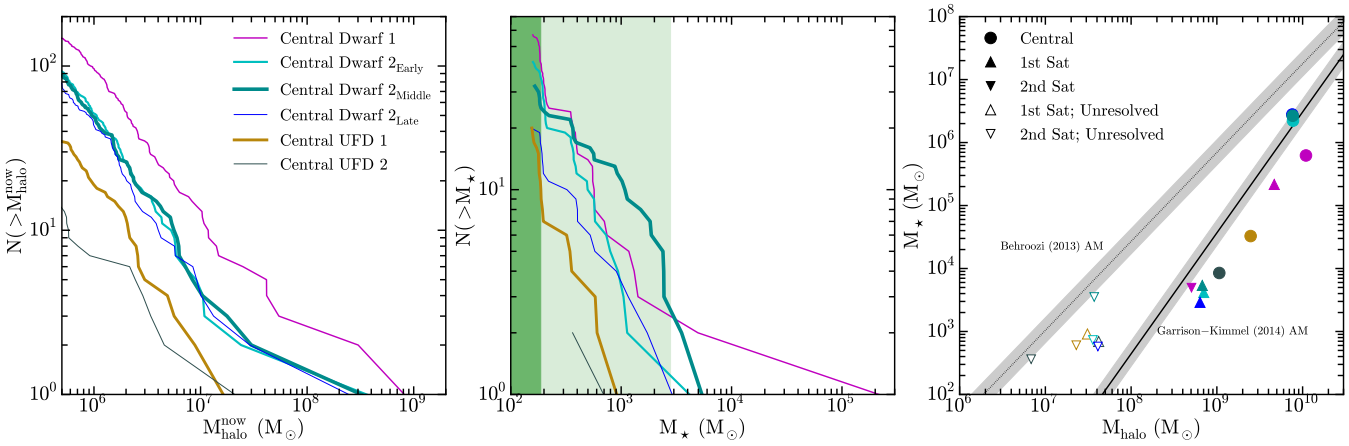

Figure 3.2: Left: Subhalo mass function for all six runs. $M_{\rm halo}^{z=0}$ is the present day mass for all subhalos. For reference, $M_{\rm halo}^{z=0}$ is typically about a factor of 2 smaller than $M_{\rm peak}$. The left edge of the panel corresponds to ~ 400 bound dark matter particles. Note: if these halos simply contained the universal fraction ($f_{\rm b} = 0.169$) of baryons, this would correspond to $\gtrsim 350$ baryonic particles in these halos before they were forcefully removed by feedback. Middle: Stellar mass function for all satellites that form at least one star particle. The average mass of a single star particle is shown as a dark green band. Masses we regard as poorly-resolved ($M_\star < 3 \times 10^3$ M$_\odot$) are highlighted by the light green region. Right: $M_\star - M_{\rm halo}$ for all Centrals (filled circles), 1st and 2nd satellites (upward and downward triangles respectively). With surprisingly little scatter, our isolated dwarfs and their six well-resolved satellites (filled triangles) sit just offset from the extrapolated abundance matching relation from Garrison-Kimmel et al. [80] (solid black line). Both this and the abundance-matching relationship from Behroozi et al. [8] (dotted black line) are shown with 0.2 dex in scatter. Open symbols correspond to poorly resolved galaxies: $M_\star < 3 \times 10^3$ M$_\odot$ and/or $N_p^{\rm dm} < 2 \times 10^5$.

we aim to avoid). The galaxy stellar masses are all computed using these radial limits.

3.3 Results

In all six runs, the dark matter halos hosting the central galaxies contain significant substructure. The leftmost panel of Figure 3.2 shows the current subhalo mass function for all six runs. We plot $M_{\rm halo}^{z=0}$ rather than $M_{\rm peak}$ in order to capture a snapshot of the halo populations as they currently exist. For reference, $M_{\rm halo}^{z=0}$ is typically about a factor of 2 smaller than $M_{\rm peak}$. Only subhalos with $M_{\rm halo}^{z=0} > 5 \times 10^5$ M$_\odot$ are plotted, which corresponds to $N_p^{\rm dm} \gtrsim 400$. Dwarf 1, with the highest virial mass, has both the greatest number of and the most massive subhalos. The subhalo mass functions

for the three runs of Dwarf 2 lie predictably on top of each other. As expected, the two isolated "ultra-faints" ($M_{\rm vir} < 3 \times 10^9$ M$_\odot$) form far fewer subhalos (at fixed mass) than their more massive counterparts. In Dwarf 1 and Dwarf 2, the 1st satellites form in subhalos that are a fairly large fraction of their hosts' masses when compared to the mass ratios for the most massive subhalos in the two "ultra-faint" runs. This is likely the result of stochasticity. As we discuss in Section 3.4.1, subhalos as large as those that host the 1st satellites of Dwarf 1 and Dwarf 2 are fairly rare. It would, however, be useful to compare this result with many more high resolution hydrodynamic simulations.

The satellite stellar mass functions are shown in the middle panel of Figure 3.2. They are intriguingly steep, rising to as many as fifty tiny satellites in the case of Dwarf 1. However, the majority of these star-forming satellites form only a single star particle, and this potentially exciting behavior will need to be confirmed at much higher resolution. In order to make this clear, the dark green shaded region shows the average stellar mass of a single star particle, while the light green shaded region shows the mass range for all other objects that form with $M_\star < 3 \times 10^3$ M$_\odot$ (fewer than 16 star particles). In all six simulations, a total of 187 subhalos form at least one star particle, but a mere six of them form galaxies with $M_\star > 3 \times 10^3$ M$_\odot$ (and only five of these also meet the $N_p^{\rm dm}$ requirement). It is these, the most massive satellites, that will be the focus of our analysis (along with the centrals themselves).

The $M_\star - M_{\rm halo}$ relation for the five resulting "massive satellites" (filled triangles), their less-well-resolved counterparts (open triangles), and all central galaxies (filled circles), is shown in the right panel of Figure 3.2. Plotted are the six central galaxies along with the 1st and 2nd satellites of each host (detailed in Table 1) for each run. Although 18 symbols are shown, we only regard the 11 filled points as reasonably well-resolved. All of the well-resolved systems in this work lie only slightly offset from the extrapolated abundance matching relationship from Garrison-Kimmel et al. [80], which has been constrained down to a stellar mass of $\sim 10^5$ M$_\odot$. This abundance matching relation, obtained by updating the Behroozi et al. [8] relation with a faint-end slope derived from

the measurements of the GAMA survey [5], accurately reproduces the stellar mass functions of the Milky Way and Andromeda satellites, as well as the stellar mass function of the Local Field, when applied to the ELVIS simulations [80].

We do not find the "bending" of the $M_\star - M_{halo}$ relation reported by Sawala et al. [219] at $M_{halo} \simeq 5 \times 10^9$ $M_\odot$. Instead, the relation maintains a fairly steady power-law down to $M_{halo} \simeq 10^9\,M_\odot$. We do see a qualitatively similar break to that seen by Sawala et al. [219] but at a significantly lower halo mass of $M_{halo} \simeq 5 \times 10^8$ $M_\odot$. Below this point it is clear that we are witnessing a large amount of stochasticity, the onset of which corresponds to the scale of extremely faint galaxies ($M_\star \sim 10^3$ $M_\odot$), as opposed to the results of Sawala et al. [219], where stochasticity sets in near the masses of classical dSphs ($M_\star = 10^5$ $M_\odot$). However, it is in this regime where our resolution is severely limited – these galaxies have $\lesssim 15$ star particles. At this time we are unable to determine whether the apparent break and associated stochasticity in our relation at small mass are physical or simply artifacts of resolution, although it is intriguing that the break witnessed by Sawala et al. [219] occurs at the mass of ~ 10 of their baryonic particles as well. Future work at higher resolution will allow us to explore this question more fully.

The most massive satellite of Dwarf 1 represents an interesting statistical rarity (see Section 3.4.1) in that the mass of the subhalo hosting this satellite is just over 40% of the mass of its host, and the satellite itself has $1/3$ of the stellar mass of its central galaxy. Dwarf 1 is clearly undergoing a major merger (see Figure 3.1) and the associated large satellite has properties that are distinct from the other satellites described in this work. Most notably, its stellar mass is two orders of magnitude greater than the other "massive satellites", and it's stellar and dark matter masses are both larger than those of the central hosts of UFD 1 and UFD 2. For identification only (with no relation to the structural properties of the satellite), we refer when necessary to this most massive satellite as "dSph", and all other satellites as "ultra-faint" satellites. The broader term "ultra-faints" is reserved for all galaxies, centrals and satellites, that have $M_\star = 3 - 30 \times 10^3$ $M_\odot$ in our simulations.

3.3.1 Star Formation Histories

The top panel of Figure 3.3 shows the cumulative fractional star formation histories (SFH) for Dwarf 1 (solid line) and its two "massive satellites". The SFH of its large, "dSph" satellite ($M_\star^{z=0} \simeq 2 \times 10^5\,\mathrm{M}_\odot$) is shown by the dotted line. Its second, "ultra-faint" satellite ($M_\star^{z=0} \simeq 5 \times 10^3\,\mathrm{M}_\odot$) is shown by the dashed line. The shaded band corresponds to the epoch of reionization in our simulations. The bottom panel presents similar histories for the three Dwarf 2 runs along with the single most massive "ultra-faint" satellite ($M_\star^{z=0} \simeq 3 - 5 \times 10^3\,\mathrm{M}_\odot$) that forms in each run (dashed lines). In both panels, the short vertical lines at the top mark the first virial crossing of the satellites.

The massive "dSph" satellite of Dwarf 1 demonstrates a particularly interesting SFH. It stops forming stars shortly after the epoch of reionization for almost 8 Gyr (from $z \sim 3$ to $z \sim 0.25$). However, it manages to keep some of its gas on hand in a state that is just below the threshold for star formation. Upon infall into the virial radius of Dwarf 1 at a lookback time of ~ 2 Gyr, followed by pericentric passage ~ 500 Myr later, its ISM is compressed enough to create a new burst of stars, all of which are concentrated at the center of the satellite and were formed in situ. The central galaxy of Dwarf 1 itself also appears to experience a related (albeit mild) burst. This type of bimodal star formation history was suggested by Ricotti [208] as a signature of massive reionization "fossils". Our "dSph" satellite has a slightly higher V_{max} than the range given in that work, and its rebirth of star-formation was triggered by a merger rather than by a change in its halo concentration (as originally suggested by Ricotti 208); it is nevertheless similar in its qualitative nature. Benítez-Llambay et al. [18] tie the star formation history of a set of simulated dwarfs to their virial temperatures when reionization is effectively complete (at $z \simeq 6$). They argue that a bimodal star formation history like that of "dSph" can be created by the merger of a dwarf with a uniformly ancient stellar population (T_{vir} just above a critical value at $z \simeq 6$) and a gas-rich halo that forms all of its stars at late times (T_{vir} just below a critical value at $z \simeq 6$). While this is not the formation mechanism that created "dSph" (our sample does not contain any dwarfs that experience a significant delay *before* forming any stars), when comparing our dwarfs' star formation histories to their

virial temperatures at $z \simeq 6$, our results follow qualitatively similar trends to Benítez-Llambay et al. [18]: objects that have the most intermediate star formation tend to have higher virial temperatures at the completion of reionization than those that have uniformly ancient stellar populations.

In our simulations, halos with $M \simeq 10^{10}\,\mathrm{M}_\odot$ appear to robustly maintain star formation to $z = 0$. This massive satellite at $M_{\mathrm{peak}} \simeq 5 \times 10^9\,\mathrm{M}_\odot$ seems to mark a transition point where reionization begins to favor uniformly ancient star formation. The influence of its impending merger was enough to trigger a rebirth. The "ultra-faint" satellites shown in Figure 3.3 all form in halos smaller than this, with $M_{\mathrm{peak}} \lesssim 2\times10^9\,\mathrm{M}_\odot$. They all form their stars entirely before $z \sim 2$ and are quenched over 5 Gyr before their infall onto the larger hosts, indicating that their star formation is shut down by reionization rather than environmental processes. Importantly, these subsequent mergers do not trigger fresh star formation, as was seen in the more massive satellite. These small halos are either quenched during reionization or shortly thereafter, running out of fuel after the fresh gas supply was shut off by the ambient UV field.

This tendency for our ultra-faint galaxies in $M_{\mathrm{peak}} \lesssim 2\times10^9\,\mathrm{M}_\odot$ halos to quench early is illustrated more clearly in Figure 3.4, where we have plotted the cumulative fractional star formation histories for all seven "ultra-faints" formed in our simulations, e.g. all "ultra-faint" satellites from Figure 3.3 (dashed lines), along with UFD 1 and UFD 2 (solid lines). We also include the unresolved 2nd satellite of Dwarf 2_{Middle} (dotted line) due to it's high stellar mass and to illustrate its similar SFH. From Figure 3.4 it is clear that, in every case, reionization plays a significant role in the shutting down of star formation in our "ultra-faints". Not only were 100% of all stars in all seven of these objects formed before $z = 2$, five of the objects form nearly 90% of their stars before the completion of reionization at $z = 6$.

As can be seen in the lower panel of Figure 3.3, small changes in the feedback implementation and softening length between the three runs in Dwarf 2 cause significant variation in the star formation histories of their central galaxies. One may be concerned then that our expectations for uniformly ancient populations in ultra-faint dwarfs may be affected by small changes of this kind. While the

detailed SFHs of the "ultra-faint" satellites do differ somewhat from run-to-run, these variations are minimal. Perhaps more importantly, the "ultra-faints" in our simulations have uniformly old stellar populations in all runs, irrespective of small changes to the feedback or force softening (and in both satellites and isolated galaxies). The fact that the "ultra-faint" satellite in each of the three runs of Dwarf 2 forms its stars before $z = 2$ is encouraging and suggests that this could be a robust prediction, independent of the subgrid changes.

3.4 Detecting Satellites of Dwarfs

3.4.1 How Common are Satellites of Dwarfs?

It is beyond the scope of this paper to investigate a statistically significant sample of hydrodynamic simulations of $M_{\rm vir} \simeq 10^{10}$ M$_\odot$ dwarfs in order to estimate the frequency with which they will host satellites above a given mass. However, if we assume an $M_\star$ - $M_{\rm peak}$ relation similar to that presented in Figure 2, we can make an estimate using dark-matter-only simulations. We do so using the Exploring the Local Volume in Simulations (ELVIS) suite of collisionless zoom-in simulations of Local Group-like environments [80].

We select all isolated ($d_{\rm halo} > 2\ R_{\rm vir}^{\rm halo}$ for all more massive halos) dwarf-size dark matter halos ($35\ {\rm km\,s^{-1}} < V_{\rm max} < 45\ {\rm km\,s^{-1}}$) in the 12 Local Group-like pairs and the 24 isolated ELVIS simulations, and determine the fraction of those hosts that have N subhalos with $M_{\rm peak} \geq 5 \times 10^8$ M$_\odot$. This is the halo mass that corresponds to $M_\star > 3000\,{\rm M}_\odot$ according to Figure 2.[4] We similarly compute the fraction of dwarf halos that have a very large subhalo with $M_{\rm peak} \geq 4.5 \times 10^9$ M$_\odot$, set by the most massive satellite of Dwarf 1 ($M_\star \gtrsim 2 \times 10^5\,{\rm M}_\odot$).

[4]In all six of our runs, every subhalo with $M_{\rm peak} \geq 5 \times 10^8$ M$_\odot$ forms a well-resolved satellite. Although we focus here on satellites of isolated dwarfs, we note that this criteria would suggest the existence of ~ 100 undetected ultra-faint "stealth galaxies" within 400 kpc of the Milky Way.

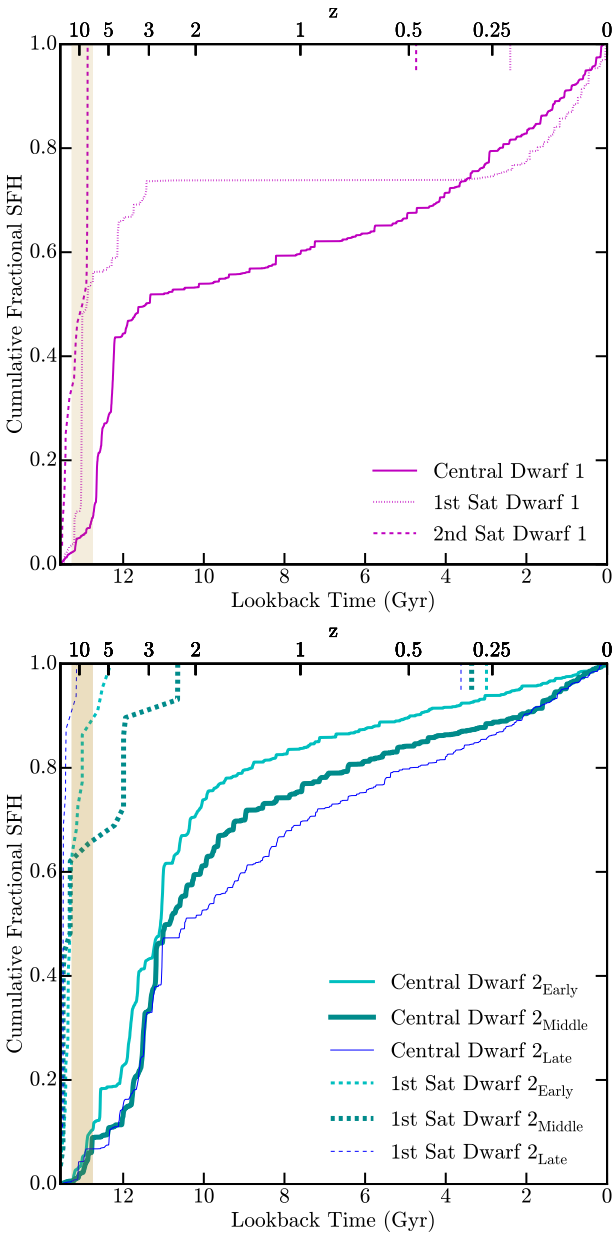

Figure 3.3: Cumulative fractional star formation histories (SFH) of the Centrals (solid) and well-resolved satellites (dashed / dotted) in the two isolated Dwarf simulations ($M_{\rm vir} \sim 10^{10}$ $M_\odot$). Short vertical lines along the top axes indicate infall times of the satellites. Top: Dwarf 1 Central (solid) along with its two satellites. The massive "dSph" satellite is shown by the dotted line and it displays a late-time burst in conjunction with its recent infall. The "ultra-faint" satellite (dashed) is quenched early, during reionization (shaded band), well before it is accreted. Bottom: Dwarf 2 centrals (solid) and the most massive satellites (dashed) in each run. All three "ultra-faint" satellites in the Dwarf 2 runs form all of their stars before $z = 2$.

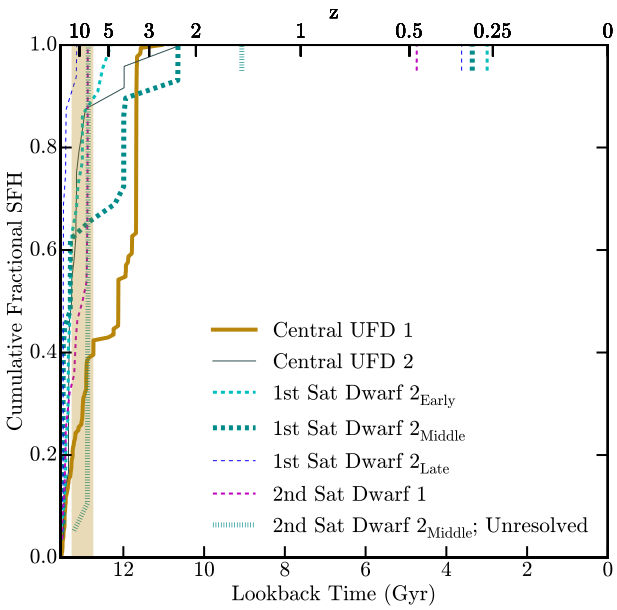

Figure 3.4: Ancient "ultra-faints". Shown are the cumulative fractional star formation histories (SFH) for our isolated (solid) and resolved satellite (dashed) "ultra-faint" dwarfs ($M_\star^{z=0} = 3 - 30 \times 10^3\,\mathrm{M}_\odot$). The SFH of the unresolved outlier that passes the stellar mass cut (see Section 3.2.1 for details) is also shown (dotted line). All seven of these systems have ancient stellar populations, similar to those observed for the ultra-faint galaxies of the Milky Way.

Figure 3.5 shows the probability for an isolated dwarf halo in ELVIS to have ≥ N satellites of at least these two peak virial masses within a projected distance of 50 kpc (the typical virial radius for our dwarfs) as a function of N. According to Figure 3.5, isolated halos with $M_{\rm vir} \sim 10^{10}$ $\mathrm{M}_\odot$ will have one or more subhalos that could host $M_\star \gtrsim 3000\,\mathrm{M}_\odot$ satellites about 35% of the time. The likelihood that an isolated dwarf in the same mass range hosts a satellite as massive "dSph", however, is just under 5%.

Using both SDSS and the semi-analytic models of Guo et al. [91] applied to the MS-II simulation [35], Sales et al. [215] show that the probability for a central galaxy to host a satellite a given fraction of its stellar mass, $M_\star^{\rm sat}/M_\star^{\rm cen}$, decreases as a strong function of $M_\star^{\rm cen}$ until $M_\star^{\rm cen} = 10^{10}$ $\mathrm{M}_\odot$, becoming independent of $M_\star^{\rm cen}$ for centrals below the stellar mass of the Milky Way. Although the stellar masses of the central galaxies in our simulations lie far below their stellar mass range ($10^{7.5} \leq M_\star/\mathrm{M}_\odot \leq 10^{11}$), this decoupling of the probability from $M_\star^{\rm cen}$ for satellites of dwarf galaxies allows us to make a comparison with the probabilities they find. Their Figure 2 suggests

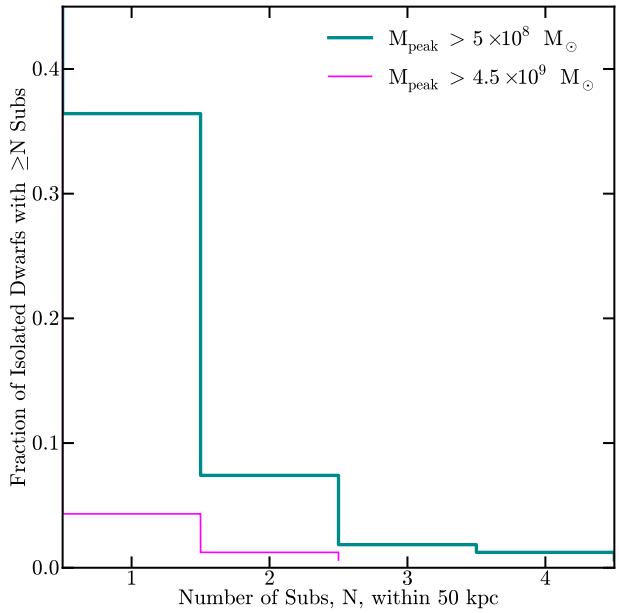

Figure 3.5: From the dark-matter only ELVIS suite of Local Group simulations, the fraction of isolated dwarfs in the V_{max} range $35-45$ km s^{-1} with N or more subhalos with $M_{peak} > 5\times10^8$ $M_\odot$ (thick line) and 4.5×10^9 $M_\odot$ (thin line) that are found within 50 kpc of their host galaxy. In all of our hydrodynamic runs, all subhalos with $M_{peak} > 5 \times 10^8$ $M_\odot$ have formed a galaxy with $M_\star > 3 \times 10^3$ $M_\odot$, while the most massive satellite, "dSph", forms in a subhalo with $M_{peak} \simeq 4.5 \times 10^9$ $M_\odot$. According to these dark-matter only simulations, $\sim 35\%$ of isolated dwarfs should have a "massive satellite" within their virial radii, but only $\leq 5\%$ should host a satellite as massive as "dSph".

that for all central galaxies with $M_\star^{cen} \leq 10^{10}$ $M_\odot$, there is a $\sim 40\% - 50\%$ chance that they host a satellite with stellar mass $M_\star^{sat}/M_\star^{cen} \sim 0.5\%$ – similar to our "ultra-faints". This is roughly consistent with the $\sim 35\%$ probability we find. They also find that the likelihood for a satellite as massive in proportion to its central as "dSph" ($M_\star^{sat}/M_\star^{cen} \sim 1/3$), is vanishingly small. Again, according to their Figure 2 and assuming that the lack of dependence of this probability on $M_\star^{cen}$ for dwarfs, there is only about a $1-2\%$ chance for a central to have such a massive satellite, which is again roughly consistent with the results shown in Figure 3.5.

3.4.2 Can they be detected?

Our ultra-faint galaxies with $M_\star \simeq 3 - 30 \times 10^3$ $M_\odot$ all reside within low mass halos ($M_{\rm vir} < 3 \times 10^9$ $M_\odot$). They also have extremely diffuse stellar distributions, as expected for the ultra-faint, low dark-matter mass, "stealth galaxies" discussed in B10. Figure 3.6 shows the projected (2D) half stellar-mass radii, $R_{1/2}$, of our simulated galaxies vs their total stellar mass. The central galaxies are shown as colored circles and the satellites as triangles (the single unresolved satellite with $M_\star > 3 \times 10^3$ $M_\odot$ is shown as an open triangle). The open black circles show observed Milky Way dwarfs [173]. The black points with error bars are the half-mass radii and stellar masses of the eight recently reported ultra-faint satellite candidates from The DES Collaboration et al. [241], and the single blue square with error bars is Hydra II from Martin et al. [162].

In addition to stellar mass, we checked the sizes of the simulated galaxies to make sure they are also well-resolved. While the plotted half-light radii are clearly much larger than our minimum force softening, a more demanding criterion is the Power et al. [203] radius which, for the dissipationless version of these runs, is $\gtrsim$ 100 pc (see Oñorbe et al. 188). While this suggests that we are dynamically well resolved, the effect on the baryonic component within this radius is harder to determine. In lower resolution runs, the satellites' half-mass radii do vary by about a factor of two, but in both directions (some are larger, some smaller). Higher resolution simulations would be particularly useful for solidifying the expectations for the sizes of these galaxies. While predicting these quantities is difficult, we believe it is worth exploring because of the implications for the observability of these objects.

The surface brightness detection limit for SDSS is shown as a solid black line in the Figure. It represents a constant peak central surface brightness for a Plummer profile

$$\Sigma_{\rm peak} = \frac{L}{\pi R_{1/2}^2} 0.036 \; L_\odot {\rm pc}^{-2} \tag{3.1}$$

and corresponds to a surface brightness of $\mu_{\rm V} = 30$ mag arcsec^{-2} for solar absolute magnitude

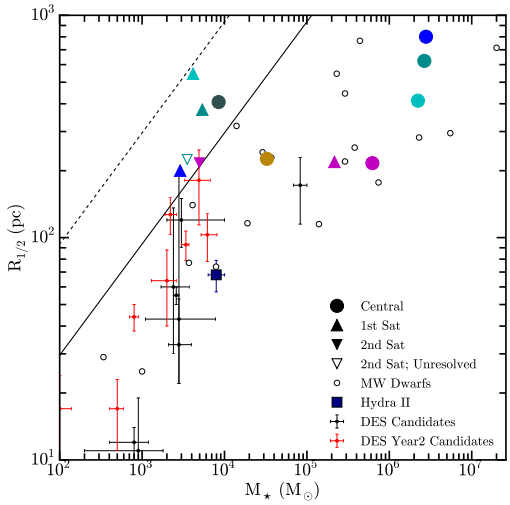

Figure 3.6: 2D half-stellar-mass radii, $R_{1/2}$, vs $M_\star$ for all resolved galaxies in our simulations (filled circles and triangles; colors are the same as in Figure 3.2), the one unresolved satellite with $M_\star > 3000$ $M_\odot$ (open triangle), as well as for observed Milky Way dwarfs [173, open circles], the newly discovered DES ultra-faint dwarf candidates [241, black points with error-bars], [63, red points with error-bars], and Hydra II [162, blue square]. The solid line represents a surface brightness limit of 30 mag arcsec^{-2} while the dashed line shows 32.5 mag arcsec^{-2}. Both lines and the Hydra II data point assume a stellar mass-to-light ratio of 1. Satellites as massive as "dSph", which occur around $\sim 5\%$ of isolated dwarfs (see Figure 3.5), should be currently visible, but most of the satellites lie just out of reach, and will visible only with future surveys such as LSST or potentially even DES.

$M_{\odot,V} = 4.83$ and assuming a stellar mass-to-light ratio of $M_\star/L = 1(M_\odot/L_\odot)$.

Except for UFD 1, all of our simulated "ultra-faint" dwarfs have surface brightnesses fainter than 30 mag arcsec^{-2}, and would qualify as "stealth galaxies". The dashed line in Figure 3.6 shows a surface brightness of 32.5 mag arcsec^{-2}, a limit that will likely be achieved by upcoming surveys such as the Large Synoptic Survey Telescope (LSST). Once the full co-added LSST data is collected, satellites this faint should be able to be detected out to ~ 1 Mpc over half the sky [245].

In the more immediate future, the Dark Energy Survey (DES) is already online. DES will only be able to detect ultra-faint objects of this kind out to about 400 kpc, and is only slated to cover $\sim 12\%$ of the sky over its first 5 years. However, DES contains within its footprint the dwarf galaxy Phoenix. Phoenix has a stellar mass of $M_\star = 7.7 \times 10^5$ $M_\odot$ and is about 415 kpc away. It is falling into the Milky Way with a velocity of ~ -100 km s^{-1} [173] and is likely on first approach,

meaning that it is a good analog to the isolated systems simulated in this work. This suggests that Phoenix may be an excellent dwarf galaxy candidate to host an ultra-faint satellite detectable in the immediate future. It also has an advantage over more distant dwarfs like Cetus or Aquarius in that it is close enough that low luminosity satellites such as the "ultra-faints" predicted in this work have a greater chance of being visible.

Although, according to Figure 3.5, there is only a $\sim 35\%$ chance that Phoenix will host a subhalo massive enough to form a $\sim 3000\,\mathrm{M}_\odot$ satellite, once the volume that lies between us and Phoenix has been factored in, we find that the probability for finding an ultrafaint in its field increases to anywhere between $50\% - 65\%$ according to the ELVIS simulations and depending on the specifics of abundance matching for $M_\star \sim 3000\,\mathrm{M}_\odot$ satellites. In general, for future telescopes that have a limited number of pointings available, targeting the ~ 50 kpc region around isolated dwarf galaxies should prove to be a much more efficient strategy than pointing into blank sky, as it should increase the chances of observing an ultra-faint satellite by $\sim 35\%$. These expectations are in broad agreement with the work of Sales et al. [214], who discussed dwarf companions associated with the LMC.

3.5 Comparison to Previous work

Sawala et al. [220] run a series of 12 zoom-in simulations of Local Group-like environments at three levels of resolution, both with baryons and with dark matter only. They run each simulation with and without a cosmic UV background that turns on sharply at $z = 11.5$, and argue that the onset of the ionizing background radiation sets the mass scale at which all halos become dark. Their simulations shut down star formation in over 80% of halos with present-day virial masses less than 10^9 $\mathrm{M}_\odot$. Their Figure 2 does seem to show convergence in their highest resolution simulation run with reionization, but the gas particle mass in their highest resolution run ($\sim 10^4$ $\mathrm{M}_\odot$) is an order of magnitude higher than the total stellar mass of most of the the satellites that form in our

simulations, indicating that they would fail to detect these galaxies. Furthermore, their reionization turns on at a higher redshift than does ours ($z = 10.65$), which may lead to a higher halo mass cutoff for star formation. Order of magnitude changes in the final count of simulated dwarf satellites can be caused by varying the timing of reionization for a simulated Milky Way from $z \sim 6$ to $z \sim 11$ [41]. Likewise, Simpson et al. [227] show that changing the onset of the cosmic reionizing background from $z = 8.9$ to $z = 7$ can change the stellar mass of a simulated dwarf galaxy from $M_\star \sim 10^5$ $M_\odot$ to $M_\star \sim 10^6$ $M_\odot$.

Shen et al. [222] run a zoom-in simulation of a small group of seven dwarf galaxies with a range of virial masses (4×10^8 $M_\odot \leq M_{\rm vir} \leq 4 \times 10^{10}$ $M_\odot$). They find that galaxies only form in the halos with present day $M_{\rm vir} > 10^9$ $M_\odot$, and of the halos that form galaxies, the two with $M_{\rm vir} < 10^{10}$ $M_\odot$ only form stars long after the end of reionization. Although they do not model H_2 cooling nor self-shielding in their simulations, they do approximate the effects of H_2 cooling and run a parallel simulation without a cosmic UV background. In their reionization-free simulation, all dwarfs form stars, but they show that the gas in the three low mass halos never reaches the column density required for self shielding. Their baryonic particle mass is $\sim 10^3$ $M_\odot$, the same particle mass we achieve in the low resolution runs of Dwarf 2 (see Oñorbe et al. 188 for details). In our low resolution runs, each of the most massive subhalos forms an object with stellar mass similar to its high resolution counterpart, but at this resolution each satellite object consists of only $3 - 5$ star particles. While it is difficult to say conclusively that resolution is the main driver of their apparent halo mass limit for star formation, in general it has been the case that every time resolution is increased in simulations, the minimum virial mass for a halo that can form stars has approached lower values [95, 188]. In addition to enabling the formation of galaxies with $M_\star$ lower than the low resolution baryonic particle mass, higher resolution simulations allow for a more accurate description of shielding, which will also affect the minimum halo mass that can form stars. Furthermore, resolving the formation of dense substructures that collapse under self-gravity and become self-shielding requires resolving the Jeans/Toomre mass of the galaxies, which can be as low as ~ 1000 $M_\odot$ (and corresponds to a required force/gravitational softening of at least

$< 10 - 100$ pc) in baryon-poor dwarfs.

Our simulations do not escape the challenges of imperfect resolution, but because our particle mass is an order of magnitude lower than most simulations that attempt to form galaxies in low mass halos, we can push down the predicted low mass limit for the halos that can form ultra-faint satellites. Rather than attempt to make a prediction for the low*est* mass halo that can form a galaxy, we predict that ultra-faint dwarf galaxies *can* form in dark matter subhalos as low mass as $M_{\rm peak} \sim 5\times10^8$ M$_\odot$. While we cannot state with certainty that these galaxies are fully converged in our high resolution runs, the stellar masses of the satellites do show a better convergence between low and high resolution runs than do the centrals. (see Oñorbe et al. 188 for a discussion of the convergence of the centrals). Additionally, at these low masses, we still see sensitivity to spatial resolution and feedback (e.g. the second satellite of Dwarf $2_{\rm Middle}$). More and higher resolution runs of dwarfs with $M_{\rm vir} \sim 10^8 - 10^{10}$ M$_\odot$ that vary feedback prescriptions, reionization onset and spectrum, and particle mass are needed to fully probe the low mass end of the simulated stellar mass function and the $M_\star - M_{\rm halo}$ relation.

3.6 Discussion and Conclusions

In the ΛCDM paradigm, all dark matter halos, from those around giant galaxy clusters to those hosting ultra-faint galaxies, should be filled with subhalos. We have used ultra-high resolution ($m_p^{\rm gas} \approx 255$ M$_\odot$) simulations with the PSPH version of `Gizmo` [97] and the Feedback in Realistic Environments (FIRE) prescriptions [98] to predict that subhalos of isolated dwarf halos should form galaxies.

Most of the subhalos around dwarf galaxies are expected to be of low-mass ($M_{\rm peak} \lesssim 10^9$ M$_\odot$) and we predict that some should host ultra-faint galaxies with $M_\star \lesssim 10^4$ M$_\odot$. If these tiny satellites are observed, it would provide evidence that dark matter substructure persists to very small scales,

as predicted in the standard paradigm.

Using the dark-matter-only simulations of the ELVIS suite, we show that each isolated field dwarf ($M_\star \sim 10^6$ M$_\odot$) galaxy in the Local Group has about a 35% chance of hosting at least one satellite with $M_\star > 3000\,\mathrm{M}_\odot$. The extended ~ 50 kpc regions around known field dwarfs in the Local Group should prove to be fruitful search areas for ultra-faint satellites, as each pointing towards a dwarf also contains all of the volume of the Milky Way dark matter halo along the line of sight to that region. The Phoenix dwarf galaxy in particular is an excellent target due to its proximity to the Milky Way and the high probability that it is on first infall.

Although we consider only isolated dwarfs in this work, it is worth noting that some satellites of the Milky Way may also have their own satellites. [54] show, using the ELVIS simulations, that approximately 7% of Milky Way satellites (but as many as 25% depending on the infall time and mass of the group), fell in as a part of LMC-size groups, and that several of the recent DES satellites are likely satellites of the LMC (see also Sales et al. [214]). A simple calculation of the Roche limit for a rigid satellite assuming the common halo mass scale for Milky Way dwarf spheroidals ($M_{\rm halo} = 3 \times 10^9$ M$_\odot$) orbiting a Milky Way-size host ($M_{\rm vir} = 10^{12}$ M$_\odot$) shows that Fornax could potentially hold on to ultra-faint satellites residing within its inner 17 kpc, and Sculptor out to 10 kpc, assuming the more massive satellite is on first infall. This suggests that these galaxies might also be suitable candidates to host "satellites of satellites".

We do not see a sharp cut-off or break in the $M_\star - M_{\rm halo}$ relation, at least for $M_{\rm peak} > 5 \times 10^8$ M$_\odot$. We do, however, see a sharp cut-off in halos that host galaxies with uniformly ancient stellar populations. The "ultra-faint" dwarfs in our simulations form most of their stars in the first billion years after the Big Bang and are subsequently deprived of the cold gas required for star formation due to the ionizing background radiation, and not by infall into a more massive dark matter halo. We predict that below a critical mass threshold ($M_{\rm halo} \sim 5\times10^9$ M$_\odot$, $M_\star \sim 3\times10^4$ M$_\odot$) all galaxies are ubiquitously ancient and, unlike more massive galaxies ($10^7 < M_\star/\,\mathrm{M}_\odot < 10^9$) that are nearly uniformly star forming in the field [82], both central and satellite ultra-faint galaxies should all be

quenched.

For satellites with $M_\star > 10^5$ $M_\odot$, it is likely that time since infall is one of the primary factors in quenching their star formation. Massive satellites ($10^{8.5} < M_\star / M_\odot < 10^{9.5}$) have been shown to have extremely long quenching timescales, probably due to the cutting off of the fresh gas supply after infall [52, 273, 276]. Slightly less massive galaxies ($10^6 < M_\star / M_\odot < 10^8$) are likely quenched over much shorter timescales by the tidal or ram-pressure forces they experience upon falling in as satellites [230, 75, 274]. However, it is likely that the quenching of ultra-faints is completely independent of their infall time, and set by the timing of the onset of and the mass they had at reionization, although these results will need to be confirmed at higher resolution.

The precise stellar masses of the "ultra-faint" dwarfs in our simulations are likely also sensitive to the reionization redshift (with an earlier onset of reionization likely to quench star formation in higher mass halos) and may also be sensitive to star formation physics at very low metallicities. We plan to explore these dependencies in future work, but here we point out that it is possible to form ultra-faint satellites of regular dwarf galaxies and highlight that they are quenched by reionization rather than infall.

The recent discovery of up to nine Milky Way dwarf satellite galaxy candidates in the Southern Sky by DES [241, 140] has important consequences for our understanding of star formation in low mass galaxies. Of particular interest is DES J0344.3-4331 (Eridanus II), because of its large distance from the Milky Way (> 330 kpc) [241]. At this distance, whether the satellite is on first infall or even headed out after a pericentric passage, it was likely accreted within the last ~ 2 Gyr. Given that the initial age estimate for Eridanus II shows that it likely has an ancient stellar population [~ 10 Gyr; 241][5], this would mean that it was quenched long before infall. If confirmed in follow-up observations, Eridanus II would be the first known ultra-faint galaxy shown to be quenched in the field, supporting our findings that, below a critical mass scale $\sim 5 \times 10^9\,M_\odot$, all galaxies host

[5] Koposov et al. [140] suggest that Eridanus II could possibly have a population of young stars in addition to the old stellar population.

ancient stellar populations quenched by reionization-related feedback, and not by environmental processes. This would be a clear example of a reionization "fossil", as first discussed by Ricotti & Gnedin [209].

Chapter 4

The No Spin Zone: Rotation vs Dispersion Support in Simulated and Observed Dwarf Galaxies

4.1 Introduction

Dwarf spheroidal (dSph) galaxies comprise the largest population of galaxies in the Local Group, consisting of nearly 60 confirmed members [130, 182, 160, 225, 226, 224, 1, 14, 43, 84, 137, 259, 261, 110, 46, 48, 142, 140, 141, 281, 243, 47, 126, 129, 128, 247, 146, 147, 124, 123, 161, 162]. These objects are characterized by their low luminosities, spheroidal shapes, high mass-to-light ratios, and by the absence of appreciable gas or recent star formation [71, 254, 167, 50, 284, 174]. Line of sight velocity measurements suggest that dSphs have little to no rotation in their stellar populations and velocity dispersion profiles that are nearly flat with radius [278, 184, 183, 262, 263, 136, 135, 166].

In the Local Group, dSphs tend to occupy regions close to either the Milky Way or M31 [167, 87].

At greater distances from the two massive galaxies, the population of dSphs dwindles and gives way to a different class of low-mass galaxies called dwarf irregulars (dIrrs). These galaxies have similar luminosities to dSphs, but are distinct most notably in that they have retained some of their gas. Many dIrrs also demonstrate disky features and rotation in their HI content [167, 174]. This "Local Group morphology-density relation," with dSphs found close and dIrrs found far from MW and M31, mimics similar relationships between galaxy shape and distance from the local barycenter found in clusters [190, 62]. This, and the fact that both dSphs and dIrrs can be fit with exponential light profiles [167, 71, 66], is often used to argue in favor of a dwarf irregular transformation-based origin for dSphs [66, 171]. If, as is commonly understood from classical galaxy formation theory, all galaxies initially form as thin, angular momentum supported disks [277, 67, 27], then significant transformation must occur to convert these rotationally-supported galaxies into the puffy, dispersion-dominated dSphs we see today.

The currently-favored mechanism for bringing about this transformation is known as "tidal stirring" [170, 171]. According to this model, rotationally-supported dwarfs with exponential stellar disks and high gas fractions are repeatedly tidally shocked at the pericenters of their orbits. While ram pressure is primarily responsible for removing gas from the dwarf, it is the repeated tidal shocks that produce the morphological transformation. In general, for low-mass dwarfs (the majority of those found in the Local Group), this involves the creation of a tidally-induced bar, which transports high angular momentum material to the outer regions of the galaxy where it is subsequently stripped. This reduces the rotation of the system and transforms the galaxy into a spheroidal, dispersion-supported system [168, and references therein]. In the tidal stirring model, a galaxy is generally considered to have been transformed into a dSph if it has no (or very little) gas, an ellipticity within a specific range (usually $0.1 < e < 0.5$; greater values of ellipticity indicate a more elongated shape), and if the ratio of its line-of-sight rotational velocity to its velocity dispersion, $v_{\rm rot}/\sigma$, is below some value – usually 1, but as low as 0.5. A number of early simulations investigating this effect had considered infalling dIrr models with extremely cold disks

($v_{\rm rot}/\sigma \simeq 5$) but more recent simulations involve somewhat hotter initial disks [1] $v_{\rm rot}/\sigma \simeq 3$ [e.g. 117].

While tidal stirring simulations have been successful at producing systems with $v_{\rm rot}/\sigma \lesssim 1$ [170, 171, 172, 131, 168, 155, 117, 118, 156, 250], historically it has been difficult to reduce $v_{\rm rot}/\sigma$ to values < 0.5 found for many observed dwarf satellites [165]. The most complete transformations occur for highly eccentric orbits [170, 171], at low inclination, and that are mildly prograde [117, 156, but see Mayer et al. 172]. The high eccentricity in particular allows for shorter orbital times and repeated pericenter passages (typically $3-5$, but as many as 8). Short orbital times ($1-3$ Gyr) and close pericenter distances ($10-70$ kpc) have been shown to be particularly important to the transformation [117]. Interestingly, these simulations have often found that the accreted dIrr galaxies need to orbit within a Milky Way host potential for ~ 10 Gyr in order to be able to complete the required number of pericenter passages [131, 168, 155, 117, 118, 156, 250].

One major issue with any scenario that requires ~ 10 Gyr in order to transform a dIrr to a dSph is that this is quite long compared to the expected accretion times for satellites derived from cosmological simulations of Milky Way and Local Group analogues. Specifically, the overwhelming majority of Milky Way satellites are predicted to have fallen in less than 10 Gyr ago [210, 80, 75, 271], with $\sim 40\%$ accreted within the last 4 Gyr. Only 2 of the 11 classical Milky Way dwarf satellites are dIrrs [which appear to have fallen in very recently, 21], and they are significantly more massive than the dSph satellites. This suggests that any environmental transformation associated with dSph formation needs to occur within ~ 2 Gyr of accretion [75, 271]. Furthermore, at least two dSphs, Cetus and Tucana, currently exist at large distances from either the Milky Way or Andromeda [681 and 882 kpc from the closest giant, 174]. They, like the dSphs much closer to their hosts, have little to no gas and their stars are dispersion rather than rotationally-supported (see below). Explaining the existence of such distant objects as the result of tidal stirring poses a particularly

[1] Kazantzidis, Łokas & Mayer [118] suggest that if dark matter halos are more core-like, then it would be natural to consider $v_{\rm rot}/\sigma \simeq 1-1.5$ as starting points because $v_{\rm rot}$ is reduced at small radii while σ might be expected to stay fixed.

difficult challenge to the model. Due to this difficulty, Kazantzidis et al. [117] predict that distant dSphs should have systematically higher values of $v_{\rm rot}/\sigma$. Alternatively, it has been shown that dwarfs with highly cored dark-matter profiles undergo faster transformations [after just $1-2$ pericenter passages, 118, 250]. This reduction in required time spent near the host would be particularly useful in explaining the lack of rotation in an object like Leo I, which has undergone only a single pericenter passage at a distance of ~ 100 kpc from the Milky Way [232, 34].

There are other alternative mechanisms for transforming a dIrr into a dSph that require the initial galaxy to interact with another object. Dwarf-dwarf mergers can create dSphs [179, 119], and the mechanism is satisfyingly similar to models proposed for transforming massive disks into giant ellipticals [104]. Starkenburg, Helmi & Sales [236] propose that the spheroidal shapes of dSphs can be reproduced by mergers between dwarf galaxies and lower-mass dark halos, but do not discuss rotation support. Another model, "resonant stripping", posits that a fly-by between a dwarf and a galaxy 100 times its mass can instigate resonances in the smaller dwarf that preferentially strip the stellar material [60]. Interactions between dwarfs in the Local Group are common [53], but merger-based transformation scenarios fail to explain the "Local Group morphology-density relation," and so are not likely to account for a large fraction of observed dSphs.

Given the strict requirements for the tidal stirring mechanism to be effective, it seems reasonable to question the initial conditions used for dwarf galaxies in these models. The traditional picture of disk galaxy formation was developed for massive galaxies [67, 27] with virial temperatures $T_{\rm v} \sim 10^6\ K$, which is well above the expected bulk ISM temperature of a cooled gas in a galaxy $T_{\rm g} \sim 10^4$ K. In this case, the pressure support radius of cooled gas will be tiny compared to the angular-momentum support radius. [2] It is in this sense that the disk of a massive galaxy is expected to be "cold." However, Kaufmann, Wheeler & Bullock [115, hereafter KWB] show, using a simple analytic approximation and hydrodynamic simulations, that low-mass galaxies with shallow po-

[2]The radius of pressure support declines exponentially as the ratio $T_{\rm g}/T_{\rm v}$ shrinks, where $T_{\rm g}$ is a phenomenological proxy that mimics the net effect of velocity dispersion from various feedback effects, such as inefficient cooling, heating by an internal or external ultraviolet (UV) background, supernova feedback, turbulent pressure, or cosmic-ray heating, among others [115].

tential wells and modest virial temperatures ($T_{\rm v} \lesssim 10\ T_{\rm g}$) will tend to have pressure support radii that are comparable to their angular-momentum support radii. KWB did not look at $v_{\rm rot}/\sigma$ explicitly, but showed that at low virial mass ($M_{\rm vir} \lesssim 10^{11}\,{\rm M}_{\odot}$), the dispersion-supported component of a galaxy should begin to rival the rotationally-supported component [see also e.g. 49]. As first suggested by Read, Pontzen & Viel [207], the above arguments only strengthen if one considers additional ISM pressure imparted on small galaxies from internal feedback effects and turbulent motions. Moreover, stars, unlike gas, can never re-cool after their orbits are disturbed by potential fluctuations or mergers. Taken together, these arguments suggest that the stellar populations of dwarf galaxies residing in the field are not necessarily expected to exhibit well-ordered, disk-like motions as seen in their larger cousins.

Recently, large samples of stellar kinematic data for local dIrr galaxies have become available [225, 77, 149, 150, 127]. These data enable more detailed studies of the pressure support in field dwarfs. In particular, Kirby et al. [127] present a stellar kinematic analysis of seven (non-satellite) dwarf galaxies in the local volume, and showed that only one among them (Pegasus) demonstrates a clear sign of rotation in its stellar population. While they did not explicitly rule out rotation in the other objects, the work of Kirby et al. provides some suggestion that a high degree of rotation support is not the rule among isolated dwarfs.

In what follows, we conduct a systematic search for stellar rotation in Local Group dwarfs. We use a Bayesian analysis on a large observational sample of dwarfs consisting of twenty eight MW and M31 dSphs, two dwarf ellipticals (dEs), and ten dwarfs beyond the virial radii of either the MW or M31 (including two isolated dSphs and eight dIrrs) to estimate $v_{\rm rot}/\sigma$. We confirm previous findings that both the MW and M31 dSphs, with few exceptions, have stellar populations that are not rotating. We show further that isolated dwarfs in the Local Group are also largely dispersion-supported, with only two of ten showing strong Bayesian evidence for rotation, and seven of ten failing to show even moderate evidence in favor of rotation. We propose an alternative formation scenario for dSphs galaxies: most dwarf galaxies form initially as puffy, dispersion-supported or

slowly rotating systems, and gas removal via ram pressure stripping (enabled by internal feedback) is likely the main process that leads to the formation of dSphs. We demonstrate the feasibility of this in a ΛCDM scenario by using the same Bayesian analysis to measure the rotation support in four hydrodynamic cosmological zoom-in simulations of *isolated* dwarf galaxies run with FIRE/GIZMO. The star particles in our simulated isolated dwarf galaxies are dispersion-supported, without any interaction with a more massive galaxy, and their ellipticities are also similar to the known dSph population without the need for harassment.

In Section 4.2, we highlight our observational sample. Our simulated dwarfs and their characteristics are described in Section 4.3. Section 4.4.1 is used to explain the Bayesian analysis we perform on each galaxy. The results of our systematic search for stellar rotation are given in Section 4.5. We discuss these findings in Section 4.6 and conclude in Section 4.7.

4.2 Observations

We analyze spectroscopic data for 40 Local Group galaxies, which are listed by name in Table 4.1 (column 1) along with the number of stars used in our analysis (column 10). We use measured line-of-sight velocities for each star as well as the associated errors kindly provided by the authors in the references listed below.

Among Milky Way satellites, our sample includes all nine of the classical dwarfs: Carina, Fornax, Sculptor, Sextans [259], Draco [264], Leo I [166], Leo II [135], Sagittarius [78], and Ursa Minor [193]. For the ultra-faint dSphs of the Milky Way we examine Canes Venatici I, Canes Venatici II, Coma Berenices, Hercules, Leo IV, Ursa Major I, Ursa Major II [225], and Boötes I [142].

For the M31 system we examine 14 satellites: And II [94], And I, And III, And V, And VII, And IX, And X, And XIII, And XIV, And XV, [243], And VI, [47] Cassiopeia 3, and Lacerta 1 [159], NGC 147, and NGC 185 [83].

Finally, we study ten isolated Local Group galaxies: Tucana [77], Leo T [225], NGC 6822, IC 1613, VV 124, Pegasus dIrr, Leo A, Cetus and Aquarius [127], and WLM [149, 150]. The dwarf galaxies Phoenix [105] and Antlia [249] have spectroscopic samples that are too small to search for rotation.

The authors of these spectroscopic studies have taken care to remove foreground contamination. We adopt those same selection criteria here. All samples are homogeneous except for WLM, which consists of data from two distinct observations (one with Keck and the other with the VLT). The analysis includes all stars in each sample, and the samples span varying degrees of spatial extent within the galaxy (the majority go out to $\sim$ 1.5 effective radii). All stars analyzed are either red giant or horizontal branch stars.

A subset of our analysis includes an allowance for proper motion (see below). This effect is only important for the satellites of the Milky Way. We specifically use proper motion measurements from *Hubble Space Telescope* (HST) observations when available. In the standard frame (μ_α, μ_δ) and in units of mas century^{-1}, these are: Carina [$22 \pm 9, 15 \pm 9$; 202], Draco [$17.7 \pm 6.3, -22.1 \pm 6.3$; 205], Fornax [$47.6 \pm -4.6, -36.0 \pm 4.1$; 201], Leo I [$11.40 \pm 2.95, -12.56 \pm 2.93$; 232], Leo II [$10.4 \pm 11.3, -3.3 \pm 15.1$; 152], Sagittarius [$-254 \pm 18, -119 \pm 16$; 164], Sculptor [$9 \pm 13, 2 \pm 13$; 200], and Ursa Minor [$-50 \pm 17, 22 \pm 16$; 199].

4.3 Simulations

Our simulations were previously presented in Wheeler et al. [275], and consist of four[3] cosmological zoom-in simulations of isolated dwarf galaxy halos. Two were run at the mass of the halos

[3]In Wheeler et al. [275], we also analyzed two additional simulations that used the same initial conditions as one of our $\sim 10^{10}$ $M_\odot$ halos, but were run with slight changes to the subgrid feedback implementation (see Wheeler et al. 275 for details). We have not included analysis of those two runs in the text or in the figures here, but note that they have values of $v_{\rm rot}/\sigma$ and ellipticity similar to the other runs analyzed here, and so would not change our results if included.

Dwarf	Category	$M_\star (10^6\,M_\odot)$	$d_{L_\star}$ (kpc)	ellipticity	v_{rot}/σ	v_{rot} (km s^{-1})	σ (km s^{-1})	N	ln B_{rad}	ln B_{rot}
Coma Berenecis	UF dSph	0.0037	45	$0.38^{+0.14}_{-0.14}$	$1.78^{+1.07}_{-0.92}$	$7.01^{+3.16}_{-3.24}$	$4.00^{+0.95}_{-0.87}$	59	3.13	0.73
Ursa Major II	UF dSph	0.0041	38	$0.63^{+0.05}_{-0.05}$	$0.81^{+1.07}_{-1.41}$	$5.33^{+6.04}_{-9.27}$	$6.46^{+1.88}_{-1.43}$	20	1.57	−0.17
Canis Venatici II	UF dSph	0.0079	161	$0.52^{+0.11}_{-0.11}$	$1.35^{+0.67}_{-0.57}$	$5.21^{+1.83}_{-1.91}$	$3.88^{+1.19}_{-0.96}$	25	4.21	1.64
Ursa Major I	UF dSph	0.014	102	$0.80^{+0.04}_{-0.04}$	$0.15^{+0.41}_{-0.41}$	$1.20^{+3.25}_{-3.23}$	$7.93^{+1.25}_{-1.01}$	39	1.05	−1.73
Bootes I	UF dSph	0.029	64	$0.39^{+0.06}_{-0.06}$	$0.28^{+0.28}_{-0.25}$	$1.44^{+1.42}_{-1.30}$	$5.16^{+0.55}_{-0.48}$	74	1.19	−2.00
Hercules	UF dSph	0.037	126	$0.68^{+0.08}_{-0.08}$	$0.20^{+0.59}_{-0.69}$	$1.10^{+3.25}_{-3.76}$	$5.49^{+1.11}_{-0.92}$	30	1.38	−1.76
Canis Venatici I	UF dSph	0.23	218	$0.39^{+0.03}_{-0.03}$	$0.04^{+0.18}_{-0.21}$	$0.29^{+1.38}_{-1.61}$	$7.67^{+0.49}_{-0.45}$	214	1.38	−2.48
Draco	MW dSph	0.29	76	$0.31^{+0.02}_{-0.02}$	$0.29^{+0.10}_{-0.10}$	$2.62^{+0.90}_{-0.86}$	$9.05^{+0.31}_{-0.28}$	476	2.68	1.99
Ursa Minor	MW dSph	0.29	78	$0.56^{+0.05}_{-0.05}$	$0.27^{+0.16}_{-0.15}$	$2.16^{+1.27}_{-1.18}$	$7.97^{+0.24}_{-0.23}$	867	2.11	−0.59
Carina	MW dSph	0.38	107	$0.33^{+0.05}_{-0.05}$	$0.00^{+0.09}_{-0.09}$	$0.03^{+0.56}_{-0.56}$	$6.44^{+0.22}_{-0.21}$	758	1.84	−2.60
Sextans	MW dSph	0.44	89	$0.35^{+0.05}_{-0.05}$	$0.08^{+0.12}_{-0.11}$	$0.54^{+0.82}_{-0.80}$	$7.10^{+0.30}_{-0.27}$	424	1.82	−2.30
Leo II	MW dSph	0.74	236	$0.13^{+0.05}_{-0.05}$	$0.13^{+0.18}_{-0.19}$	$0.86^{+1.24}_{-1.29}$	$6.76^{+0.49}_{-0.44}$	164	1.26	−2.17
Sculptor	MW dSph	2.3	86	$0.32^{+0.03}_{-0.03}$	$0.16^{+0.12}_{-0.10}$	$1.37^{+1.03}_{-0.84}$	$8.79^{+0.18}_{-0.18}$	1349	3.35	−0.72
Sagittarius*	MW dSph	3.5	18	$0.65^{+0.01}_{-0.01}$	$0.28^{+0.89}_{-1.33}$	$2.11^{+6.78}_{-10.33}$	$7.68^{+1.48}_{-1.13}$	180	10.83	80.26
Leo I	MW dSph	5.5	258	$0.21^{+0.03}_{-0.03}$	$0.16^{+0.12}_{-0.12}$	$1.44^{+1.12}_{-1.09}$	$8.99^{+0.40}_{-0.37}$	327	2.16	−1.37
Fornax	MW dSph	20	149	$0.30^{+0.01}_{-0.01}$	$0.03^{+0.05}_{-0.07}$	$0.30^{+0.57}_{-0.70}$	$10.59^{+0.17}_{-0.16}$	2409	1.47	−2.76
Andromeda XIV	M31 dSph	0.02	162	$0.20^{+0.11}_{-0.11}$	$0.24^{+0.40}_{-0.43}$	$1.42^{+2.42}_{-2.61}$	$6.10^{+1.08}_{-0.91}$	48	1.20	−1.34
Andromeda X	M31 dSph	0.096	110	$0.30^{+0.18}_{-0.18}$	$0.39^{+0.50}_{-0.50}$	$2.85^{+3.57}_{-3.66}$	$7.37^{+1.73}_{-1.32}$	21	1.35	−0.99
Andromeda IX	M31 dSph	0.15	40	$0.12^{+0.07}_{-0.07}$	$0.10^{+0.47}_{-0.43}$	$1.22^{+5.70}_{-5.21}$	$12.08^{+2.56}_{-2.05}$	32	1.16	−1.06
Andromeda V	M31 dSph	0.39	110	$0.28^{+0.07}_{-0.07}$	$0.28^{+0.32}_{-0.31}$	$3.08^{+3.52}_{-3.39}$	$11.02^{+1.28}_{-1.08}$	85	1.87	−0.70
Andromeda XV	M31 dSph	0.49	174	$0.24^{+0.10}_{-0.10}$	$0.42^{+0.57}_{-0.63}$	$2.08^{+2.87}_{-2.56}$	$4.92^{+1.67}_{-1.34}$	29	1.65	−1.04
Andromeda III	M31 dSph	0.83	75	$0.59^{+0.03}_{-0.03}$	$0.60^{+0.57}_{-0.58}$	$5.87^{+5.57}_{-5.45}$	$9.74^{+1.58}_{-1.24}$	62	0.35	−0.35
Andromeda VI	M31 dSph	2.8	269	$0.41^{+0.03}_{-0.03}$	$0.04^{+0.55}_{-0.54}$	$0.54^{+7.36}_{-7.19}$	$13.29^{+2.75}_{-2.11}$	38	1.10	−0.78
Andromeda I	M31 dSph	3.9	58	$0.29^{+0.03}_{-0.03}$	$0.48^{+0.68}_{-0.57}$	$5.31^{+7.60}_{-6.50}$	$11.17^{+2.36}_{-1.82}$	51	0.94	−0.31
Cassiopeia III	M31 dSph	3.98	144	$0.50^{+0.09}_{-0.09}$	$0.25^{+0.24}_{-0.37}$	$2.04^{+2.00}_{-3.01}$	$8.30^{+0.54}_{-0.50}$	212	1.88	−1.48
Lacerta I	M31 dSph	6.3	275	$0.43^{+0.07}_{-0.07}$	$0.13^{+0.24}_{-0.28}$	$1.36^{+2.51}_{-2.91}$	$10.30^{+0.83}_{-0.74}$	127	1.32	−1.65
Andromeda II	M31 dSph	7.6	184	$0.14^{+0.02}_{-0.02}$	$1.43^{+0.18}_{-0.17}$	$11.43^{+1.31}_{-1.33}$	$7.97^{+0.38}_{-0.37}$	474	6.80	70.13
Andromeda VII	M31 dSph	9.5	218	$0.13^{+0.04}_{-0.04}$	$0.47^{+0.21}_{-0.20}$	$6.11^{+2.65}_{-2.59}$	$12.95^{+1.05}_{-0.97}$	135	2.01	1.25
NGC 147	dE/dSph	62	142	$0.46^{+0.02}_{-0.02}$	$0.96^{+0.11}_{-0.11}$	$17.05^{+1.81}_{-1.91}$	$17.73^{+0.63}_{-0.58}$	520	11.42	77.56
NGC 185	dE/dSph	187	442	$0.22^{+0.01}_{-0.01}$	$0.45^{+0.12}_{-0.11}$	$10.62^{+2.87}_{-2.48}$	$23.73^{+0.84}_{-0.80}$	442	4.13	12.99
Leo T	Iso dIrr/dSph	0.14	422	$0.29^{+0.12}_{-0.14}$	$0.08^{+1.01}_{-0.87}$	$0.66^{+8.20}_{-7.13}$	$8.17^{+2.08}_{-1.61}$	19	1.80	−0.64
Tucana	Iso dSph	0.56	882	$0.48^{+0.03}_{-0.03}$	$0.22^{+0.44}_{-0.39}$	$4.79^{+8.99}_{-8.64}$	$21.37^{+4.56}_{-3.34}$	19	0.71	−0.25
Aquarius †	Iso dIrr/dSph	1.6	1066	$0.50^{+0.10}_{-0.10}$	$1.70^{+1.23}_{-1.01}$	$10.47^{+5.68}_{-5.66}$	$6.24^{+1.63}_{-1.35}$	43	−1.00	0.62
Cetus	Iso dSph	2.6	681	$0.33^{+0.06}_{-0.06}$	$0.02^{+0.34}_{-0.57}$	$0.15^{+2.75}_{-4.65}$	$8.24^{+0.84}_{-0.75}$	120	1.73	−1.46
Leo A	Iso dIrr	6.0	803	$0.40^{+0.03}_{-0.03}$	$1.99^{+0.99}_{-1.09}$	$10.93^{+5.17}_{-4.85}$	$5.46^{+1.11}_{-0.92}$	50	0.29	1.50
Pegasus	Iso dIrr	6.61	474	$0.46^{+0.02}_{-0.02}$	$1.43^{+0.25}_{-0.22}$	$16.25^{+2.56}_{-2.24}$	$11.36^{+0.92}_{-0.80}$	105	0.19	29.09
VV 124	Iso dIrr/dSph	8.3	1367	$0.44^{+0.04}_{-0.04}$	$0.56^{+1.00}_{-0.57}$	$5.22^{+8.98}_{-5.25}$	$9.27^{+1.08}_{-0.93}$	87	1.40	−0.47
WLM	Iso dIrr	43	836	$0.65^{+0.01}_{-0.01}$	$1.01^{+0.17}_{-0.15}$	$14.79^{+2.32}_{-2.04}$	$14.69^{+0.90}_{-0.81}$	180	10.83	21.36
IC 1613	Iso dIrr	100	517	$0.24^{+0.06}_{-0.06}$	$0.48^{+0.39}_{-0.63}$	$4.99^{+3.96}_{-6.57}$	$10.44^{+0.79}_{-0.71}$	143	3.89	1.46
NGC 6822 †	Iso dIrr	100	452	$0.24^{+0.05}_{-0.05}$	$0.41^{+0.12}_{-0.15}$	$9.38^{+2.77}_{-3.46}$	$22.62^{+0.99}_{-0.92}$	314	−0.26	3.30

Table 4.1: Properties and estimated parameters of all galaxies in the observed sample. (1) Name of galaxy. (2) Galaxy type. (3) Galaxy stellar mass from literature. (4) Distance from galaxy to its nearest massive neighbor from literature – either the Milky Way or M31. (5) Ellipticity of galaxy obtained from literature, with error. (6) Median of parameter v_{rot}/σ from Bayesian analysis, with $\pm1\,\sigma$ error. (7) Median rotational velocity from Bayesian analysis, with $\pm1\,\sigma$ error. (8) Median velocity dispersion from Bayesian analysis, with $\pm1\,\sigma$ error. (9) Number of stars used in analysis. (10) ln B_{rad}, where B is the Bayes factor for the rotation model. Values less than 3 imply weak/inconclusive evidence for the radially varying model and negative values favor the flat

believed to host classical dwarf galaxies ($M_{\rm vir} \simeq 10^{10}\,{\rm M}_\odot$) and two at lower mass ($M_{\rm vir} \simeq 10^{9}\,{\rm M}_\odot$) (see Wheeler et al. 275 for details). All of our simulations were run with the fully conservative cosmological hydrodynamic code Gizmo [98] in 'PSPH-mode', with the standard FIRE feedback implementation. Every run uses a gas particle mass of $m_p^{\rm gas} = 255\ {\rm M}_\odot$ except for UFD 2, which uses $m_p^{\rm gas} = 499\ {\rm M}_\odot$. The gas force resolution varies from $\epsilon_{\rm gas}^{\rm min} = 1.0 - 2.8$ pc, and the stellar masses of the resultant galaxies span $\sim 10^{3.9} - 10^{6.3}\,{\rm M}_\odot$.

All of these cosmological simulations are of isolated dwarfs, that is, with no large neighbors in either the high or low resolution regions. All but one of the ($M_{\rm vir} \simeq 10^{9}\,{\rm M}_\odot$) dwarfs were selected from 5 h^{-1} Mpc boxes to have typical values of spin parameter λ, concentration, and formation time for their mass range, and also to have small Lagrangian volumes [189]. The lowest mass ($M_{\rm vir} \simeq 10^{9}\,{\rm M}_\odot$) dwarf was selected from a 25 h^{-1} Mpc box and required to have no other halos of 50% or more of its mass within 4 $R_{\rm vir}$ at $z = 0$ and a small Lagrangian volume. All analysis was performed on the $z = 0$ snapshot of each simulation.

4.4 Measuring Rotation

4.4.1 Bayesian Analysis

For each galaxy, we investigate models with and without rotation in order to determine if there is evidence in favor of rotation. We do not assume the stellar components necessarily exist within coherently rotating disks – the rotation we measure is based entirely on the observed gradient in velocity across the face of the galaxy in the sky. We assume that the likelihood of observing a

distribution $\mathcal{D} = (\mathbf{v}, \epsilon)$ of N stars with line-of-sight velocities v_j and associated errors ϵ_j is:

$$\mathscr{L} = \prod_{j=1}^{N} \frac{1}{\sqrt{2\pi(\sigma^2 + \epsilon_j^2)}} \exp\left[-\frac{1}{2}\frac{(v_j - v_j^{\rm rel})^2}{\sigma^2 + \epsilon_j^2}\right], \tag{4.1}$$

where σ is the underlying (constant) velocity dispersion and $v_j^{\rm rel}$ is a relative velocity, the form of which depends on whether the model is rotating or non-rotating. In the absence of rotation, the relative velocity is simply the average bulk motion of the system $v_j^{\rm rel} = \overline{v}$. With rotation, the relative velocity becomes

$$v_j^{\rm rel} = \overline{v} + v_{\rm rot}\cos(\theta - \theta_j), \tag{4.2}$$

where θ is a model parameter (measured from North to East) that defines the axis of rotation, θ_j is the position angle for each star, and $v_{\rm rot}$ is the observed rotation across this axis. We explore two models for $v_{\rm rot}$: constant rotation, $v_{\rm rot}(R) = v_o$ and a radially varying pseudo-isothermal sphere, $v_{\rm rot} = v_o\sqrt{1 - {\rm R_o}/{\rm R}\arctan({\rm R}/{\rm R_o})}$, where R is the distance from the rotation axis on the plane of the sky, and v_o and R_o are the rotation velocity and rotation radial scale parameters respectively. We choose to measure the rotation at the radius that encloses 90% of the spectroscopic sample. This is because the value of the rotation at infinity is poorly constrained. We have checked that this radius encloses over 70% of the total mass in each galaxy for over half of the sample (and over 60% of the total mass for $\gtrsim$ 60% of the sample). Using the radius that encloses 75% or 95% does not significantly change the results presented here.

Note that if the galaxy's angular momentum vector is inclined relative to us with an angle i, then $v_{\rm rot} = v_{\rm rot}^{\rm intrinsic}\sin i$, where $v_{\rm rot}^{\rm intrinsic}$ is the magnitude of the intrinsic rotation. In what follows we quote results for $v_{\rm rot}$ (rather than $v_{\rm rot}^{\rm intrinsic}$) because $\sin i$ is poorly constrained for the stars. The value of $v_{\rm rot}$ is a lower limit on the intrinsic value of $v_{\rm rot}^{\rm intrinsic}$. We discuss the possible effects of inclination

in Section 4.5.1.

For nearby dwarfs, the line-of-sight velocities as measured from Earth will not project along parallel directions. One implication is that if a galaxy is moving in the transverse direction, a significant component of this proper motion can be observed as a gradient in the line-of-sight motions of stars across the face of the galaxy [70, 257]. This perspective proper motion effect can be important for interpreting the dynamics of local galaxies [111, 260] and we therefore include it when possible here. All classical dSphs except Sextans have proper motion measurements from Hubble Space Telescope (HST) observations. For these galaxies, we include the perspective proper motion effects on the relative velocity as $v_{\rm rel} \rightarrow v_{\rm rel} + v_{\rm perspec}$, marginalizing over the proper motion using Gaussian priors centered on the reported measurements (see below). We do not include the (currently unmeasured) proper motion parameters in Sextans or any of the Ultra Faint dSphs. The isolated and the M31 systems are too distant for proper motions to have a measurable effect.

The posterior distribution, $\mathcal{P}(\mathscr{M}|\mathcal{D}, H)$, is the distribution of model parameters $\mathscr{M}$ given the observation of data $\mathcal{D}$. The symbol H represents the model under consideration: we consider both rotating and non-rotating scenarios. The likelihood, $\mathscr{L} = \mathcal{P}(\mathcal{D}|\mathscr{M}, H)$, is the probability to observe the data given a set of model parameters. The posterior is related to the likelihood via Bayes' Theorem:

$$\mathcal{P}(\mathscr{M}|\mathcal{D}, H) = \frac{\mathcal{P}(\mathcal{D}|\mathscr{M}, H) Pr(\mathscr{M})}{\mathcal{P}(\mathcal{D}, H)}, \tag{4.3}$$

where $Pr(\mathscr{M})$ is the prior distribution, set by our preconceived knowledge of the model. In our fiducial case that explores rotation and allows for proper motion, we have model parameters $\mathscr{M} = (\overline{v}, \sigma, v_o, \theta, R_o, \mu_\alpha, \mu_\delta)$, where μ_α and μ_δ are the proper motions.

The denominator in Equation 3, $Z = \mathcal{P}(\mathcal{D}, H)$, is referred to as the Bayesian evidence. It is a

normalization factor that is commonly ignored, but will be used for model comparison in our analysis. To test whether the radially varying rotation model is favored over the flat rotation model, we compute the natural log of the Bayes factor, which is defined as the ratio of the evidence for each model: $\ln B_{\rm rad} = \ln(Z_{\rm rot,rad}/Z_{\rm rot,flat})$. A value greater than zero favors the radially varying model. Then, for the preferred model, we compute the natural log of the Bayes factor for the rotating model compared to a model with no rotation: $\ln B_{\rm rot} = \ln(Z_{\rm rotating}/Z_{\rm non-rotating})$. A value greater than zero here favors the rotating model. The significance of the preference for each model (radially varying vs flat; rotating vs non-rotating) is based on the magnitude of $\ln B_{\rm rad}$ ($\ln B_{\rm rot}$) on Jeffery's scale: (0-1), (1-3), (3-5), (5+), corresponds to inconclusive, weak, moderate, and strong evidence in favor of the radially varying (rotating) model. Likewise, the corresponding negative values offer varying degrees of evidence in favor of the flat (non-rotating) model. $\ln B_{\rm rad}$ and $\ln B_{\rm rot}$ for each galaxy in this work can be found in columns 10 and 11 of Table 4.1. For all other parameters estimated by our model, we list the parameter corresponding to the preferred model (flat vs radially varying). Note that only two galaxies (Aquarius and NGC 6822) prefer the flat rotation model.

We compute the posterior distribution with a Multi-Nested Sampling routine [72, 73]. This method directly calculates the evidence and, as a by-product, samples the posterior distribution (for a review of Bayesian method and model comparison see Trotta 251). We marginalize over the prior ranges: $-20 < \overline{v} - v_{\rm g} < +20$ km s^{-1}, $0 < \sigma < +75$ km s^{-1}, $-50 < v_o < +50$ km s^{-1}, $0 < \theta < +\pi$, $-300 < \mu_\alpha - \bar{\mu}_{\alpha,\rm HST} < +300$ mas century^{-1}, and $-300 < \mu_\delta - \bar{\mu}_{\delta,\rm HST} < +300$ mas century^{-1}, where $v_{\rm g}$, $\bar{\mu}_{\alpha,\rm HST}$, and $\bar{\mu}_{\delta,\rm HST}$ are the values for each galaxy taken from the literature. For the radially varying model, $-1 < \log_{10}(R_o/\rm kpc) < \log_{10}\left(1.5 \times R_{\rm spectra\,max}\right)$. For several galaxies, we examine larger ranges of $\overline{v}$, μ_α, and μ_α. This is significant only for Sagittarius, where its close position causes its best fit HST proper motions to be well outside the range considered for other dwarfs. For galaxies with rotation axes near 0 or π, we marginalize over $-\pi/2 < \theta < +\pi/2$. All priors are uniform except μ_α and μ_δ, which are Gaussian and centered on the HST measurements. We test our method with mock data sets and verify that the input parameters are recovered.

Properties taken from the literature and parameter estimates for each observed galaxy in our analysis, given observational dataset $D(\mathrm{v_j}, \epsilon_\mathrm{j}, \theta_\mathrm{j})$ for each star, can be found in Table 4.1. Before moving on to our broad results (Section 5) we will first comment on several galaxies of particular interest in comparison to past work in the literature.

4.4.2 Comments on Individual Galaxies

Draco: Two recent proper motion measurements for Draco differ by several standard deviations: $(17.7 \pm 6.3, -22.1 \pm 6.3)$ [205] and $(-28.4 \pm 4.7, -28.9 \pm 4.1)$ [44]. Casetti-Dinescu & Girard [44] discuss possible reasons for the discrepancy, but are unable to determine one. We run our analysis with both measurements, which lead to v_rot/σ values of $2.62^{+0.86}_{0.90}$, and $v_\mathrm{rot}/\sigma = 2.03^{+0.91}_{-0.97}$ respectively. The two measurements of v_rot/σ are within one sigma of one another and have roughly the same kinematic position angle (101° versus 105°). We use the HST measurement to be consistent with the reminder of the classical dSph.

Sagittarius: Peñarrubia et al. [195] predict significant rotation in this galaxy based on simulations aimed at reproducing the Sagittarius stream. However, they assumed its progenitor was a late-type disk galaxy ($v_\mathrm{rot} \approx 20\ \mathrm{km\,s^{-1}}$). Follow-up work by Peñarrubia et al. [196] did not detect rotation of this magnitude and could only reproduce the line-of-sight velocities observed today using progenitor models with no or little rotation. Similar searches for rotation in Sagittarius have made no conclusive detection [103, 78].

Our result show very strong evidence for some rotation ($v_\mathrm{rot}/\sigma \simeq 0.28^{+0.89}_{-1.33}$; $\ln B_\mathrm{rot} = 80.26$) but this determination is complicated by the large field of view occupied by Sagittarius on the sky. There are three different proper motion measurements [59, 204, 164]. All three are discrepant and were obtained from analyzing different fields within Sagittarius. It is possible that the discrepancy is due to the 3D perspective motion or the internal motions of stars within the galaxy. In our analysis, we use the transform of the three measurements into the center of mass frame computed by Massari

et al. [164]: -301 ± 11, -145 ± 11 mas century^{-1}.

The kinematic axis preferred in our analysis is $\theta = -64 \pm 6°$, which is offset from the photometric major axis of $\theta = 102 \pm 2°$ [174]. A velocity gradient along the major axis is expected based on the 3D motion of Sagittarius [196, 78]. It is peculiar, then, that our model favors attributing part of the gradient to rotation instead of the perspective motion. Part of the signal could be induced by tidal interactions, but a more in-depth analysis of the Sagittarius system is required to make a strong conclusion. Another origin of this problem could be the fact that Sagittarius may suffer from a higher degree of foreground contamination from Milky Way stars. We distrust our $v_{\rm rot}/\sigma$ analysis for these reasons, and exclude Sagittarius from all figures. However, we note that our estimated value suggests that Sagittarius is not rotationally-supported, and it would lie in the same general region as most of the dSphs analyzed in this work.

And II: Ho et al. [94] detect $v_{\rm rot} = 8.6 \pm 1.6$ km s^{-1} along the minor axis and a maximum $v_{\rm rot} = 10.9 \pm 2.4$ km s^{-1} located at $\theta = 113 \pm 9°$ [the photometric position angle is $\theta = 46 \pm 6°$, 94]. Our kinematic axis is offset from this value: $v_{\rm rot}/\sigma = 1.43^{+0.18}_{-0.17}$; $v_{\rm rot} = 11.43^{+1.31}_{-1.33}$ km s^{-1}; $\theta = -26 \pm 4°$. We detect stellar rotation at strong significance near the minor axis, which could have been caused by a minor merger [4].

Tucana: Fraternali et al. [77] suggest that a flat rotation curve with $v_{\rm rot} \approx 15$ km s^{-1} along the major axis is consistent with their data [$\theta = 97°$, 218]. Our analysis finds no evidence for rotation and prefers a value consistent with zero: $v_{\rm rot}/\sigma = 0.22^{+0.44}_{-0.39}$; $v_{\rm rot} = 4.79^{+8.99}_{-8.64}$ km s^{-1}; $\ln B_{\rm rot} = -0.25$. The position angle is quite unconstrained: $\theta = -6^{+59}_{-49}$. If Tucana is rotating, a larger sample size will be required to uncover it.

Aquarius: This galaxy has one of the largest preferred $v_{\rm rot}/\sigma$ values in our sample ($\simeq 1.70^{+1.23}_{-1.01}$), though the error is large and the Bayesian evidence is weak ($\ln B_{\rm rot} = 0.62$). As with Leo A, a larger sample size will be required to make a stronger statement about the rotation and to confirm that it is indeed rotationally-supported. The kinematic axis of the HI gas is at $\theta \approx 70°$ [7]. Our

kinematic axis is misaligned at $\theta \approx -1^\circ$. The magnitude of the stellar rotation is similar to the observed gas rotation.

Leo A: Although our model prefers a fair amount of rotation in this galaxy ($v_{\rm rot}/\sigma = 1.99^{+0.99}_{-1.09}$), our analysis yields only weak evidence for rotation in Leo A compared to a non-rotating model ($\ln B_{\rm rot} = 1.50$). There is no rotation seen in HI gas [285]. Our potential rotation at $\theta \approx 33^\circ$ is almost perpendicular to the HI disc at $\theta = 102^\circ$. A larger kinematic sample size will be required to make a stronger statement about the rotation.

Pegasus: Stellar rotation in Pegasus was first measured in Kirby et al. [127] with a magnitude of $\sim 10\ {\rm km\,s^{-1}}$ across the major axis [located at a position angle of 122°, 99]. We measure a larger value that is 20° offset from the major axis: $v_{\rm rot} = 16.25^{+2.56}_{-2.24}$, $\theta = 146^{+16}_{-20}$. A velocity gradient is observed in HI across the major axis. It has been suggested that this gradient could be the result of random motions [286], but since the stellar rotation is detected at such high significance ($\ln B_{\rm rot} = 29.09$), it seems likely that the gas is rotating as well. This is in general agreement with the conclusions of Kirby et al. [127].

WLM: We measure: $v_{\rm rot} = 14 \pm 1.6\ {\rm km\,s^{-1}}$, $\sigma = 15.6 \pm 0.9\ {\rm km\,s^{-1}}$, and $\theta = 163^{23}_{-19}$. The position angle we prefer agrees well with the value of $\theta = 173^\circ$ reported by Leaman et al. [150]. In addition, Leaman et al. [150] measure a velocity dispersion for WLM that is broadly consistent with our value ($\sigma \approx 15\ {\rm km\,s^{-1}}$), and they report a stellar rotation and $v_{\rm rot}/\sigma$ that are also consistent with our measured values ($v_{\rm rot} \sim 15\ {\rm km\,s^{-1}}$; $v_{\rm rot}/\sigma = 1.01^{+0.17}_{-0.15}$ with strong evidence).

IC 1613: Rotation support in IC 1613 is quite unconstrained in our model, $v_{\rm rot}/\sigma = 0.48^{+0.39}_{-0.63}$. Our measured rotation is roughly half as large as that suggested by its HI kinematics [191]. IC 1613 is currently undergoing substantial star formation [288, 100] and has HI bubbles and shells [157, 223]. The lack of clear rotation support may be due to this starburst phase [206].

NGC 6822: We find moderate evidence for stellar rotation in RGB stars in this galaxy ($\ln B_{\rm rot} = 3.30$) but the rotation is sub-dominant to the velocity dispersion with $v_{\rm rot}/\sigma = 0.41^{+0.12}_{-0.15}$. The

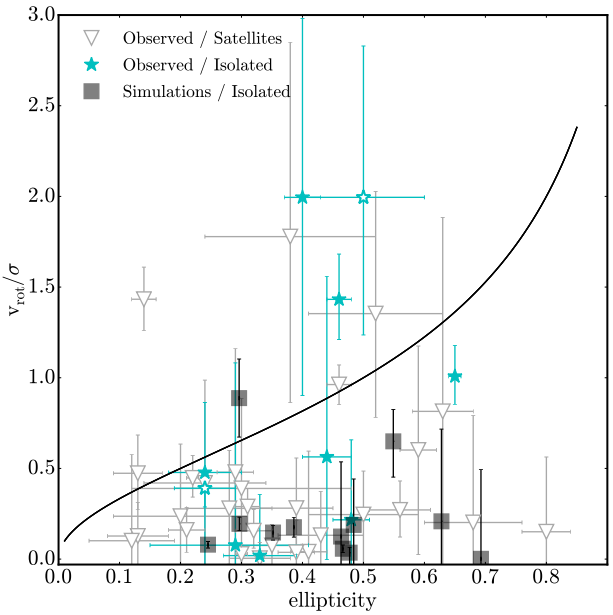

Figure 4.1: Stellar rotation support $v_{\rm rot}/\sigma$ vs. e (ellipticity) for observed satellites of the Milky Way and M31 (open gray triangles), isolated Local Group Dwarfs (cyan stars), and simulated isolated (dIrr) galaxies (gray squares). Open stars show the two galaxies for which a flat rotation model is preferred. The solid line shows the approximate value of $v_{\rm rot}/\sigma$ for self-gravitating objects that are flattened by rotation [24]. The (5/30) observed satellite galaxies (open triangles) that lie above the curve are Andromeda VII, Andromeda II, Coma Berenecis NGC 147, and Canis Venatici II. Only three isolated observed galaxies lie above the curve. Those are Leo A, Pegasus, and Aquarius.

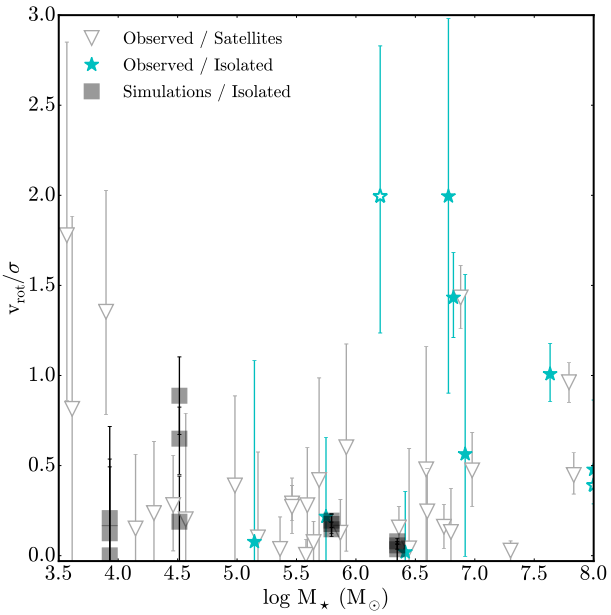

Figure 4.2: Stellar rotation support ($v_{\rm rot}/\sigma$) vs. stellar mass for observed satellites of the Milky Way and M31 (open gray triangles), isolated Local Group Dwarfs (cyan stars), and our simulations (gray squares). No clear trend with stellar mass is seen in the data, although there could be a slight upward turn at the highest masses observed.

rotation axis is offset from the photometric position angle [located at $\theta = 65°,\ 6]$ by $\approx 40°$: $v_{\rm rot} = 9.38^{+2.77}_{-3.46}$ km s^{-1}, $\theta = 108^{+9}_{-11}$, $\sigma = 22.62^{+0.99}_{-0.92}$. Stellar rotation in Carbon stars was previously detected along the major axis [56]. As the HI disk is perpendicular to the stellar component, they label NGC 6822 as a polar ring galaxy. N-type Carbon stars have variable velocity, limiting the precision of the Demers, Battinelli & Kunkel [56] measurements to ± 15 km s^{-1}. In addition, their sample was created from two telescopes, with a velocity offset of 46 km s^{-1} between each measurement and $\Delta\bar{v} \approx 20$ between the RGB stars and C stars. With these caveats, it is intriguing that the different tracers all have a different kinematic axes, possibly hinting at past mergers. Valenzuela et al. [253] model NGC 6822 using a tilted ring analysis and show that the presence of a bar can artificially decrease the rotation signal for some projections. We do not account for bars in our model, instead opting to use the same analysis for each galaxy in our sample.

4.4.3 Simulation analysis

We apply an identical method for calculating $v_{\rm rot}/\sigma$ to the simulations (see Section 4.4.1). To calculate the ellipticity values for the simulations, we use a simple method outlined in Cappellari et al. [42] for converting two dimensional field data to a single $v_{\rm rot}/\sigma$ value. For each of the three orthogonal distributions, the galaxy is rotated along the axis parallel to the line-of-sight until there is a maximum in the difference between velocity measurements in the left and right hemispheres of the projection plane. Then, after binning the stars in two dimensions, we sum up the effective "flux" in each bin and weight the bins by their distance from the center of the simulated galaxy, according to this formula:

$$(1-e)^2 = \frac{\sum_{n=1}^{N} F_n y_n}{\sum_{n=1}^{N} F_n x_n}, \tag{4.4}$$

where x_n and y_n are the bin centers and we replace flux, F_n, with the number of star particles in that bin. [4] All analysis on the simulations is done on all star particles within 3 kpc of the center of each simulated galaxy. This choice allow us to select all stars that belong to the main galaxy while excluding any satellites.

4.5 Results

Figure 4.1 shows $v_{\rm rot}/\sigma$ vs. e (ellipticity) for all objects in our study. $v_{\rm rot}/\sigma$ is a standard diagnostic for detecting rotational support in more massive systems [17] as well. Observed Milky Way and M31 satellites are shown as open triangles, observed isolated dwarfs are shown as cyan stars, and simulated (isolated) galaxies are gray rectangles. The black line shows the expectation for self-gravitating objects flattened by rotation [24]. For the sake of concreteness, we consider objects that lie above this line to be at least marginally rotationally-supported. The galaxy ellipticity values were drawn from the literature.

Of all the galaxies in our sample, eight have $v_{\rm rot}/\sigma$ values that are consistent with being supported by rotation, rather than dispersion: Coma Berenecis, Canis Venatici II, Andromeda II, Andromeda VII, NGC 147, Aquarius, Leo A and Pegasus. Of these, only And II (dSph), NGC 147 and Pegasus (dIrr) show rotation at strong significance. The Bayesian evidence that Aquarius and Leo A are rotating is inconclusive or weak – the small sample sizes prohibit a stronger statement. We also detect sub-dominant rotation at strong significance in NGC 185, Sagittarius, and WLM. We detect some (sub-dominant) rotation in NGC 6822, but at a lower significance.

Perhaps the most striking feature of Figure 4.1 is the distribution of isolated galaxies. 7/10 of the isolated dwarfs in our analysis have $v_{\rm rot}/\sigma$ vs ellipticity values that are consistent with being

[4] We have tested that this method produces ellipticity values consistent with those obtained by performing a 2D Gaussian fit to histograms of the "flux" (in this case the number of star particles) in a 2×2 grid along the line-of-sight to each object.

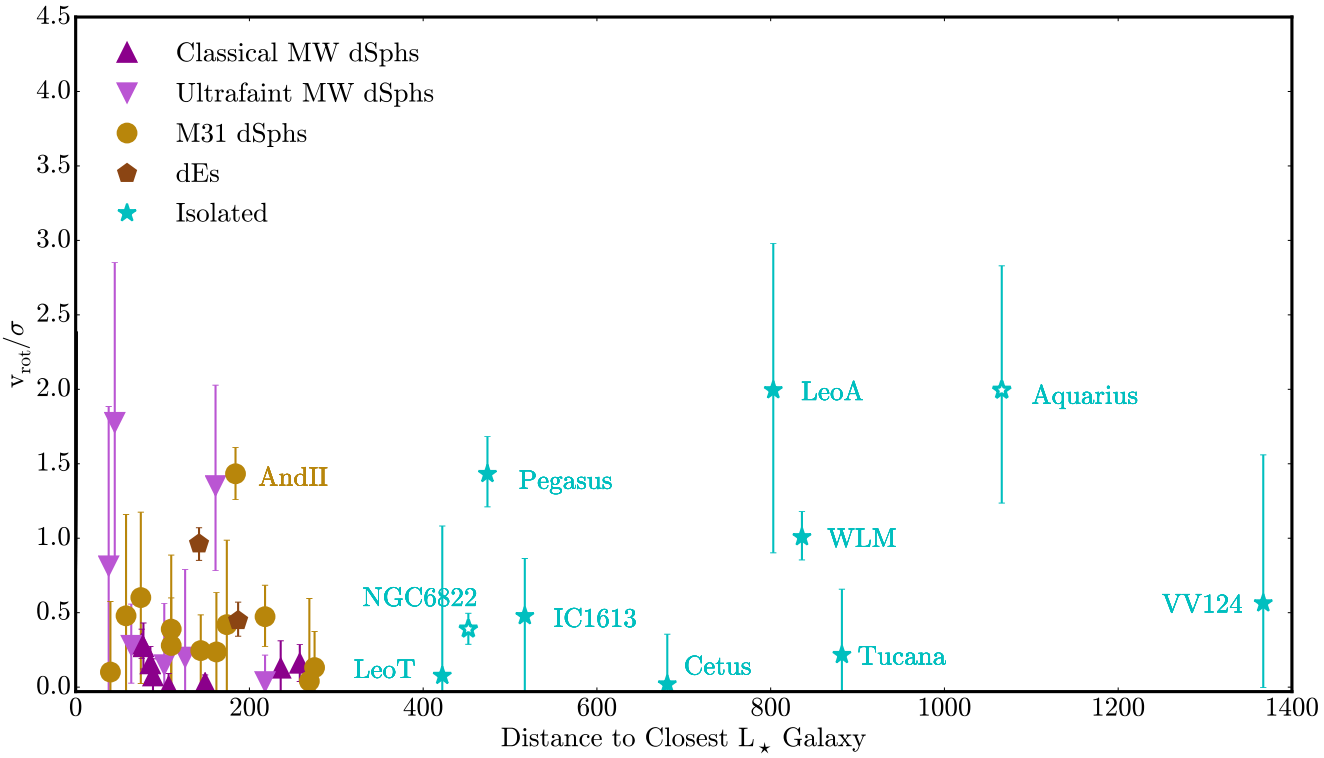

Figure 4.3: Rotation support $v_{\rm rot}/\sigma$ vs $d_{L_\star}$, distance from the dwarf to the closest $L_\star$ galaxy (either the Milky Way or M31), for observed classical Milky Way dSphs (up-facing dark magenta triangles), ultra-faint dSphs (down-facing light magenta triangles), M31 dSphs (gold circles), isolated Local Group Dwarfs (cyan stars) and dEs (brown pentagons). There is no clear trend between $v_{\rm rot}/\sigma$ and $d_{L_\star}$, as predicted by tidal stirring models.

dispersion-dominated, while (6/10) have $v_{\rm rot}/\sigma \lesssim 1.0$. All have $v_{\rm rot}/\sigma \lesssim 2.0$ This is in stark contrast to the common assumption that dIrrs have stellar disks that are smaller versions of their more massive, rotating counterparts. Even the three rotation-dominated systems are only modestly so, with $v_{\rm rot}/\sigma \simeq 1.5 - 2$, which is significantly less rotation than a canonical cold disk, and below the values typically assumed as initial conditions for tidal stirring scenarios for dSph formation ($v_{\rm rot}/\sigma \gtrsim 3$) [117].

Our simulated dwarfs are shown as filled gray squares, each displayed at three orthogonal (but random) orientations (for a total of 12 points). The range of simulated ellipticities is consistent with the range of the observed dwarfs. Our simulated dwarfs also have $v_{\rm rot}/\sigma$ values that are broadly consistent with the data [5]. We will need more simulations [76] to determine whether we can ever achieve the modest fraction of isolated galaxies (3/10) with $v_{\rm rot}/\sigma \simeq 1.5 - 2$ that we see among isolated Local Group dwarfs. If not, then this may suggest that the star formation is too bursty, or that the specific feedback implementation causes too much coupling between the injected energy and both the stellar populations and the dissipationless dark matter at the hearts of dwarf galaxies [188, 45].

Figure 4.2 shows $v_{\rm rot}/\sigma$ vs. stellar mass for all of the objects in our sample. No obvious trend with stellar mass is seen, though we note that 4/6 systems with $v_{\rm rot}/\sigma > 1$ all have $M_\star > 10^6 M_\odot$. Kormendy et al. [143] show that more luminous ($-23.24 < M_{\rm V} < -15.53$) dSphs in the Virgo cluster form an extension of Local Group dSphs in the Sersic index-$M_{\rm V}$ plane, and Toloba et al. [248] find a wide range of $v_{\rm rot}/\sigma$ values for subset of the Virgo dwarfs ($-19.0 < M_{\rm r} < -16.0$), but both of these studies rely on photometry from diffuse light. Extending our analysis (using resolved stellar populations) to higher mass objects, both observed and simulated, would be useful in detecting either a trend between of $v_{\rm rot}/\sigma$ and $M_\star$ at higher mass, or a discontinuity between dSphs/dEs and rotating disks. However, at least on the observational side, this analysis may have to wait for the next generation of telescopes. An initial analysis of one slightly more massive

[5] The simulations also show a higher degree of rotation in their cold gas, in qualitative agreement with observations [167, 87].

($M_\star \sim 10^9$ $M_\odot$) simulated dwarf run with the same code at slightly lower resolution, shows that it is also dispersion-supported ($v_{\rm rot}/\sigma \lesssim 0.25$), but more runs at higher mass are needed in the simulations to make a stronger statement about mass trends.

4.5.1 Inferring 3D Rotation

The $v_{\rm rot}/\sigma$ values estimated by our model and listed in Table 4.1 are lower limits to the intrinsic amount of rotation support for each galaxy. This is due to the fact that the line of sight velocity we measure is $v_{\rm rot} = v_{\rm rot}^{\rm intrinsic} \sin i$. We can correct for the actual measured inclination of at least those (6/10) galaxies with measured inclination angles in HI: Aquarius (66.7°), Pegasus (69.4°), WLM (74.0°), IC1613 (48.0°)[191], Leo A (60.3°) [100], and NGC 6822 (60°) [270]. Additionally, Read, Agertz & Collins [206] estimate an inclination of 20° for Leo T by matching their simulations to the galaxy's photometric light profile. With these inclination values, the estimated $v_{\rm rot}/\sigma$ value for Aquarius changes from 1.99 to 2.17, for IC 1613 from 0.48 to 0.64, for Leo A from 1.99 to 2.30, for NGC 6822 from 0.39 to 0.45, for Pegasus from 1.43 to 1.53, for WLM from 1.01 to 1.05, and for Leo T from 0.08 to 0.22. None of the estimated $v_{\rm rot}/\sigma$ values move from < 1 to > 1 and, of the four galaxies without measured inclinations, VV 124 has the highest $v_{\rm rot}/\sigma$ value (0.56), and would still have $/ratio < 1$ for inclination as low as 35°. Therefore it is unlikely that inclination severely affects the primary result presented in this work – that dwarf galaxies do not form as cold, rotating disks with $v_{\rm rot}/\sigma \gtrsim 2$.

Another way of evaluating the effect of inclination on the estimated line of sight $v_{\rm rot}/\sigma$ values is to infer something about the distribution of three dimensional rotation in our sample by comparing the observed distribution ($v_{\rm rot}/\sigma = v_{\rm rot}^{\rm intrinsic} \sin i/\sigma$) to what would be measured for a given $v_{\rm rot}^{\rm intrinsic}$ viewed in projection from random orientations. [6] As can be seen in Figure 4.4, the observed

[6] We have assumed that σ is independent of viewing angle, which is a good approximation for dispersion-supported objects. For rotationally supported objects, if σ is larger in the plane of the disk compared to vertically, as is the case for the Milky Way, the result of a face-on viewing angle will have less of an effect than described here.

distribution of $v_{\rm rot}/\sigma$ for satellite galaxies (thick solid black line) closely matches the distribution of $v_{\rm rot}^{\rm intrinsic}/\sigma = 0.7$ (dotted magenta line), but with a slight tail out to higher intrinsic rotation values. The multiple (1000) gray lines indicate the possible distributions of $v_{\rm rot}/\sigma$ if each data point is selected from a Gaussian distribution centered on the $v_{\rm rot}/\sigma$ values from our model, and with standard deviations also taken from the model (1σ errors).[7] The distribution of line of sight $v_{\rm rot}/\sigma$ values for the isolated dwarfs (thin solid cyan line) lies just outside of this "error band" for satellite galaxies, with a distinct excess at $v_{\rm rot}/\sigma \sim 0.7 - 2.0$. The isolated galaxy distribution more closely matches a distribution of $v_{\rm rot}^{\rm intrinsic}/\sigma \approx 1 - 2$ (dashed magenta line at $v_{\rm rot}^{\rm intrinsic}/\sigma = 2$), but falls far short of matching the (dash-dotted magenta) $v_{\rm rot}^{\rm intrinsic}/\sigma = 3$ line. While it appears that the isolated sample has more intrinsic rotation than the satellite sample, the isolated sample remains only marginally rotationally supported, with none as cold as $v_{\rm rot}^{\rm intrinsic}/\sigma \sim 3$, the value commonly used in tidal stirring simulations.

4.6 Discussion

A clear prediction made by the tidal stirring model of dSph formation is the increase of $v_{\rm rot}/\sigma$ with increasing distance from a more massive galaxy [117]. Because the most distant galaxies in the Local Group could have had no more than one pericenter passage in a Hubble time [and most are expected to have had none, e.g., 80], we would expect that galaxies that lie beyond the virial radius of either giant to have larger $v_{\rm rot}/\sigma$ values if tidal stirring plays the primary role in shaping dwarf galaxy dynamics.

Figure 4.3 explores this possibility by showing $v_{\rm rot}/\sigma$ vs. distance from the closest massive Local Group galaxy (MW or M31). We do not see any clear trend between $v_{\rm rot}/\sigma$ and distance to a massive galaxy, as would be expected if multiple close pericenter passages were necessary for

[7] For clarity, the error is not shown for the distribution of isolated galaxies, but has a wider spread than the error in the satellite population.

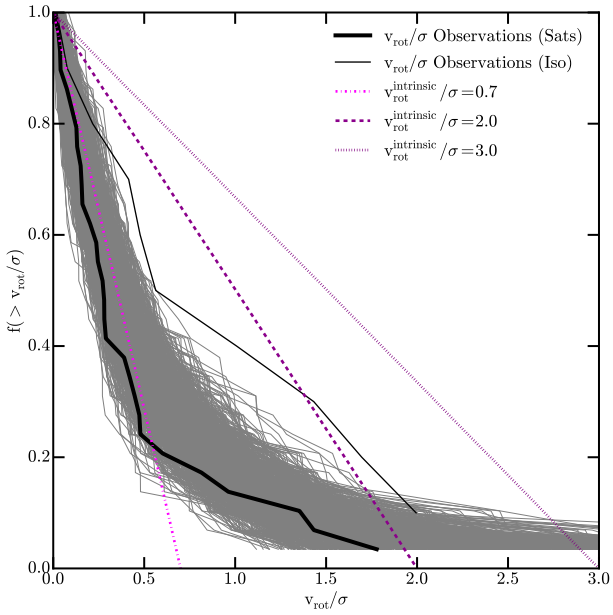

Figure 4.4: Distribution of measured $v_{\rm rot}/\sigma$ on the sky if all galaxies are assumed to have an intrinsic $v_{\rm rot}/\sigma$ value of 0.7 (dash-dotted line), 2.0 (dashed line) or 3.0 (dotted line), but are viewed with a random inclination. The thick solid black (thin solid cyan) line shows the distribution of estimated median $v_{\rm rot}/\sigma$ values for the satellites (isolated dwarfs) in our sample. The error in the satellite distribution is illustrated with 1000 thin gray lines, each consisting of points drawn randomly from Gaussian distributions with parameters taken from the estimated values for each of the 29 dSphs in our sample. For clarity, the error is not shown for the distribution of isolated galaxies, but has a wider spread than the lines for the satellite population. The isolated distribution is distinct from the satellite distribution, and more closely tracks $v_{\rm rot}^{\rm intrinsic}/\sigma \sim 1-2$. However, it is clear that the $v_{\rm rot}^{\rm intrinsic}/\sigma$ values for the isolated galaxies are much less than 3, the commonly used value in tidal stirring simulations.

removing rotation from dwarf galaxies.

Given the lack of trend between $v_{\rm rot}/\sigma$ and distance, we are more inclined to suspect that the stars in small galaxies are formed in a medium with marginal rotation support, and undergo merely a modest transformation to become dSphs. Some further evidence for this comes from Sánchez-Janssen, Méndez-Abreu & Aguerri [217], who study 11,753 galaxies from the Sloan Digital Sky Survey (SDSS) and Karachentsev et al. [112]. They suggest the existence of a critical stellar mass, $M_\star = 2 \times 10^9$ M$_\odot$, below which all galaxies become systematically thicker. One important question that will need to be investigated with future simulations is whether or not galaxies that start out with $v_{\rm rot}/\sigma \sim 1-2$ can undergo enough of a transformation to match the near zero values observed for the smallest dwarf satellites within the infall time constraints provided by cosmological simulations. Although it is likely that a mild transformation in $v_{\rm rot}/\sigma$ would take much less than the 10 Gyr required by tidal-stirring simulations, it would be instructive to use mildly dispersion-dominated dwarfs – in particular at slightly higher mass than those presented here – as the initial conditions for those models. An initial study has been performed by Mayer [169], who perform tidal stirring simulations on a gas-dominated, cosmological dwarf with a larger vertical scale height (aspect ratio $\sim 3:1$) resulting from stellar feedback-driven turbulence in the star-forming gas. In this work, the thicker dwarf reaches $v_{\rm rot}/\sigma < 0.5$ in just under 2 pericenter passages, without the typical bar formation and subsequent buckling common in tidally-induced transformations. Additional work along these lines should prove particularly informative.

We have checked to see if the four observed "rotating" systems are distinct in other properties that might help explain why they have $v_{\rm rot}/\sigma$ values that are > 1. These objects do not appear to be significant outliers in metallicity, inner density, star formation history or star formation rate, but a more thorough search for galaxy properties that do correlate with $v_{\rm rot}/\sigma$ would be useful. In addition to explaining the small number of outlying observed dwarfs, it could further explain why most of the simulated galaxies fail to demonstrate an elevated $v_{\rm rot}/\sigma$ – perhaps all simulated halos were selected in a way that disfavors the property that best correlates with rotation support. Gallart

et al. [79] do find that Aquarius and Leo A qualify as "slow" dwarfs, having formed in a low density environment which leads to a small fraction of their stars forming early, followed by continues star formation until the present time. This is in contrast to "fast" dwarfs that form the majority of their stars in a single, early burst. However, our simulated dwarfs were preferentially selected to inhabit low density environments, and yet have low $v_{\rm rot}/\sigma$ values. Additional simulations selected from a variety of environments would be useful to test these effects.

All stars analyzed in this work are either red giant or horizontal branch stars, so it is unlikely that we are biasing our sample due to stellar ages. A separate analysis of stellar populations with varying ages – in both the observations as well as the simulations – would likely be informative, but is beyond the scope of this paper.

4.7 Summary and Conclusion

We have performed a systematic Bayesian search for stellar rotation in 40 dwarf galaxies ($10^{3.5}$ M$_\odot$ < M$_\star$ < 10^8 M$_\odot$) in the Local Group, using resolved stellar kinematic data from the literature. We find that the vast majority of these galaxies ($\sim$ 80%) have $v_{\rm rot}/\sigma$ values that imply dispersion-supported kinematics. In particular, we find that 6/10 isolated dwarfs in our sample have $v_{\rm rot}/\sigma < 1.0$, and all have $v_{\rm rot}/\sigma \lesssim 2$ (see Figure 1 and Table 1). This result for the most distant LG dwarfs galaxies contrasts the common assumption that dwarf galaxies form with cold, rotationally-supported stellar disks (with $v_{\rm rot}/\sigma \sim 3$). We find no strong trend of $v_{\rm rot}/\sigma$ with $M_\star$ within the mass range studied (Figure 2), nor any trend of $v_{\rm rot}/\sigma$ with distance from large host galaxy in the Local Group (Figure 3), as would be expected if tidal stirring scenarios drive a kinematic transformation of stars in dIrr galaxies to dSph galaxies over multiple pericenter passages.

Taken together, our results suggest that dwarf galaxies form as puffy stellar systems that either dispersion-supported, or only mildly rotation-dominated. The conversion of a dIrr galaxy into

dSph galaxy may involve little more than the removal of its gas, and a resulting mild decrease of its $v_{\rm rot}/\sigma$. Specifically, the process of gas stripping itself may be enough to shock the potential, transforming a stellar system with $v_{\rm rot}/\sigma \sim 1.5$ into a system with $v_{\rm rot}/\sigma \sim 0.5$. Detailed simulations of this kind will be needed to test this hypothesis.

The formation of initially dispersion-supported systems is more likely to occur within dark matter halos with shallow potential wells (KWB), especially if explosive feedback effects act to dynamically heat stellar populations after the stars form. We have examined $v_{\rm rot}/\sigma$ in four cosmological zoom-in simulations of isolated dwarf galaxies that include such explosive feedback events [275, 188, 185]. These simulated dwarfs have $M_\star - M_{\rm halo}$ values that lie very close to extrapolated abundance-matching relations [98, 188, 275], so the total amount of energy injected to the surrounding medium is likely appropriate. However, the strength and frequency of bursts could modify the fraction of energy that couples to stars and dark matter, and so could be driving the stellar kinematics. All but 2 of the 12 viewing angles for the simulated dwarfs show (mock-observed) stellar dispersion support values $v_{\rm rot}/\sigma \simeq 0 - 0.8$ (and ellipticities $\simeq 0.2 - 0.7$), and all are completely consistent with our derived properties of observed satellite dwarfs and isolated dwarfs without a significant need for harassment from a massive neighbor. While these simulations are certainly not the final word on the formation of dwarf galaxies, the result suggests that it is at least reasonable to posit that dwarf galaxies are generally born moderately hot and are never strongly rotationally-supported.

The comparison between our model isolated dwarfs and the data did reveal one source of potential tension: none of our simulated dwarfs have stellar rotations that are as high as the highest in our sample (the 3/10 isolated galaxies with $v_{\rm rot}/\sigma \simeq 1.5 - 2$). This is not particularly surprising, given the small number of simulations analyzed here, but if this discrepancy holds in the face of better data and more simulations, it could point to a new test for feedback models. In particular, it is via bursty and violent feedback episodes that the dark matter cores in these halos are reduced in density, thus alleviating potential problems with ΛCDM like the Too Big to Fail problem [32]. As

first pointed out by Teyssier et al. [240], the same outbursts also inject significant random energy into the stellar populations [see also 116, 45]. A more detailed comparison between simulated and observed $v_{\rm rot}/\sigma$ values may offer an interesting direction in testing models that attempt to solve dark matter problems via explosive feedback episodes [e.g. 86, 240, 36, 188, 45]. Can these same models preserve the mild stellar rotation that is seen in some isolated dwarfs? Or, is stellar rotation only seen in galaxies with cuspy density distributions, which would be an important prediction of such models? The analysis of observational data provided here will hopefully provide an important benchmark for this question going forward.

Chapter 5

Conclusions

In this work, we study dwarf satellite galaxy quenching, the existence of ultra-faint dwarfs around isolated dwarf galaxies in the Local Volume, and the stellar kinematics of simulated and observed dwarfs. A thorough discussion and conclusions for each topic are presented within their respective chapters. However, we summarize our main findings here.

Chapter 2 Conclusions:

- Fewer than 30% of dwarfs with $M_\star \simeq 10^{8.5-9.5}\,\mathrm{M}_\odot$ have had their star formation shut down, in spite of the expectation from cosmological simulations that half of them should have been accreted more than 6 Gyr ago.
- The combination of the low observed quenched fraction and infall times from cosmological simulations suggests that the quenching timescale in this satellite mass range is very long ($> 9.5\,\mathrm{Gyr}$).

Chapter 3 Conclusions:

- Dwarf galaxies throughout the universe, including isolated dwarfs in the Local Volume,

should commonly host ultra-faint satellites of their own.

- Each of our simulated ultra-faint galaxies ($M_\star \simeq 3 - 30 \times 10^3$ $M_\odot$) has a uniformly ancient stellar population (> 10 Gyr), likely having had its star formation shut down by reionization. This is in contrast to the massive systems, which all have late-time star formation. This suggests that galaxies that form in halos with $M_{\rm halo} \simeq 5 \times 10^9\,M_\odot$ host true reionization "fossils", while galaxies that form in more massive halos continue to form stars after reionization, assuming that there are no environmental effects.

- With observational searches for ultra-faint galaxies, targeting the$\sim$ 50 kpc regions around nearby isolated dwarfs could increase the chances of discovery by $\sim$ 35% compared to a random telescope pointing.

Chapter 4 Conclusions:

- The stellar populations in $\sim$ 80% of the 40 LV dwarf galaxies studied in this work, which consists of both satellites and isolated systems, are dispersion-dominated. Additionally, four FIRE hydrodynamic zoom-in simulations of isolated dwarf galaxies ($10^9\,M_\odot < M_{\rm vir} < 10^{10}\,M_\odot$) have stellar ellipticities and stellar $v_{\rm rot}/\sigma$ ratios consistent with the observed population of dIrrs *and* dSphs without subjecting these dwarfs to tidal forces.

- 6/10 *isolated* dwarfs in our sample have $v_{\rm rot}/\sigma \lesssim 1.0$, while all have $v_{\rm rot}/\sigma \lesssim 2.0$, calling into question the traditional view that the stars in dwarf irregulars are distributed in cold, rotationally-dominated stellar disks while dwarf spheroidals have dispersion-supported stars.

- We find no trend between $v_{\rm rot}/\sigma$ and $M_\star$, nor between $v_{\rm rot}/\sigma$ and distance to the nearest host within our sample.

Bibliography

[1] Adén D. et al., 2009, AAP, 506, 1147

[2] Agertz O. et al., 2007, MNRAS, 380, 963

[3] Aihara H. et al., 2011, ApJ Supplement, 193, 29

[4] Amorisco N. C., Evans N. W., van de Ven G., 2014, Nature, 507, 335

[5] Baldry I. K. et al., 2012, MNRAS, 421, 621

[6] Battinelli P., Demers S., Kunkel W. E., 2006, AAP, 451, 99

[7] Begum A., Chengalur J. N., 2004, AAP, 413, 525

[8] Behroozi P. S., Marchesini D., Wechsler R. H., Muzzin A., Papovich C., Stefanon M., 2013, APJ Letters, 777, L10

[9] Behroozi P. S., Wechsler R. H., Lu Y., Hahn O., Busha M. T., Klypin A., Primack J. R., 2013, ArXiv e-prints, arXiv:1310.2239

[10] Behroozi P. S., Wechsler R. H., Wu H.-Y., 2013, APJ, 762, 109

[11] Behroozi P. S., Wechsler R. H., Wu H.-Y., Busha M. T., Klypin A. A., Primack J. R., 2013, APJ, 763, 18

[12] Belokurov V. et al., 2008, APJ Letters, 686, L83

[13] Belokurov V. et al., 2010, APJ Letters, 712, L103

[14] Belokurov V. et al., 2009, MNRAS, 397, 1748

[15] Belokurov V. et al., 2007, APJ, 654, 897

[16] Belokurov V. et al., 2006, APJ Letters, 647, L111

[17] Bender R., Burstein D., Faber S. M., 1993, APJ, 411, 153

[18] Benítez-Llambay A., Navarro J. F., Abadi M. G., Gottlöber S., Yepes G., Hoffman Y., Steinmetz M., 2015, MNRAS, 450, 4207

[19] Benson A. J., Frenk C. S., Lacey C. G., Baugh C. M., Cole S., 2002, MNRAS, 333, 177

[20] Benson A. J., Lacey C. G., Baugh C. M., Cole S., Frenk C. S., 2002, MNRAS, 333, 156

[21] Besla G., Kallivayalil N., Hernquist L., Robertson B., Cox T. J., van der Marel R. P., Alcock C., 2007, APJ, 668, 949

[22] Bigiel F., Leroy A., Walter F., Brinks E., de Blok W. J. G., Madore B., Thornley M. D., 2008, AJ, 136, 2846

[23] Bigiel F. et al., 2011, APJ Letters, 730, L13

[24] Binney J., 1978, MNRAS, 183, 501

[25] Birnboim Y., Dekel A., Neistein E., 2007, MNRAS, 380, 339

[26] Blanton M. R., Kazin E., Muna D., Weaver B. A., Price-Whelan A., 2011, AJ, 142, 31

[27] Blumenthal G. R., Faber S. M., Primack J. R., Rees M. J., 1984, Nature, 311, 517

[28] Boselli A., Cortese L., Boquien M., Boissier S., Catinella B., Gavazzi G., Lagos C., Saintonge A., 2014, AAP, 564, A67

[29] Bovill M. S., Ricotti M., 2009, APJ, 693, 1859

[30] Bovill M. S., Ricotti M., 2011, APJ, 741, 17

[31] Bovill M. S., Ricotti M., 2011, APJ, 741, 18

[32] Boylan-Kolchin M., Bullock J. S., Kaplinghat M., 2011, MNRAS, 415, L40

[33] Boylan-Kolchin M., Bullock J. S., Kaplinghat M., 2012, MNRAS, 422, 1203

[34] Boylan-Kolchin M., Bullock J. S., Sohn S. T., Besla G., van der Marel R. P., 2013, APJ, 768, 140

[35] Boylan-Kolchin M., Springel V., White S. D. M., Jenkins A., Lemson G., 2009, MNRAS, 398, 1150

[36] Brooks A. M., Zolotov A., 2014, APJ, 786, 87

[37] Brown T. M. et al., 2014, APJ, 796, 91

[38] Bryan G. L., Norman M. L., 1998, APJ, 495, 80

[39] Bullock J. S., Kravtsov A. V., Weinberg D. H., 2000, APJ, 539, 517

[40] Bullock J. S., Stewart K. R., Kaplinghat M., Tollerud E. J., Wolf J., 2010, APJ, 717, 1043

[41] Busha M. T., Alvarez M. A., Wechsler R. H., Abel T., Strigari L. E., 2010, APJ, 710, 408

[42] Cappellari M. et al., 2007, MNRAS, 379, 418

[43] Carlin J. L., Grillmair C. J., Muñoz R. R., Nidever D. L., Majewski S. R., 2009, APJ Letters, 702, L9

[44] Casetti-Dinescu D. I., Girard T. M., 2016, MNRAS

[45] Chan T. K., Kereš D., Oñorbe J., Hopkins P. F., Muratov A. L., Faucher-Giguère C.-A., Quataert E., 2015, MNRAS, 454, 2981

[46] Collins M. L. M. et al., 2010, MNRAS, 407, 2411

[47] Collins M. L. M. et al., 2013, APJ, 768, 172

[48] Collins M. L. M. et al., 2011, MNRAS, 417, 1170

[49] Dalcanton J. J., Stilp A. M., 2010, APJ, 721, 547

[50] Dalcanton J. J., Yoachim P., Bernstein R. A., 2004, APJ, 608, 189

[51] de Jong J. T. A., Martin N. F., Rix H.-W., Smith K. W., Jin S., Macciò A. V., 2010, APJ, 710, 1664

[52] De Lucia G., Weinmann S., Poggianti B. M., Aragón-Salamanca A., Zaritsky D., 2012, MNRAS, 423, 1277

[53] Deason A. J. et al., 2014, MNRAS, 444, 3975

[54] Deason A. J., Wetzel A. R., Garrison-Kimmel S., Belokurov V., 2015, ArXiv e-prints

[55] Dekel A., Silk J., 1986, APJ, 303, 39

[56] Demers S., Battinelli P., Kunkel W. E., 2006, APJ Letters, 636, L85

[57] Diemand J., Kuhlen M., Madau P., Zemp M., Moore B., Potter D., Stadel J., 2008, Nature, 454, 735

[58] Dijkstra M., Haiman Z., Rees M. J., Weinberg D. H., 2004, APJ, 601, 666

[59] Dinescu D. I., Girard T. M., van Altena W. F., López C. E., 2005, APJ Letters, 618, L25

[60] D'Onghia E., Besla G., Cox T. J., Hernquist L., 2009, Nature, 460, 605

[61] D'Onghia E., Lake G., 2008, APJ Letters, 686, L61

[62] Dressler A., 1980, APJ, 236, 351

[63] Drlica-Wagner A. et al., 2015, APJ, 813, 109

[64] Efstathiou G., 1992, MNRAS, 256, 43P

[65] Einasto J., Saar E., Kaasik A., Chernin A. D., 1974, Nature, 252, 111

[66] Faber S. M., Lin D. N. C., 1983, APJ Letters, 266, L17

[67] Fall S. M., Efstathiou G., 1980, MNRAS, 193, 189

[68] Fattahi A., Navarro J. F., Starkenburg E., Barber C. R., McConnachie A. W., 2013, MNRAS, 431, L73

[69] Faucher-Giguère C.-A., Lidz A., Zaldarriaga M., Hernquist L., 2009, APJ, 703, 1416

[70] Feast M. W., Thackeray A. D., Wesselink A. J., 1961, MNRAS, 122, 433

[71] Ferguson H. C., Binggeli B., 1994, AAPR, 6, 67

[72] Feroz F., Hobson M. P., 2008, MNRAS, 384, 449

[73] Feroz F., Hobson M. P., Bridges M., 2009, MNRAS, 398, 1601

[74] Fillingham S. P., Cooper M. C., Pace A. B., Boylan-Kolchin M., Bullock J. S., Garrison-Kimmel S., Wheeler C., 2016, ArXiv e-prints

[75] Fillingham S. P., Cooper M. C., Wheeler C., Garrison-Kimmel S., Boylan-Kolchin M., Bullock J. S., 2015, MNRAS, 454, 2039

[76] Fitts A., Boylan-Kolchin M., Bullock J. S., Wheeler C., 2016, in prep.

[77] Fraternali F., Tolstoy E., Irwin M. J., Cole A. A., 2009, AAP, 499, 121

[78] Frinchaboy P. M., Majewski S. R., Muñoz R. R., Law D. R., Łokas E. L., Kunkel W. E., Patterson R. J., Johnston K. V., 2012, APJ, 756, 74

[79] Gallart C. et al., 2015, APJ Letters, 811, L18

[80] Garrison-Kimmel S., Boylan-Kolchin M., Bullock J. S., Lee K., 2014, MNRAS, 438, 2578

[81] Geha M., Blanton M. R., Masjedi M., West A. A., 2006, APJ, 653, 240

[82] Geha M., Blanton M. R., Yan R., Tinker J. L., 2012, APJ, 757, 85

[83] Geha M., van der Marel R. P., Guhathakurta P., Gilbert K. M., Kalirai J., Kirby E. N., 2010, APJ, 711, 361

[84] Geha M., Willman B., Simon J. D., Strigari L. E., Kirby E. N., Law D. R., Strader J., 2009, APJ, 692, 1464

[85] Genzel R. et al., 2010, MNRAS, 407, 2091

[86] Governato F. et al., 2012, MNRAS, 422, 1231

[87] Grebel E. K., 1999, in IAU Symposium, Vol. 192, The Stellar Content of Local Group Galaxies, Whitelock P., Cannon R., eds., p. 17

[88] Grillmair C. J., 2006, APJ Letters, 645, L37

[89] Grillmair C. J., 2009, APJ, 693, 1118

[90] Gunn J. E., Gott, III J. R., 1972, APJ, 176, 1

[91] Guo Q. et al., 2011, MNRAS, 413, 101

[92] Hahn O., Abel T., 2011, MNRAS, 415, 2101

[93] Hearin A. P., Watson D. F., Becker M. R., Reyes R., Berlind A. A., Zentner A. R., 2013, ArXiv e-prints, arXiv:1310.6747

[94] Ho N. et al., 2012, APJ, 758, 124

[95] Hoeft M., Yepes G., Gottlöber S., Springel V., 2006, MNRAS, 371, 401

[96] Hopkins P. F., 2013, MNRAS, 428, 2840

[97] Hopkins P. F., 2014, ArXiv e-prints

[98] Hopkins P. F., Kereš D., Oñorbe J., Faucher-Giguère C.-A., Quataert E., Murray N., Bullock J. S., 2014, MNRAS, 445, 581

[99] Hunter D. A., Elmegreen B. G., 2006, ApJ Supplement, 162, 49

[100] Hunter D. A. et al., 2012, AJ, 144, 134

[101] Hunter D. A., Gallagher, III J. S., 1985, ApJ Supplement, 58, 533

[102] Ibata R. A. et al., 2013, Nature, 493, 62

[103] Ibata R. A., Wyse R. F. G., Gilmore G., Irwin M. J., Suntzeff N. B., 1997, AJ, 113, 634

[104] Icke V., 1985, AAP, 144, 115

[105] Irwin M., Tolstoy E., 2002, MNRAS, 336, 643

[106] Irwin M. J. et al., 2007, APJ Letters, 656, L13

[107] Ivezic Z. et al., 2008, Serbian Astronomical Journal, 176, 1

[108] Kaiser N. et al., 2002, in Society of Photo-Optical Instrumentation Engineers (SPIE) Conference Series, Vol. 4836, Survey and Other Telescope Technologies and Discoveries, Tyson J. A., Wolff S., eds., pp. 154–164

[109] Kaisin S. S., Karachentsev I. D., 2013, Astrophysics

[110] Kalirai J. S. et al., 2010, APJ, 711, 671

[111] Kaplinghat M., Strigari L. E., 2008, APJ Letters, 682, L93

[112] Karachentsev I. D., Karachentseva V. E., Huchtmeier W. K., Makarov D. I., 2004, AJ, 127, 2031

[113] Karachentsev I. D., Tully R. B., Wu P.-F., Shaya E. J., Dolphin A. E., 2014, APJ, 782, 4

[114] Katz N., White S. D. M., 1993, APJ, 412, 455

[115] Kaufmann T., Wheeler C., Bullock J. S., 2007, MNRAS, 382, 1187

[116] Kawata D., Gibson B. K., Barnes D. J., Grand R. J. J., Rahimi A., 2014, MNRAS, 438, 1208

[117] Kazantzidis S., Łokas E. L., Callegari S., Mayer L., Moustakas L. A., 2011, APJ, 726, 98

[118] Kazantzidis S., Łokas E. L., Mayer L., 2013, APJ Letters, 764, L29

[119] Kazantzidis S., Łokas E. L., Mayer L., Knebe A., Klimentowski J., 2011, APJ Letters, 740, L24

[120] Keller S., Bessell M., Schmidt B., Francis P., 2007, in Astronomical Society of the Pacific Conference Series, Vol. 364, The Future of Photometric, Spectrophotometric and Polarimetric Standardization, Sterken C., ed., p. 177

[121] Kennicutt, Jr. R. C. et al., 2007, APJ, 671, 333

[122] Kereš D., Katz N., Weinberg D. H., Davé R., 2005, MNRAS, 363, 2

[123] Kim D., Jerjen H., 2015, APJ Letters, 808, L39

[124] Kim D., Jerjen H., Mackey D., Da Costa G. S., Milone A. P., 2015, APJ Letters, 804, L44

[125] Kimm T. et al., 2009, MNRAS, 394, 1131

[126] Kirby E. N., Boylan-Kolchin M., Cohen J. G., Geha M., Bullock J. S., Kaplinghat M., 2013, APJ, 770, 16

[127] Kirby E. N., Bullock J. S., Boylan-Kolchin M., Kaplinghat M., Cohen J. G., 2014, MNRAS, 439, 1015

[128] Kirby E. N., Cohen J. G., Simon J. D., Guhathakurta P., 2015, ArXiv e-prints

[129] Kirby E. N., Simon J. D., Cohen J. G., 2015, APJ, 810, 56

[130] Kleyna J. T., Wilkinson M. I., Evans N. W., Gilmore G., 2005, APJ Letters, 630, L141

[131] Klimentowski J., Łokas E. L., Kazantzidis S., Mayer L., Mamon G. A., 2009, MNRAS, 397, 2015

[132] Klypin A., Kravtsov A. V., Valenzuela O., Prada F., 1999, APJ, 522, 82

[133] Klypin A. A., Trujillo-Gomez S., Primack J., 2011, APJ, 740, 102

[134] Knollmann S. R., Knebe A., 2009, ApJ Supplement, 182, 608

[135] Koch A., Kleyna J. T., Wilkinson M. I., Grebel E. K., Gilmore G. F., Evans N. W., Wyse R. F. G., Harbeck D. R., 2007, AJ, 134, 566

[136] Koch A., Wilkinson M. I., Kleyna J. T., Gilmore G. F., Grebel E. K., Mackey A. D., Evans N. W., Wyse R. F. G., 2007, APJ, 657, 241

[137] Koch A. et al., 2009, APJ, 690, 453

[138] Komatsu E. et al., 2011, ApJ Supplement, 192, 18

[139] Koposov S. et al., 2008, APJ, 686, 279

[140] Koposov S. E., Belokurov V., Torrealba G., Evans N. W., 2015, APJ, 805, 130

[141] Koposov S. E. et al., 2015, APJ, 811, 62

[142] Koposov S. E. et al., 2011, APJ, 736, 146

[143] Kormendy J., Fisher D. B., Cornell M. E., Bender R., 2009, ApJ Supplement, 182, 216

[144] Kravtsov A. V., Gnedin O. Y., Klypin A. A., 2004, APJ, 609, 482

[145] Kroupa P., 2002, Science, 295, 82

[146] Laevens B. P. M. et al., 2015, APJ, 813, 44

[147] Laevens B. P. M. et al., 2015, APJ Letters, 802, L18

[148] Laevens B. P. M. et al., 2014, APJ Letters, 786, L3

[149] Leaman R., Cole A. A., Venn K. A., Tolstoy E., Irwin M. J., Szeifert T., Skillman E. D., McConnachie A. W., 2009, APJ, 699, 1

[150] Leaman R. et al., 2012, APJ, 750, 33

[151] Leitherer C. et al., 1999, ApJ Supplement, 123, 3

[152] Lépine S., Koch A., Rich R. M., Kuijken K., 2011, APJ, 741, 100

[153] Leroy A. K., Walter F., Brinks E., Bigiel F., de Blok W. J. G., Madore B., Thornley M. D., 2008, AJ, 136, 2782

[154] Li Y.-S., Helmi A., 2008, MNRAS, 385, 1365

[155] Łokas E. L., Kazantzidis S., Mayer L., 2011, APJ, 739, 46

[156] Łokas E. L., Semczuk M., Gajda G., D'Onghia E., 2015, APJ, 810, 100

[157] Lozinskaya T. A., 2002, Astronomical and Astrophysical Transactions, 21, 223

[158] Madau P., Kuhlen M., Diemand J., Moore B., Zemp M., Potter D., Stadel J., 2008, APJ Letters, 689, L41

[159] Martin N. F. et al., 2014, APJ Letters, 793, L14

[160] Martin N. F., Ibata R. A., Chapman S. C., Irwin M., Lewis G. F., 2007, MNRAS, 380, 281

[161] Martin N. F. et al., 2015, ArXiv e-prints

[162] Martin N. F. et al., 2015, APJ Letters, 804, L5

[163] Martin N. F. et al., 2013, APJ, 772, 15

[164] Massari D., Bellini A., Ferraro F. R., van der Marel R. P., Anderson J., Dalessandro E., Lanzoni B., 2013, APJ, 779, 81

[165] Mastropietro C., Moore B., Mayer L., Debattista V. P., Piffaretti R., Stadel J., 2005, in IAU Colloq. 198: Near-fields cosmology with dwarf elliptical galaxies, Jerjen H., Binggeli B., eds., pp. 244–248

[166] Mateo M., Olszewski E. W., Walker M. G., 2008, APJ, 675, 201

[167] Mateo M. L., 1998, ARAA, 36, 435

[168] Mayer L., 2010, Advances in Astronomy, 2010, 25

[169] Mayer L., 2011, in EAS Publications Series, Vol. 48, EAS Publications Series, Koleva M., Prugniel P., Vauglin I., eds., pp. 369–381

[170] Mayer L., Governato F., Colpi M., Moore B., Quinn T., Wadsley J., Stadel J., Lake G., 2001, APJ, 559, 754

[171] Mayer L., Governato F., Colpi M., Moore B., Quinn T., Wadsley J., Stadel J., Lake G., 2001, APJ Letters, 547, L123

[172] Mayer L., Mastropietro C., Wadsley J., Stadel J., Moore B., 2006, MNRAS, 369, 1021

[173] McConnachie A. W., 2012, AJ, 144, 4

[174] McConnachie A. W., 2012, AJ, 144, 4

[175] Milosavljević M., Bromm V., 2014, MNRAS, 440, 50

[176] Monachesi A., Trager S. C., Lauer T. R., Freedman W., Dressler A., Grillmair C., Mighell K. J., 2011, APJ, 727, 55

[177] Moore B., Diemand J., Madau P., Zemp M., Stadel J., 2006, MNRAS, 368, 563

[178] Moore B., Ghigna S., Governato F., Lake G., Quinn T., Stadel J., Tozzi P., 1999, APJ Letters, 524, L19

[179] Moore B., Katz N., Lake G., Dressler A., Oemler A., 1996, Nature, 379, 613

[180] More S., van den Bosch F. C., Cacciato M., Skibba R., Mo H. J., Yang X., 2011, MNRAS, 410, 210

[181] Moster B. P., Naab T., White S. D. M., 2013, MNRAS, 428, 3121

[182] Muñoz R. R., Carlin J. L., Frinchaboy P. M., Nidever D. L., Majewski S. R., Patterson R. J., 2006, APJ Letters, 650, L51

[183] Muñoz R. R., Carlin J. L., Frinchaboy P. M., Nidever D. L., Majewski S. R., Patterson R. J., 2006, APJ Letters, 650, L51

[184] Muñoz R. R. et al., 2005, APJ Letters, 631, L137

[185] Muratov A. L., Kereš D., Faucher-Giguère C.-A., Hopkins P. F., Quataert E., Murray N., 2015, MNRAS, 454, 2691

[186] Navarro J. F., Frenk C. S., White S. D. M., 1997, APJ, 490, 493

[187] Nickerson S., Stinson G., Couchman H. M. P., Bailin J., Wadsley J., 2011, MNRAS, 415, 257

[188] Oñorbe J., Boylan-Kolchin M., Bullock J. S., Hopkins P. F., Kereš D., Faucher-Giguère C.-A., Quataert E., Murray N., 2015, MNRAS, 454, 2092

[189] Oñorbe J., Garrison-Kimmel S., Maller A. H., Bullock J. S., Rocha M., Hahn O., 2014, MNRAS, 437, 1894

[190] Oemler, Jr. A., 1974, APJ, 194, 1

[191] Oh S.-H. et al., 2015, AJ, 149, 180

[192] Okamoto T., Frenk C. S., 2009, MNRAS, 399, L174

[193] Pace A. B., 2016, ArXiv e-prints

[194] Pace A. B., Martinez G. D., Kaplinghat M., Muñoz R. R., 2014, MNRAS, 442, 1718

[195] Peñarrubia J., Belokurov V., Evans N. W., Martínez-Delgado D., Gilmore G., Irwin M., Niederste-Ostholt M., Zucker D. B., 2010, MNRAS, 408, L26

[196] Peñarrubia J. et al., 2011, APJ Letters, 727, L2

[197] Peng Y.-j. et al., 2010, APJ, 721, 193

[198] Phillips J. I., Wheeler C., Boylan-Kolchin M., Bullock J. S., Cooper M. C., Tollerud E. J., 2014, MNRAS, 437, 1930

[199] Piatek S., Pryor C., Bristow P., Olszewski E. W., Harris H. C., Mateo M., Minniti D., Tinney C. G., 2005, AJ, 130, 95

[200] Piatek S., Pryor C., Bristow P., Olszewski E. W., Harris H. C., Mateo M., Minniti D., Tinney C. G., 2006, AJ, 131, 1445

[201] Piatek S., Pryor C., Bristow P., Olszewski E. W., Harris H. C., Mateo M., Minniti D., Tinney C. G., 2007, AJ, 133, 818

[202] Piatek S., Pryor C., Olszewski E. W., Harris H. C., Mateo M., Minniti D., Tinney C. G., 2003, AJ, 126, 2346

[203] Power C., Navarro J. F., Jenkins A., Frenk C. S., White S. D. M., Springel V., Stadel J., Quinn T., 2003, MNRAS, 338, 14

[204] Pryor C., Piatek S., Olszewski E. W., 2010, AJ, 139, 839

[205] Pryor C., Piatek S., Olszewski E. W., 2015, AJ, 149, 42

[206] Read J. I., Agertz O., Collins M. L. M., 2016, MNRAS, 459, 2573

[207] Read J. I., Pontzen A. P., Viel M., 2006, MNRAS, 371, 885

[208] Ricotti M., 2010, Advances in Astronomy, 2010, 33

[209] Ricotti M., Gnedin N. Y., 2005, APJ, 629, 259

[210] Rocha M., Peter A. H. G., Bullock J., 2012, MNRAS, 425, 231

[211] Saintonge A. et al., 2011, MNRAS, 415, 61

[212] Sakamoto T., Hasegawa T., 2006, APJ Letters, 653, L29

[213] Sales L. V., Navarro J. F., Abadi M. G., Steinmetz M., 2007, MNRAS, 379, 1475

[214] Sales L. V., Navarro J. F., Cooper A. P., White S. D. M., Frenk C. S., Helmi A., 2011, MNRAS, 418, 648

[215] Sales L. V., Wang W., White S. D. M., Navarro J. F., 2013, MNRAS, 428, 573

[216] Salomon J.-B., Ibata R. A., Martin N. F., Famaey B., 2015, MNRAS, 450, 1409

[217] Sánchez-Janssen R., Méndez-Abreu J., Aguerri J. A. L., 2010, MNRAS, 406, L65

[218] Saviane I., Held E. V., Piotto G., 1996, AAP, 315, 40

[219] Sawala T. et al., 2015, MNRAS, 448, 2941

[220] Sawala T. et al., 2014, ArXiv e-prints

[221] Schiminovich D. et al., 2010, MNRAS, 408, 919

[222] Shen S., Madau P., Conroy C., Governato F., Mayer L., 2014, APJ, 792, 99

[223] Silich S., Lozinskaya T., Moiseev A., Podorvanuk N., Rosado M., Borissova J., Valdez-Gutierrez M., 2006, AAP, 448, 123

[224] Simon J. D., Drlica-Wagner A., Li T. S., Nord B., Geha M., Bechtol K., 2015, APJ, 808, 95

[225] Simon J. D., Geha M., 2007, APJ, 670, 313

[226] Simon J. D. et al., 2011, APJ, 733, 46

[227] Simpson C. M., Bryan G. L., Johnston K. V., Smith B. D., Mac Low M.-M., Sharma S., Tumlinson J., 2013, MNRAS, 432, 1989

[228] Skillman E. D., Côté S., Miller B. W., 2003, AJ, 125, 593

[229] Skrutskie M. F. et al., 2006, AJ, 131, 1163

[230] Slater C. T., Bell E. F., 2014, APJ, 792, 141

[231] Smith R. J., Lucey J. R., Price J., Hudson M. J., Phillipps S., 2012, MNRAS, 419, 3167

[232] Sohn S. T., Besla G., van der Marel R. P., Boylan-Kolchin M., Majewski S. R., Bullock J. S., 2013, APJ, 768, 139

[233] Somerville R. S., 2002, APJ Letters, 572, L23

[234] Springel V. et al., 2008, MNRAS, 391, 1685

[235] Srisawat C. et al., 2013, MNRAS, 436, 150

[236] Starkenburg T. K., Helmi A., Sales L. V., 2015, ArXiv e-prints

[237] Strigari L. E., Bullock J. S., Kaplinghat M., Diemand J., Kuhlen M., Madau P., 2007, APJ, 669, 676

[238] Strigari L. E., Bullock J. S., Kaplinghat M., Simon J. D., Geha M., Willman B., Walker M. G., 2008, Nature, 454, 1096

[239] Tegmark M., Silk J., Rees M. J., Blanchard A., Abel T., Palla F., 1997, APJ, 474, 1

[240] Teyssier R., Pontzen A., Dubois Y., Read J. I., 2013, MNRAS, 429, 3068

[241] The DES Collaboration et al., 2015, ArXiv e-prints

[242] Tinker J. L., Leauthaud A., Bundy K., George M. R., Behroozi P., Massey R., Rhodes J., Wechsler R. H., 2013, APJ, 778, 93

[243] Tollerud E. J. et al., 2012, APJ, 752, 45

[244] Tollerud E. J., Boylan-Kolchin M., Barton E. J., Bullock J. S., Trinh C. Q., 2011, APJ, 738, 102

[245] Tollerud E. J., Bullock J. S., Strigari L. E., Willman B., 2008, APJ, 688, 277

[246] Tollerud E. J., Geha M. C., Grcevich J., Putman M. E., Stern D., 2015, APJ Letters, 798, L21

[247] Tollerud E. J., Geha M. C., Vargas L. C., Bullock J. S., 2013, APJ, 768, 50

[248] Toloba E. et al., 2014, ApJ Supplement, 215, 17

[249] Tolstoy E., Irwin M., 2000, MNRAS, 318, 1241

[250] Tomozeiu M., Mayer L., Quinn T., 2015, ArXiv e-prints

[251] Trotta R., 2008, Contemporary Physics, 49, 71

[252] Tully R. B. et al., 2006, AJ, 132, 729

[253] Valenzuela O., Rhee G., Klypin A., Governato F., Stinson G., Quinn T., Wadsley J., 2007, APJ, 657, 773

[254] van den Bergh S., 1999, AAPR, 9, 273

[255] van den Bosch F. C., Aquino D., Yang X., Mo H., Pasquali A., McIntosh D. H., Weinmann S. M., Kang X., 2007

[256] van den Bosch F. C., Aquino D., Yang X., Mo H. J., Pasquali A., McIntosh D. H., Weinmann S. M., Kang X., 2008, MNRAS, 387, 79

[257] van der Marel R. P., Alves D. R., Hardy E., Suntzeff N. B., 2002, AJ, 124, 2639

[258] van Zee L., 2001, AJ, 121, 2003

[259] Walker M. G., Belokurov V., Evans N. W., Irwin M. J., Mateo M., Olszewski E. W., Gilmore G., 2009, APJ Letters, 694, L144

[260] Walker M. G., Mateo M., Olszewski E. W., 2008, APJ Letters, 688, L75

[261] Walker M. G., Mateo M., Olszewski E. W., Bailey, III J. I., Koposov S. E., Belokurov V., Evans N. W., 2015, APJ, 808, 108

[262] Walker M. G., Mateo M., Olszewski E. W., Bernstein R., Wang X., Woodroofe M., 2006, AJ, 131, 2114

[263] Walker M. G., Mateo M., Olszewski E. W., Gnedin O. Y., Wang X., Sen B., Woodroofe M., 2007, APJ Letters, 667, L53

[264] Walker M. G., Olszewski E. W., Mateo M., 2015, MNRAS, 448, 2717

[265] Walsh S. M., Jerjen H., Willman B., 2007, APJ Letters, 662, L83

[266] Wang W., Sales L. V., Henriques B. M. B., White S. D. M., 2014, ArXiv e-prints, arXiv:1403.2409

[267] Wang W., White S. D. M., 2012, MNRAS, 424, 2574

[268] Weinmann S. M., van den Bosch F. C., Yang X., Mo H. J., Croton D. J., Moore B., 2006, MNRAS, 372, 1161

[269] Weisz D. R. et al., 2011, APJ, 739, 5

[270] Weldrake D. T. F., de Blok W. J. G., Walter F., 2003, MNRAS, 340, 12

[271] Wetzel A. R., Deason A. J., Garrison-Kimmel S., 2015, APJ, 807, 49

[272] Wetzel A. R., Tinker J. L., Conroy C., Bosch F. C. v. d., 2014, MNRAS

[273] Wetzel A. R., Tinker J. L., Conroy C., van den Bosch F. C., 2013, MNRAS, 432, 336

[274] Wetzel A. R., Tollerud E. J., Weisz D. R., 2015, ArXiv e-prints

[275] Wheeler C., Oñorbe J., Bullock J. S., Boylan-Kolchin M., Elbert O. D., Garrison-Kimmel S., Hopkins P. F., Kereš D., 2015, MNRAS, 453, 1305

[276] Wheeler C., Phillips J. I., Cooper M. C., Boylan-Kolchin M., Bullock J. S., 2014, MNRAS, 442, 1396

[277] White S. D. M., Rees M. J., 1978, MNRAS, 183, 341

[278] Wilkinson M. I., Kleyna J. T., Evans N. W., Gilmore G. F., Irwin M. J., Grebel E. K., 2004, APJ Letters, 611, L21

[279] Willman B. et al., 2005, AJ, 129, 2692

[280] Willman B. et al., 2005, APJ Letters, 626, L85

[281] Willman B., Geha M., Strader J., Strigari L. E., Simon J. D., Kirby E., Ho N., Warres A., 2011, AJ, 142, 128

[282] Wolf J., Martinez G. D., Bullock J. S., Kaplinghat M., Geha M., Muñoz R. R., Simon J. D., Avedo F. F., 2010, MNRAS, 406, 1220

[283] Wong T., Blitz L., 2002, APJ, 569, 157

[284] Yoachim P., Dalcanton J. J., 2006, AJ, 131, 226

[285] Young L. M., Lo K. Y., 1996, APJ, 462, 203

[286] Young L. M., van Zee L., Lo K. Y., Dohm-Palmer R. C., Beierle M. E., 2003, APJ, 592, 111

[287] Zentner A. R., Bullock J. S., 2003, APJ, 598, 49

[288] Zhang H.-X., Hunter D. A., Elmegreen B. G., Gao Y., Schruba A., 2012, AJ, 143, 47

[289] Zucker D. B. et al., 2006, APJ Letters, 650, L41

[290] Zucker D. B. et al., 2006, APJ Letters, 643, L103